Institut für Angewandte Physik

Fachrichtung Physik

Fakultät Mathematik und Naturwissenschaften

Technische Universität Dresden

Laterally modified microcavity systems containing organic emitters

Dissertation

zur Erlangung des

akademischen Grades

Doctor rerum naturalium

(Dr. rer. nat.)

vorgelegt von

Maik Langner

geboren am 06. September 1982 in Leisnig

Dresden

2011

Eingereicht am 31. August 2010

1. Gutachter: Prof. Dr. Karl Leo

2. Gutachter: Prof. Dr. Uli Lemmer

Verteidigt am 07. April 2011

Abstract

The scope of this work is an in-depth investigation of dielectric mirror microcavities with central organic dye layers, which are preferably modified in at least one lateral dimension. The large quality factor of the planar resonator in conjunction with comparatively stable and spectrally broad emitting molecules allows for a detailed analysis of several aspects of microresonator systems. Their optical properties are analyzed both with transmission and luminescence measurements as well as in the lasing regime.

The first part presents the resonant mode properties of planar and laterally structured microcavities. With the help of a high-resolution imaging micro-photoluminescence setup, working either in the spatial (near field) or vectorial (far field) regime, the polarization splitting is studied in a detuned microcavity, containing the dye 4,4'-bis[(N-carbazole)styryl]biphenyl (BSB-Cz) in a matrix of 4,4'-di(N-carbazolyl)-biphenyl (CBP). With the help of a thickness gradient, a relation between the large spectral distance of the cross-polarized states and the mode position within the stop band is investigated. In shadow-mask prepared, laterally restricted devices ($5 \times 5\,\mu\text{m}^2$ square boxes), the three-dimensional confinement introduces sets of discrete modes, which experience a similar polarization splitting. The origin in this case is a different phase shift of electromagnetic waves during internal total reflection at a boundary.

By using a concentration gradient planar microcavity sample of the dye 4-(dicyanomethylene)-2-methyl-6-(4-(dimethylamino)styryl)-4H-pyran (DCM) in a tris-(8-hydroxyquinoline)aluminum (Alq$_3$) matrix, the influence of the number of emitters on the lasing characteristics is subsequently analyzed. Depending on the pumping conditions, and thus the involvement of the Förster resonant energy transfer, an optimal composition is identified. After a qualitative evaluation of the long-term stability upon various excitation energies, the attention is focussed to the modification of the stimulated emission properties of photonic boxes. The stronger field concentration and altered density of states leads to a significant improvement of the values for the coupling factor β and the threshold levels. Furthermore, new properties arise, namely simultaneous multimode and off-axis laser emission. With an inhomogeneous excitation of the box, it is possible to selectively excite single modes above the threshold.

The work ends with experimental results of metal structures as additional optical element in the organic microcavity layer. Here, the aim is is to understand the passive influence of these possible contact-devices on the lasing performance. For this purpose, the lasing is studied at an interface of an areal thin metal layer, which is incorporated in the organic layer.

Zusammenfassung

Gegenstand der vorliegenden Arbeit sind Mikroresonatoren, bestehend aus dielektrischen Spiegeln und einer zentralen, organischen Farbstoffschicht, die vorzugsweise zusätzlich lateral strukturiert sind. Auf Grund des hohen Qualitätsfaktors der Kavitäten, der spektral breiten Emission und der vergleichsweise großen Stabilität der verwendeten Moleküle ist es möglich, die Eigenschaften der Systeme sehr detailliert zu erforschen. Ihr optisches Verhalten wird sowohl bei Transmissions- und Lumineszenzmessungen als auch im Zustand der stimulierten Emission untersucht.

Der erste Abschnitt befasst sich mit den Eigenschaften resonanter Moden in planaren und lateral strukturierten Mikroresonatoren. Mit Hilfe eines hoch auflösenden abbildenden Mikrophotolumineszenzaufbaus, der sowohl räumliche als auch Fernfeldmessungen ermöglicht, wird eine polarisationsabhängige Aufspaltung der Resonatormode in verstimmten Kavitäten untersucht. Bei einer Probe, die einen kontinuierlichen Dickengradienten der Farbstoffschicht 4,4'-Bis[(N-carbazol)styryl]biphenyl (BSB-Cz), gelöst in 4,4'-Di(N-carbazolyl)biphenyl (CBP), aufweist, wird die Beziehung zwischen der breiten spektralen Aufspaltung und der Position der Resonatormode im Stopband untersucht. Bei quadratischen photonischen Boxen (Fläche $5 \times 5\,\mu\mathrm{m}^2$), bei denen die dreidimensionale Beschränkung des elektromagnetischen Feldes zur Ausbildung von diskreten Moden führt, tritt ein ähnliches Aufspaltungsverhalten auf. Der Ursprung ist in diesem Fall die polarisationsabhängige Phasenverschiebung, bedingt durch die Totalreflexion an den lateralen Grenzflächen.

Anschließend wird in einer Probe mittels eines Konzentrationsgradienten des Farbstoffs 4-(Dicyanomethylen)-2-methyl-6-(4-(dimethylamino)styryl)-4H-pyran (DCM) in Tris-(8-hydroxyquinolin)aluminium (Alq$_3$) der Einfluss der Emitteranzahl auf das Laserverhalten untersucht. Sowohl ein direktes Pumpen des Dotanden als auch der indirekte Weg über den nichtstrahlenden Förster-Transfer wird verwendet, um eine optimale Zusammensetzung zu finden. Desweiteren findet eine qualitative Untersuchung der Langzeitstabilität der Systeme bei verschiedenen Anregungsenergien statt.

Im folgenden wird die Veränderung der Eigenschaften der stimulierten Emission in photonischen Boxen analysiert. Die im Vergleich zu unstrukturierten Mikroresonatoren höhere Feldkonzentration und die veränderte Zustandsdichte führen zu einer signifikanten Verbesserung des Kopplungsfaktors β und des Wertes der Laserschwelle. Zusätzlich werden neue Effekte beobachtet, unter anderem die gleichzeitige, stimulierte Emission bei verschiedenen Wellenlängen und unter schrägem Beobachtungswinkel. Durch eine inhomogene Anregung der Boxstrukturen ist es außerdem möglich, einzelne Moden selektiv zum Lasen zu bringen.

Der letzte Abschnitt der Arbeit befasst sich mit optischen Experimenten an Metallstrukturen in organischen Mikroresonatoren. Das Ziel dieser Versuche ist es, den passiven optischen Einfluss potentieller elektrischer Kontakte auf das Laserverhalten zu ermitteln. Zu diesem Zweck wird die stimulierte Emission in der Nähe einer Grenzfläche einer flächigen dünnen Metallschicht untersucht und mit Simulationen verglichen.

List of publications

Scientific articles

Strong optical confinement and multimode emission of organic photonic dots
M. Langner, R. Gehlhaar, C. Schriever, H. Fröb, V.G. Lyssenko, and K. Leo, *Appl. Phys. Lett.* **91**, 18 (2007)

Near and far field observation of optical confinement in non-destructive fabricated organic photonic dots
M. Langner, R. Gehlhaar, C. Schriever, H. Fröb, V.G. Lyssenko, and K. Leo, *Proc. NUSOD 7* (2007)

Stretched input-output characteristic in inhomogeneously broadened lasing system
S.I. Hintschich, M. Langner, H. Gothe, V.G. Lyssenko, H. Fröb, and K. Leo, *Proc. NUSOD 7* (2007)

Optical modes in wavelength-sized organic microcavity structures
M. Langner, R. Gehlhaar, S.I. Hintschich, H. Fröb, H. Wendrock, V.G. Lyssenko, and K. Leo, *Opt. Quant. Elect.* **40**, 5-6 (2008)

Sub-nanojule threshold lasing in $5 \times 5\,\mu m^2$ organic photonic boxes
M. Langner, M. Sudzius, S.I. Hintschich, H. Fröb, V.G. Lyssenko, and K. Leo, *Proc. SPIE* **6999**, 99902 (2008)

Multimode laser emission from laterally confined organic microcavities
M. Sudzius, M. Langner, S.I. Hintschich, V.G. Lyssenko, H. Fröb, and K. Leo, *Appl. Phys. Lett.* **94**, 6 (2009)

Selective excitation of laser modes in an organic photonic dot microcavity
M. Langner, M. Sudzius, H. Fröb, V.G. Lyssenko, and K. Leo, *Appl. Phys. Lett.* **95**, 9 (2009)

Polarization splitting of discrete states in square shaped organic photonic dots
E. Siebert-Henze, M. Langner, M. Sudzius , S.I. Hintschich, H. Fröb, V.G. Lyssenko, and K. Leo, *Appl. Phys. Lett.* **95**, 19 (2009)

Dependence of polarization splitting on mode tuning in microcavities
F. Becker, M. Langner, H. Fröb, V.G. Lyssenko, K. Leo, and C. Adachi, *Appl. Phys. Lett.* **95**, 19 (2009)

Conference contributions

Multimode spontaneous emission of optically confined organic photonic dots
M. Langner, C. Schriever, R. Gehlhaar, H. Fröb, V.G. Lyssenko, and K. Leo, Frühjahrstagung der Deutschen Physikalischen Gesellschaft, Regensburg (2007)

Spontaneous emission confinement in organic photonic dots
R. Gehlhaar, M. Langner, H. Fröb, V.G. Lyssenko, and K. Leo, Hytec meeting, Cachan (2007)

Near and far field observation of optical confinement in non-destructive fabricated organic photonic dots
M. Langner, R. Gehlhaar, C. Schriever, H. Fröb, V.G. Lyssenko, and K. Leo, NUSOD-7, Delaware (2007)

Stretched input-output characteristic in inhomogeneously broadened lasing system
S.I. Hintschich, M. Langner, H. Gothe, V.G. Lyssenko, H. Fröb, and K. Leo, NUSOD-7, Delaware (2007)

Multimode Laser emission from organic photonic dots
M. Sudzius, M. Langner, S.I. Hintschich, H. Fröb, V.G. Lyssenko, and K. Leo, 13th Microoptics Conference, Takamatsu (2007)

Influence of metal structures on the optical properties of organic microcavities
M. Langner, T. Weimann, H. Fröb, V.G. Lyssenko, and K. Leo, Frühjahrstagung der Deutschen Physikalischen Gesellschaft, Berlin (2008)

Sub-nanojule threshold lasing in $5 \times 5\,\mu m^2$ organic photonic boxes – Invited Talk
M. Langner, M. Sudzius, S.I. Hintschich, H. Fröb, V.G. Lyssenko, and K. Leo, SPIE

Photonics Europe, Strasbourg (2008)

Organic photonic dot microcavities - a step towards novel laser sources
M. Langner, H. Fröb, M. Sudzius, S.I. Hintschich, V.G. Lyssenko, and K. Leo, ICEL-7, Dresden (2008)

Selective excitation of lasing modes in organic photonic dots
M. Langner, E. Siebert, S.I. Hintschich, M. Sudzius, H. Fröb, V.G. Lyssenko, and K. Leo, EOS Annual Meeting, Paris (2008)

Polarisation splitting of localised states in organic photonic dots
E. Siebert, M. Langner, M. Sudzius, S.I. Hintschich, H. Fröb, V.G. Lyssenko, and K. Leo, EOS Annual Meeting, Paris (2008)

In-plane structured planar organic microcavities: Special optical features and laser performance – Invited Talk
M. Langner, F. Becker, E. Siebert, M. Sudzius, H. Fröb, Lyssenko V., and K. Leo, IMR Workshop on Organic Light Emitting Devices, Sendai (2009)

Electrically pumped organic microcavity-GaN-hybrid system
R. Brückner, M. Langner, D. Kasemann, H. Fröb, V.G. Lyssenko, and K. Leo, Frühjahrstagung der Deutschen Physikalischen Gesellschaft, Dresden (2009)

Nanocrystal quantum dots as emitters in DBR microcavities
J. Haase, T. Otto, M. Langner, D. Dorfs, H. Fröb, A. Eychmüller, and K. Leo, Frühjahrstagung der Deutschen Physikalischen Gesellschaft, Dresden (2009)

Selective excitation of coherent modes in photonic boxes
M. Langner, S.I. Hintschich, M. Sudzius, H. Fröb, V.G. Lyssenko, and K. Leo, Optics of Excitons in Confined Systems 11, Madrid (2009)

Dependence of the polarization splitting on mode tuning in organic microstructures
F. Becker, E. Siebert, M. Langner, M. Sudzius, H. Fröb, V.G. Lyssenko, K. Leo, and C. Adachi, Optics of Excitons in Confined Systems 11, Madrid (2009)

Cavity-enhanced two-photon optical pumping of organic microcavity lasers
M. Teich, M. Langner, M. Sudzius, V.G. Lyssenko, H. Fröb, and K. Leo, EOS Topical Meeting on Optical Microsystems, Capri (2009)

Polariton local modes and supermodes in planar microresonators
V.G. Lyssenko, M. Langner, S.I. Hintschich, H. Fröb, and K. Leo, International symposium on nanophotonics and nanoelectronics, Nizhny Novgorod (2010)

Laser characteristics of small-molecule organic microcavities – Invited Talk
M. Sudzius, M. Langner, S.I. Hintschich, H. Fröb, V.G. Lyssenko, and K. Leo, OPTIMI10, Dresden (2010)

Contents

1   Introduction

"A laser is a solution seeking a problem." [1] – this statement, attributed to T.H. Maiman, the developer of the first laser [2], described very well the situation 50 years ago. Although most of the common laser types (He-Ne [3]-, GaAs [4]-, and dye [5, 6]-laser) were realized in the same decade, they were just gradually introduced into their fields of application. Nowadays, many areas of life are directly or indirectly affected by this special form of light, e.g. material processing, medicine, communication/multimedia, or science, which suggests the laser to be one of the most important inventions of the last century. Still, there exist numerous applications which could benefit from some of the unique properties, such as the good spatial and temporal coherence, high brilliance, or low divergence mostly accompanied by a high energy density. When, on the other hand, multiple laser emission wavelengths are combined in a tricky way, it is already possible to monitor processes on the attosecond scale [7], which gives the opportunity to understand atomic transitions or chemical reactions in detail. In recent years, more and more of the large, unwieldy lasers are substituted with semiconductor (pumped) devices, where the late intensive research yielded progressively smaller efficient devices at many wavelengths and increasing power. Nevertheless, the whole visible spectrum will hardly be covered by the use of inorganic matter as emitter, as the selection of materials, which exhibit stimulated emission at a useful efficiency, is rather restricted. The mostly narrow transition lines at fixed energetic positions allow just a slight variation within the spectrum, thus leaving many practically unused wavelengths. This problem could be overcome by dye lasers, which can cover the whole region from UV to IR light. Their current disadvantage of a high consumption of solved emitter molecules and the necessary optical pumping with an additional laser reduces their usage. This is one of the points, which drives the research on organic solid state lasers to combine a simple electric operation with a high spectral tunability. Furthermore, it is expected that a final product can be fabricated in a comparably simple process, such as vapor deposition or printing. This will positively affect the costs per unit, thus allowing to adress a large market and new fields of application.

The first step towards such a device has been taken in 1987 with the development of the organic light emitting diode (OLED) [8]. Although some problems still needs

to be adressed (e.g. lifetime, environmental stability), these devices are regarded as one of the important future displays and lighting sources with already commercially available products (Sony XEL-1, Samsung AMOLED, Philips Lumiblade, Osram Orbeos). In 1996, Tessler et al. [9] observed stimulated emission from thin organic dye layers. Since then, many resonator designs and material classes have been succesfully investigated [10–16]. Although the processes and materials continuously advanced, no serious demonstration of an electrically driven organic solid state laser was given yet. Theoretical assessments assume huge current densities, which are hardly sustainable by the current choice of organic molecules. It is thus straightforward to study methods, which increase the coupling of light to the respective laser mode and to decrease the losses of the system.

A promising method is the reduction of the active mode volume, which has been successfully applied during the last years in inorganic systems with photonic structures on the wavelength scale [17–21]. In organic systems, Adawi et al. [22] demonstrated a positive effect on the emission properties of micro-structured fluorescent dye films. Besides the stronger interaction of the excited molecules with the modes of the resonator, an alteration of the spectrum, dispersion, and lasing parameters occurs in such structures. This is on one hand attributed to the increased achievable ratio of Q/V, with Q as the quality factor and V as the active mode volume of the resonator. This leads via the Purcell effect [23] to an enhanced spontaneous emission rate. On the other hand, the modification of the density of states reduces the number of possible emission channels, which in combination with the better coupling is advantageous for the development of a low threshold laser. A detailed investigation of the properties of laterally confined systems and a comparison with standard solid state organic dye lasers is within the scope of this thesis.

Samples on the base of $\lambda/2$-thick organic vertical surface emitting lasers (OVCSELs) are therefore modified in the lateral plane and the resulting effects on the optical characteristics are studied. The common resonator is a symmetric dielectric Bragg reflector (DBR) microcavity (MC), consisting of quarter wavelength thick titanium dioxide and silicon dioxide layers prepared in a physical vapor deposition process in high vacuum. The achieved reflectivity of the mirrors typically exceeds 99% at the resonance wavelength, which in combination with the employed highly efficient fluorescent dyes supports stimulated emission at moderate excitation power.

By the use of shadow mask and shutter technologies during the evaporation process of the organic emitter molecules, different heights and material compositions are realized in the central cavity layer. The strongest modification of the optical properties is shown in three-dimensionally confined photonic dots, which are posts of square shape with a width of 5μm at $\lambda/2$ height. These structures restrict the otherwise unlimited in-plane field components into a set of discrete states due to the additional reflection

of photons at the boundaries. In transmission and emission experiments, the modification of the spectrum is explored and modeled with a simple analytical approach. The major experimental setup comprises a microscope stage, with the sample mounted on a micrometer stage in the focus of two high resolution objectives. The signal is recorded with a cooled matrix charge coupled device (CCD) after the spectral decomposition in the monochromator. The good spatial and spectral resolution is used for the closer analysis of a large polarization splitting of the discrete states of photonic dots. Its nature can be attributed to a different effect than the splitting, which arises in detuned DBR microcavities. The experimental results of both types are simulated with numerical approaches based on different models.

The influence of the microstructured system on the lasing parameters of an OVCSEL is analyzed in the following. To get an impression of the values, results of planar microcavities with different emitter concentrations in the same sample are shown first for comparison. Then, the stimulated emission of a single mode of the photonic dot is regarded, which shows an improved coupling of the photons to the resonant state and thus a reduced threshold power. Contrary to standard microcavities, where the lasing is restricted to the principal state, it is possible to observe stimulated emission simultaneously from several states with similar efficiencies but at various directions and wavelengths. It is furthermore shown, that an inhomogenous distribution of inversion or gain by a partial excitation of the structure allows for a type of laser mode selection. In the end, the focus lies on the optical influence of metal interfaces, embedded in the organic cavity layer. The experiments are necessary to understand the passive effect of potential electrical contacts. The high absorption of metals at the emission wavelengths in the visible spectrum is accompanied with a low refractive index, which induces a disruption of the uniform emission layer. The thus created weak confinement has an influence on the lasing threshold, as is shown in experiment and simulation.

In summary, the obtained results present a quite robust system, which can work as starting-point to improve the design of organic microcavity systems and leave a positive conclusion regarding a possible realization of electrically pumped organic solid state lasers.

The thesis is divided into 6 chapters. At first, a brief overview of the basic theory and the employed concepts is given. This is followed by the description of the general sample composition and processing techniques as well as the involved analyzing methods and systems. Chapter 4 presents the spontaneous emission properties with the emphasis on polarization dependence of the spectral features. The lasing performance of laterally modified systems is investigated in the next part, where the coupling efficiency, stability and multimode behaviour is demonstrated. Additionally, the effect of absorptive elements incorporated in the resonator layer is demonstrated. The conclusion and outlook part completes the work.

2 Optical properties of dielectric microresonator systems

The following sections shall give a brief overview of the physical mechanisms of the investigated systems and present methods to describe them. Commencing with basic thin-film optics and the transfer matrix algorithm as a powerful tool to quickly characterize complex designs, the properties of one- and multi-dimensional resonators are introduced. Subsequently, the standard rate equation and applied alterations are explained, which describe the transition from spontaneous to stimulated emission in a microcavity laser. Finally, the optics of waveguides is discussed, since it can be employed for the description of three-dimensionally confined resonators.

2.1 Planar electromagnetic waves at interfaces

2.1.1 Optical constants and their physical meaning

The electromagnetic description of optical phenomena in nonempty space can be reduced to the set of material-dependent Maxwell-equations [24]:

$$\nabla \cdot \mathbf{D} = 0 \tag{2.1}$$

$$\nabla \cdot \mathbf{B} = 0 \tag{2.2}$$

$$\nabla \times \mathbf{E} = -\frac{\partial \mathbf{B}}{\partial t} \tag{2.3}$$

$$\nabla \times \mathbf{H} = \frac{\partial \mathbf{D}}{\partial t} \quad , \tag{2.4}$$

given that no free charges ρ_F or current fluxes j_F are present. The free-space electric and magnetizing fields $\mathbf{E}$ and $\mathbf{H}$ are linked to the electric displacement $\mathbf{D}$ and the magnetic field $\mathbf{B}$ via the relations:

$$\mathbf{D} = \epsilon_0 \epsilon_r(\omega) \mathbf{E} \qquad \mathbf{B} = \mu_0 \mu_r(\omega) \mathbf{H} \quad . \tag{2.5}$$

These equations involve the frequency-dependent, material-dependent relative permittivity $\epsilon_r(\omega)$ and permeability $\mu_r(\omega)$, which describe the reaction of matter towards electromagnetic fields. In the following, the magnetic constant $\mu_r(\omega)$ will not be regarded further, since it is unity for the non-magnetic materials used in this work.

When an electromagnetic wave enters a medium, its atomic components undergo a time-dependent deflection or alignment, which is determined by various parameters, e.g. charge distribution, elementary interaction strength, or molecular moments of inertia. Thus, the material oscillators can have multiple resonance frequencies ω_{0j}, which define the reaction to alternating fields at a given frequency ω. Solving the classical equation of motion [24] for this case, one obtains an expression for the relative permittivity:

$$\epsilon_r(\omega) = 1 + \frac{q^2 N}{\epsilon_0 m} \sum_j \frac{f_j}{\omega_{0j}^2 - \omega^2 + i\gamma_j \omega} \quad , \tag{2.6}$$

which contains the charge q, mass m, and density N of the deflecting particles, their jth resonance frequency ω_{0j} with the respective oscillator strength f_j and a damping factor γ_j. Substituting $\epsilon_r(\omega)$ with the refractive index $n(\omega)$, and accounting for the inducing fields of neighboring charges in dense media, one gets:

$$\frac{n^2(\omega) - 1}{n^2(\omega) + 2} = \frac{q^2 N}{3\epsilon_0 m} \sum_j \frac{f_j}{\omega_{0j}^2 - \omega^2 + i\gamma_j \omega} \quad . \tag{2.7}$$

Splitting the equation for $n(\omega)$ into its real and imaginary part $n(\omega) = n'(\omega) + i\kappa(\omega)$ gives the refractive index $n'(\omega)$ and a component $\kappa(\omega)$ accounting for the absorption, which is called the extinction coefficient. If non-zero, this coefficient is typically positive and determines the amount of energetic losses of the incident wave in the medium, often resulting in heat generation. In case of inverted media, the intensity of the electromagnetic wave can be enhanced, which can be treated as a negative loss.

Following equation 2.7, the real index varies slowly when the frequency ω of the external field is far away from a resonance ω_0 and can thus be regarded as a constant. When approaching an absorption band, the dispersion changes more strongly and turns from normal to abnormal, which means that the derivative $dn'/d\omega$ changes its sign to negative. This behaviour can also be described by the KRAMERS-KRONIG-relation, which links the absorption of a material to its refractive index.

Knowing $n'(\omega)$ and $\kappa(\omega)$, one can determine the phenomenologically observed absorption of a lossy material of thickness d from

$$A(\omega) = 1 - I/I_0 = 1 - exp(-\frac{2\omega n(\omega)' \kappa(\omega)}{c} d) \quad , \tag{2.8}$$

with I_0 and I being the intensity of the electromagnetic wave before and after the

layer, and c as the speed of light. For the two measures of the reflectivity R and transmission T, one has to analyze the amplitude relations of an electromagnetic wave at an interface, which is shown in the next section.

2.1.2 Fresnel formulae of polarization dependent reflection and transmission

Many of the observed optical phenomena in this work do not require a full solution of the Maxwell-equations, since their origin is often an interface effect of multiple layers of media. For this purpose, the Fresnel formulae provide a better and faster way to determine the transmitted and reflected part of light. For the derivation, an electromagnetic wave where the field vectors of $\mathbf{E}$, $\mathbf{H}$ and the direction $\mathbf{k}$ form a right-handed system (transverse electro-magnetic – TEM) is considered. When this field approaches a planar surface, it can be separated without loss of generality into a part with the electric field vector perpendicular to the incident plane (s-polarized, transverse-electric – TE), and another one parallel (p-polarized, transverse-magnetic – TM). In both cases, one has to consider three coupled fields, the incident, the reflected, and transmitted one (Fig.: 2.1). The tangential field components of $\mathbf{E}$ and $\mathbf{H}$ are always continuous. Applying the relation $\mathbf{H} = \sqrt{\frac{\epsilon}{\mu}}\frac{\mathbf{k}}{k} \times \mathbf{E}$, which connects the components of
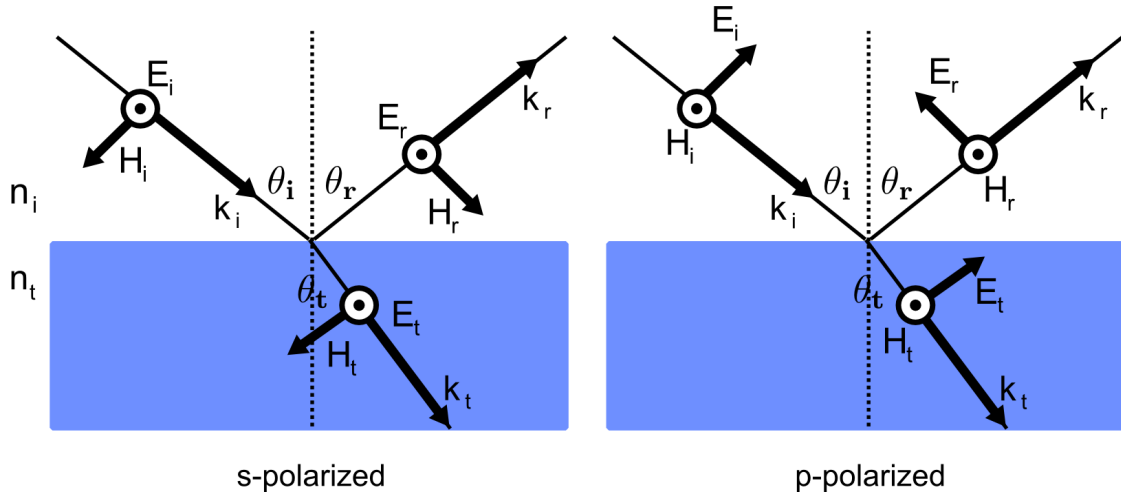
Figure 2.1: Vectors of the electric and magnetic field component $\mathbf{E}$ and $\mathbf{B}$ with directions $\mathbf{k}$ at the interface of two materials with refractive indices n_i and n_t for s- and p-polarized light.

the transversal wave and $n = \sqrt{\epsilon\mu}$, one can write for s-polarized light:

$$E_i + E_r = E_t \tag{2.9}$$

$$\sqrt{\frac{\epsilon_i}{\mu_i}}(E_i - E_r)\cos\theta_i = \sqrt{\frac{\epsilon_t}{\mu_t}}E_t\cos\theta_r \tag{2.10}$$

and for p-polarized light:

$$(E_i - E_r) \cos \theta_i = E_t \cos \theta_t \tag{2.11}$$

$$\sqrt{\frac{\epsilon_i}{\mu_i}}(E_i + E_r) = \sqrt{\frac{\epsilon_t}{\mu_t}}E_t \qquad . \tag{2.12}$$

The reflection and transmission coefficient is then determined by the ratio of the reflected or transmitted field component and the incident one. Again, for the non-magnetic materials in this work, one can set μ to unity and replace the dielectric constant with the refractive index and obtain:

$$r_s = \frac{n_i \cos \theta_i - n_t \cos \theta_t}{n_i \cos \theta_i + n_t \cos \theta_t} \qquad t_s = \frac{2n_i \cos \theta_i}{n_i \cos \theta_i + n_t \cos \theta_t} \tag{2.13}$$

$$r_p = \frac{n_t \cos \theta_i - n_i \cos \theta_t}{n_i \cos \theta_t + n_t \cos \theta_i} \qquad t_p = \frac{2n_i \cos \theta_i}{n_i \cos \theta_t + n_t \cos \theta_i} \qquad . \tag{2.14}$$

To determine the measured values of reflection R and transmission T from these amplitude ratios, one needs to involve the intensity of the field, which can be calculated via the time-averaged Poynting-vector:

$$I = \langle S \rangle_T = \frac{c\epsilon_0}{2}E_0^2 \qquad . \tag{2.15}$$

If the transmission is defined as the ratio of transmitted and incident power and the reflection is evaluated equivalently, one gets:

$$T = \frac{n_t \cos \theta_t}{n_i \cos \theta_i}\left(\frac{E_t}{E_i}\right)^2 = \left(\frac{n_t \cos \theta_t}{n_i \cos \theta_i}\right)t^2 \qquad R = \left(\frac{E_r}{E_i}\right)^2 = r^2 \qquad . \tag{2.16}$$

Since the above consideration neglects loss effects in the materials, it is necessary to add the absorption A in a layer for the measurement of real materials to obtain the transmitted part of the incident intensity. In this work, two types of systems can be classified, nearly lossless multilayer structures and absorbent dyes. For the former, equation 2.16 is sufficient to describe the measures of transmission and reflection, whereas for the latter, a measurement of the transmission will always include the absorption, due to much higher κ values in the spectrally interesting region.

2.1.3   Transfer matrix algorithm

The Fresnel-formulae give the ratio of transmitted, reflected, and incident light at a single interface for a given angle and polarization. For the description of wavelength-scale complex layer systems, which are infinitely extended perpendicular to the propagation axis, the transfer matrix algorithm can be applied. The aim is to express the optical
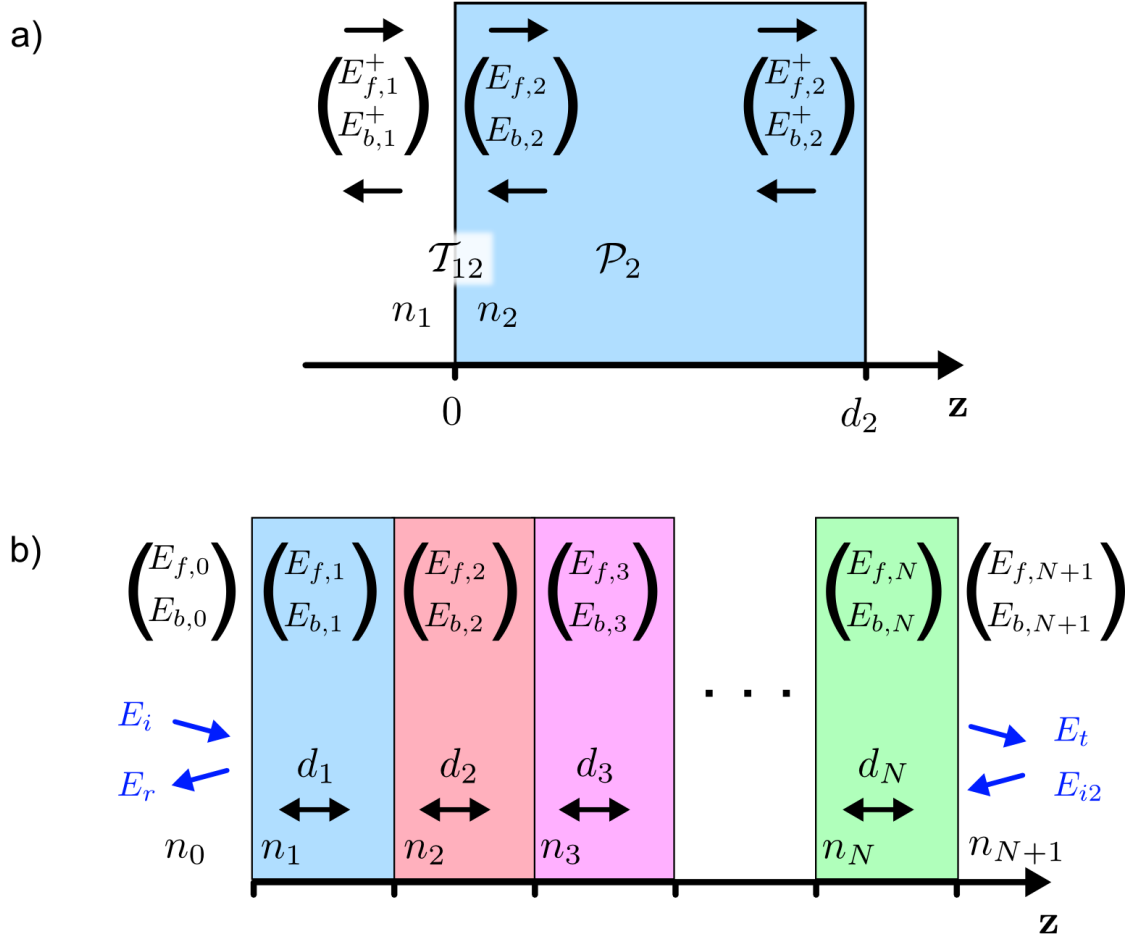
Figure 2.2: a) A single interface and layer of thickness d_2 with corresponding transfer matrix components. b) A multilayer stack, as used in the simulations, with the incident, reflected and transmitted field indicated. The 2nd incident field E_{i2} is often set to zero for simplicity.

properties of the various layers with several matrices [25], to obtain a single matrix, which connects the incident with the exiting fields. For this purpose, an electromagnetic wave is divided into a forward and backward traveling part, of which the amplitudes for each point are represented by a column vector. The behaviour at interfaces and during propagation through a layer of thickness d can be determined via:

$$\begin{pmatrix} E_{f,1}^+ \\ E_{b,1}^+ \end{pmatrix} = \mathcal{T}_{12} \cdot \begin{pmatrix} E_{f,2} \\ E_{b,2} \end{pmatrix} = \frac{1}{t} \begin{pmatrix} 1 & r_{12} \\ r_{12} & 1 \end{pmatrix} \cdot \begin{pmatrix} E_{f,2} \\ E_{b,2} \end{pmatrix} \tag{2.17}$$

$$\begin{pmatrix} E_{f,2} \\ E_{b,2} \end{pmatrix} = \mathcal{P}_2 \cdot \begin{pmatrix} E_{f,2}^+ \\ E_{b,2}^+ \end{pmatrix} = \begin{pmatrix} e^{i\phi_2} & 0 \\ 0 & e^{-i\phi_2} \end{pmatrix} \cdot \begin{pmatrix} E_{f,2}^+ \\ E_{b,2}^+ \end{pmatrix} \quad . \tag{2.18}$$

with the transmission matrix $\mathcal{T}_{12}$, composed of the Fresnel coefficients of transmission and reflection, and the propagation matrix $\mathcal{P}_2$, which determines the phase shift

(Fig. 2.2 a)), when ϕ_2 is:

$$\phi_2 = k_{2,z} d_2 = \frac{2\pi}{\lambda} n_2 d_2 \cos\theta_2 \qquad . \tag{2.19}$$

In this relation, the complex representation of n_2 can be used, and thus absorption losses during propagation are also considered.

For many layers N, a subsequent application of transmission and propagation matrices is performed (Fig. 2.2 b)) to link the fields left and right of the stack:

$$\begin{pmatrix} E_{f,0}^+ \\ E_{b,0}^+ \end{pmatrix} = \prod_{k=1}^{N} (\mathcal{T}_{k-1 k} \mathcal{P}_k) \cdot \mathcal{T}_{N N+1} \cdot \begin{pmatrix} E_{f,N+1} \\ E_{b,N+1} \end{pmatrix} = \mathcal{M} \cdot \begin{pmatrix} E_{f,N+1} \\ E_{b,N+1} \end{pmatrix} \qquad , \tag{2.20}$$

where the terminating 0th and $N+1$th layer is either ambient or substrate. From the matrix $\mathcal{M}$, the reflection coefficient r and transmission coefficient t of the stack can be determined, considering Fig. 2.2 b):

$$\begin{pmatrix} E_i \\ E_r \end{pmatrix} = \begin{pmatrix} M_{11} & M_{12} \\ M_{21} & M_{22} \end{pmatrix} \cdot \begin{pmatrix} E_t \\ 0 \end{pmatrix} \Rightarrow r = \left(\frac{M_{21}}{M_{11}}\right) \quad \text{and} \quad t = \left(\frac{1}{M_{11}}\right) \qquad . \tag{2.21}$$

For structures where the extensions perpendicular to the propagation axis influence the optical properties, it is necessary to use a more complex approach, such as the vectorial transfer matrix algorithm [26] or a numerical model. Simulations within this thesis based on the transfer matrix algorithm are performed with the commercial software FilmWizard from SCI scientific.

2.2   Planar dielectric mirror microcavities

2.2.1   Distributed Bragg reflector

As known from section 2.1.2, any interface between two materials with non-equal refractive indices splits incident light into a transmitted and reflected part, depending on the angle of incidence. For beams entering perpendicular, a ratio of $n_2/n_1 = 1.5$ leads to 4% of the light being reflected, whereas the rest passes the interface. A sequence of multiple interfaces can drastically increase this value, if some constraints are fulfilled. The result is a nearly perfect lossless mirror for a spectral band, called a distributed Bragg reflector (DBR). This device consists of alternating layers of high and low refractive index materials, which should be transparent in the considered wavelength region and having quarter wave optical thicknesses (QWOT), meaning $d_H = \lambda_d/(4 n_H)$ and $d_L = \lambda_d/(4 n_L)$. The wavelength λ_d is called the design wavelength of such a reflector, and defines the spectral position of maximum reflectivity.

From the considerations of the transfer matrix model, the matrix $\mathcal{M}$, which describes a stack of N mirror pairs, starting and ending with the high refractive index material, and surrounded on side one by ambient (n_0) and side two by a substrate (n_S) reads:

$$\mathcal{M} = \mathcal{T}_{0H} \left(\mathcal{P}_H \mathcal{T}_{HL} \mathcal{P}_L \mathcal{T}_{LH} \right)^N \mathcal{P}_H \mathcal{T}_{HS} \quad . \tag{2.22}$$

with

$$\mathcal{T}_{ij} = \frac{1}{2n_i} \begin{pmatrix} n_i + n_j & n_i - n_j \\ n_i - n_j & n_i + n_j \end{pmatrix} \quad \text{and} \quad \mathcal{P}_i = \begin{pmatrix} i & 0 \\ 0 & -i \end{pmatrix} \quad , \tag{2.23}$$

for perpendicular incidence. The resulting matrix $\mathcal{M}$:

$$\mathcal{M} = \frac{1}{2n_0 n_H} \begin{pmatrix} i(n_H^2(-\frac{n_H}{n_L})^N + n_0 n_S(-\frac{n_L}{n_H})^N) & i(n_H^2(-\frac{n_H}{n_L})^N - n_0 n_S(-\frac{n_L}{n_H})^N) \\ -i(n_H^2(-\frac{n_H}{n_L})^N - n_0 n_S(-\frac{n_L}{n_H})^N) & i(n_H^2(-\frac{n_H}{n_L})^N + n_0 n_S(-\frac{n_L}{n_H})^N) \end{pmatrix} , \tag{2.24}$$

can be used to determine the maximum reflectivity of the mirror:

$$R_{max} = \left(\frac{1 - \frac{n_0 n_S}{n_H^2} \left(\frac{n_L}{n_H}\right)^{2N}}{1 + \frac{n_0 n_S}{n_H^2} \left(\frac{n_L}{n_H}\right)^{2N}} \right)^2 \quad . \tag{2.25}$$

The crucial parameters in this relation appear in the exponential fraction $(\frac{n_L}{n_H})^{2N}$, showing the strong influence of the number of layer pairs as well as the ratio between low and high refractive index of the two applied materials. For a few combinations, the behavior of R_{max} is depicted in Fig.2.3(a), indicating the fast approach towards unity.

(a)

(b)

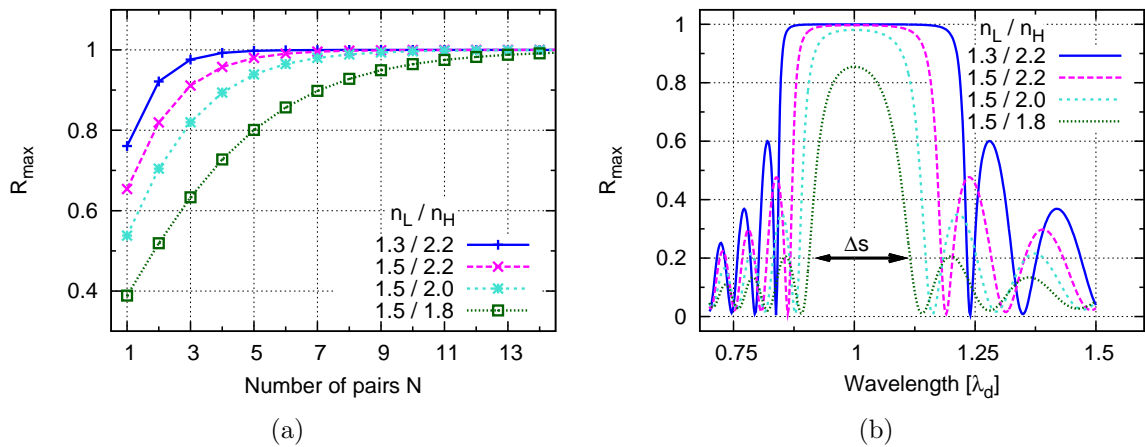**Figure 2.3:** (a) R_{max} dependence on the number of mirror pairs for some combination of n_H and n_L with $n_S = 1.5$ and $n_0 = 1.0$, showing the approach to unity. (b) Reflection spectrum for a lossless mirror of 21 layers of alternating high and low refractive index materials of the given indices. Beside the different maximum reflectivities, the varying stop band widths and edge steepnesses are visible.

For real structures, the number of pairs to obtain a certain maximum reflectivity is higher, since optical losses and imperfect interfaces needs to be compensated. Counter-intuitively, the reflection close to unity is not restricted to the design wavelength, but occurs as a "forbidden band", the so-called stop band of the mirror (Fig.: 2.3(b)). From the general treatment of the transfer matrix [25] follows for its width Δs:

$$\Delta s = \frac{4}{\pi} \sin^{-1} \left(\frac{n_H - n_L}{n_H + n_L} \right) \quad . \tag{2.26}$$

Again, the ratio of high and low refractive index is a crucial parameter controlling the spectral width of the stop band. Left and right of the stop band, the phase shifts in the propagation matrix lead to a complete loss of reflectivity, which is one of the most apparent properties of the dielectric mirror and explains why it can be also regarded as band-stop filter. A bunch of lower reflective side bands appears, which are interrupted by spikes with a transmission of unity.

Another prominent feature of a dielectric mirror is its dispersion, visible with bare eye when a sample is tilted. An estimate expression of the spectral position of maximum reflectivity λ_R versus the incident angle θ is given by

$$\lambda_R(\theta) = \lambda_d \cdot \sqrt{1 - \frac{\sin^2(\theta)}{n_{eff}^2}} \quad \text{with} \quad n_{eff} = \frac{2 n_H n_L}{n_H + N_L} \quad , \tag{2.27}$$

assuming $n_0 = 1$. It shows that with increasing angle, the reflection maximum shifts to shorter wavelengths in a parabolic way with decreasing slope for large angles (see Fig. 2.4(a)).

Whereas the dispersion is not strongly influenced by the polarization, a clear difference for the magnitude of reflection can be seen in figure 2.4(b). This behaviour can be derived from the Fresnel-formulae of a single interface between two materials with different refractive indices. The reflection of p-polarized light increases uniformly to unity with increasing angle, while the amount of reflected s-polarized light decreases to zero (Brewster angle) and then increases to 1. In the resonator, this effect takes place N times below the Brewster angle, resulting in the observed effect.

2.2.2   Bragg reflector resonators

The combination of reflecting surfaces creates a region where electromagnetic waves travel for- and backwards and can form a standing wave, if the relation:

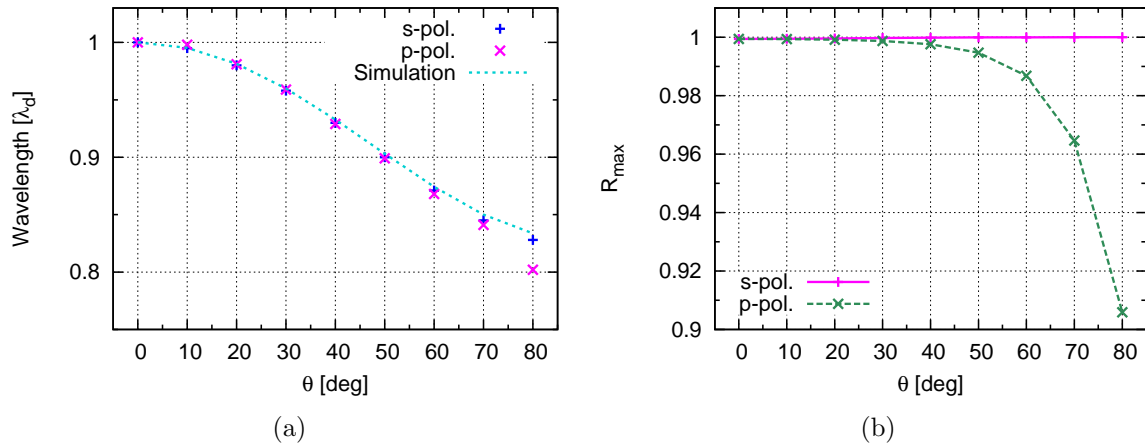$$\lambda_m = \frac{n \cdot L}{2m} \qquad m = 1, 2, 3, ... \tag{2.28}$$

Figure 2.4: (a) Angular dispersion of the reflection maximum for s- and p-polarization, determined from transfer matrix simulations of a 21 layer DBR (dots), with $n_H = 2.2$, $n_L = 1.5$, and $n_0 = 1.0$. The result from equation 2.27 (line) shows a good agreement except for very large incident angles. (b) R_{max} dependence on the incident angle and polarization. While the s-polarized light is stronger reflected with increasing θ, the reflection of the p-polarized field drops remarkably.

between the wavelength λ_m and optical distance $n \cdot L$ is fulfilled. A small resonator length L, especially on the wavelength scale, classifies the system as a microresonator or microcavity. Here, the spectral distance between λ_m and λ_{m+1} can exceed the region, where the surfaces are intrinsically reflective, leaving only a single resonant wavelength. One of the first realizations of such an optical resonator was the Fabry-Perot-etalon, where two plane parallel surfaces partially reflect an incoming beam many times. When the phase difference during the travelled optical path equals a multiple of π, the interference of the multiple beams either cancel the transmitted or reflected part. The major application of this device is thus a lossless spectral filter. With the use of dielectric Bragg mirrors, the quality is enhanced multiple times. As a measure of this, the quality factor Q of the resonator is defined as the ratio of the central wavelength of a transmitted line to its spectral width: $Q = \lambda/\Delta\lambda$. This value becomes larger with increasing reflectivities, as follows from the relation:

$$Q = \frac{(1 + \sqrt[4]{R_1 R_2})^2}{1 - \sqrt{R_1 R_2}} \approx \frac{4}{1 - R} \qquad , \qquad (2.29)$$

where the last approximation assumes symmetric mirrors with reflectivities close to unity. These high Q - factors support very sharp transmission lines (see Fig. 2.5(a)), when the resonant wavelength or so-called cavity mode is located in the center of the stop band, where maximum reflection of the mirrors is present. Photons entering the resonator do not immediately escape, but are reflected and follow on average a number of roundtrips proportional to Q, before they leave the second mirror. Thus, the photon

lifetime within the cavity τ_C is enhanced and a huge electric field can be generated in the cavity layer, exceeding the incident field amplitude many times (see Fig. 2.5(b)). Since this is an interference effect of many involved layers, it is crucially dependent on the specific phase angles. A small deviation of the incident wave from the design wavelength results in a central and output field amplitude (much) less than one, which one would intuitively expect from a successive application of two mirrors.
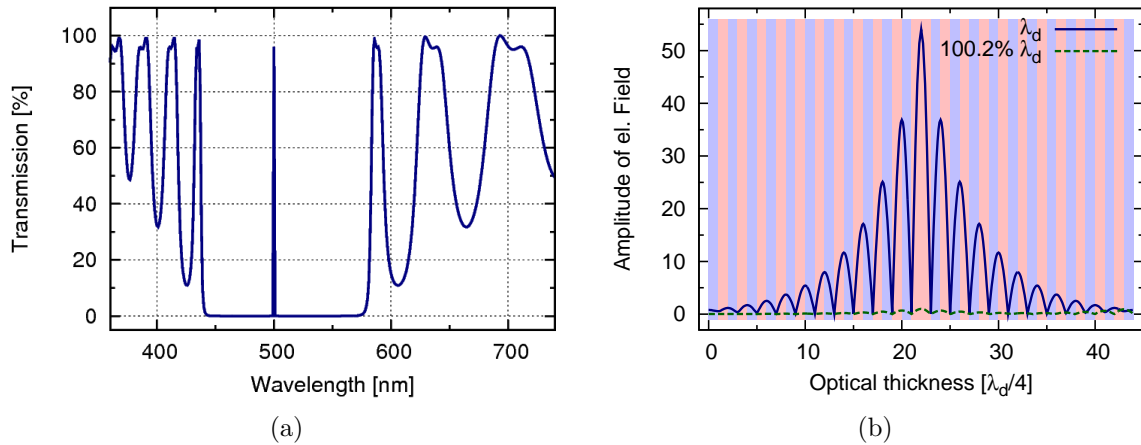

Figure 2.5: (a) Spectrally resolved transmission of a 21 layer DBR microcavity with $n_H = 2.2$ and $n_L = 1.5$ and $\lambda_D = 500\,nm$, showing the stop band with centered cavity mode at $500\,nm$ and highly transmissive side bands. (b) Progression of the electric field in this structure for resonance and slightly above. One can clearly observe the huge enhancement of the field for λ_D.

The aforementioned phase differences which create the transmissive mode also mainly determine the dispersion of a microcavity, as they change with angle. Analogous to the dispersion of the DBRs, one can couple the resonant wavelength λ_c to the incident angle θ in a single mode cavity via:

$$\lambda_c(\theta) = 2n_c L_c \cos(\theta_c) = \lambda_d \cdot \sqrt{1 - \frac{\sin^2(\theta)}{n_c^2}} \quad , \tag{2.30}$$

where n_c is the refractive index and L_c and θ_c are the length and internal angle of the cavity layer, repectively. The second expression relates the resonant mode to the design wavelength λ_d and incident angle assuming a $\lambda/2$ - system, surrounded by air. Figure 2.6 demonstrates the evolution of the stop band and cavity mode with increasing angle. The direct comparison of both polarizations shows two apparent differences, originating from the polarization sensitivity of the Bragg reflectors. The linewidth of the resonant mode decreases significantly for s-polarization, whereas it increases for p-polarization, as a direct consequence of the R_{max} dependence (Fig. 2.4(b)). Furthermore, the width of the stop band changes differently for both polarizations and it becomes partially transparent for p-polarized light at large angles.

The previous considerations are valid for an ideal microcavity, where the resonant wavelength matches the design wavelength of the dielectric mirrors, which is difficult to achieve practically and sometimes also not desired. When the center of the stop band λ_d differs from the cavity resonance wavelength λ_c, one has to introduce an effective cavity length [27, 28], which accounts for different penetration depths of the resonant field into the mirrors. Since this value is different for s- and p-polarization, one can observe a polarization splitting of the resonance, which is dependent on the angle.
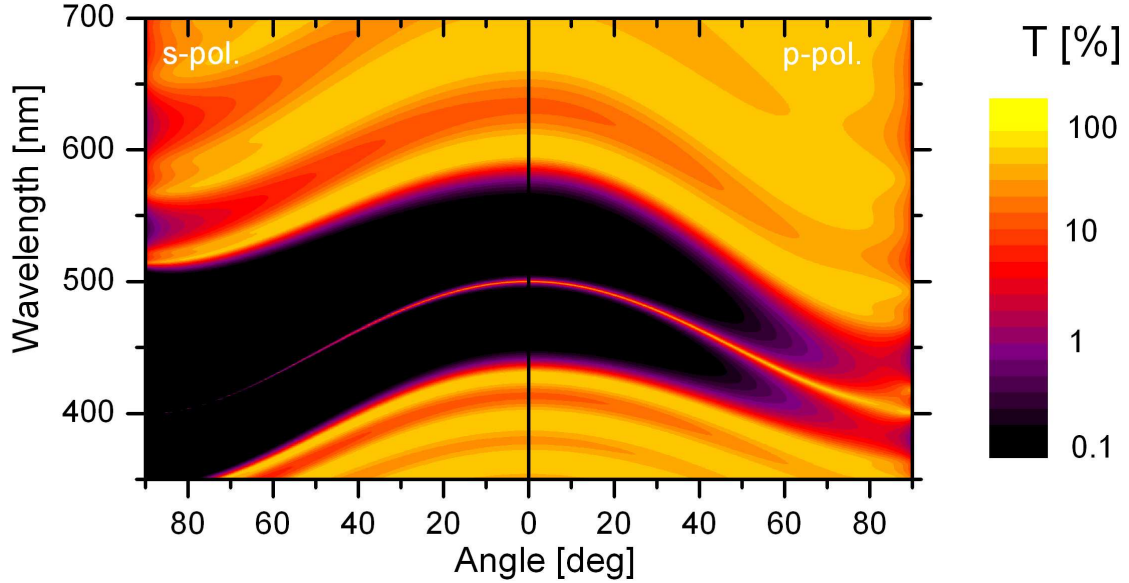

Figure 2.6: Dispersion of a microcavity, simulated for 15 layer DBR (for specifications, see Fig. 2.5(a)), for both polarizations, in log-plot for a better visibility.

2.3 Multidimensionally confined systems

2.3.1 The density of states in quantized systems

Beside a description of the spectral properties of a microcavity, it is useful to analyze the mode density in these systems, especially when it comes to interaction with excitable states in such a system. Generally, for a system undergoing a transition this can be expressed with Fermi's golden rule:

$$\Gamma_{i\to f} = \frac{2\pi}{\hbar}|\langle f|H'|i\rangle|^2\rho \quad , \tag{2.31}$$

where $\Gamma_{i\to f}$ is the transition probability from an initial to final state at small pertuba-tion H' and given density of final states ρ. For the described resonator systems herein, the change of transition probability of the emission from a dipole interacting with a

certain field is of interest, so one can write:

$$\Gamma_{em} = \frac{1}{\tau_{sp}} = \frac{2\pi}{\hbar^2}|\langle|\hat{\mathbf{d}}\cdot\hat{\mathbf{E}}^\dagger_{\mathbf{k},\sigma}|\rangle|^2\rho(\omega) \quad , \tag{2.32}$$

with $\hat{\mathbf{d}}$ as dipole moment operator and $\hat{\mathbf{E}}$ as electric field operator of a mode with certain $\mathbf{k}$ - vector and polarization σ. It was shown in the last section that the electric field is magnified many times for the resonant case, which directly increases the transition probability. However, for the complete determination of the transition rate Γ_{em}, one has to know $\rho(\omega)$. By the introduction of an effective mode density of the optical field $g(k)$, it is possible, to separate equation 2.32 into a quantum mechanical and a classical part [29]. Thus, one can estimate the spectral position of resonances (modes) as well as the impact on the transition strength of the emitter. The cavity mode and its dispersion as seen in figure 2.6 can be regarded as a direct consequence of the altered mode density compared to free space. The available states per solid angle are restricted in the $\lambda/2$ - cavity due to the discrete nature of the perpendicular part of the wave vector.

To obtain the volume normalized mode density for some typical rectangular resonator systems, the method of mode counting is applied, which is described in [29]. It can be summarized into the following steps:

1. Identify available k-states, which are supported by the resonator.

2. Intersect allowed modes with a spherical surface of radius $k = \omega/c$ and width dk, and determine the volume in k - space.

3. Take the sum over all k-space modes, including a "background" density factor and normalize by the cavity volume.

This method gives the resonant modes for perfectly reflecting mirror cavities; for real systems, it would be thus necessary to include losses, or polarization and angle dependent reflectivities. Furthermore, it implies an empty system. If one considers an emitter placed in the center of a microcavity, one needs to regard its specific orientation and thus different interaction strength with a resonant mode. The result are mode densities $g(k)$ for dipoles either parallel or perpendicular to a distinct direction. The experimental spectra are a superposition of the different orientations, as the majority of the investigated systems within this thesis have an amorphous active layer where the dipoles are oriented randomly.

2.3.2 Mode structure in photonic wells, wires, and dots

In the following, the mode density is presented for one, two, and three dimensions of confinement and hence discretization of k_i with $i = x, y, z$. For the photonic well, which

is equivalent to a planar microcavity, one has a discretization of available k_z states due to the wavelength - scale resonator extension L_z, if the z-axis is taken as the cavity normal. Thus, the available states form xy - planes in the k-space, which cross the spherical shell (see figure 2.7(a)). The result are rings, which need to be integrated over and then summed over all planes, fulfilling $|m\pi/L_z| < k$, with m as order number of the discrete z-states.
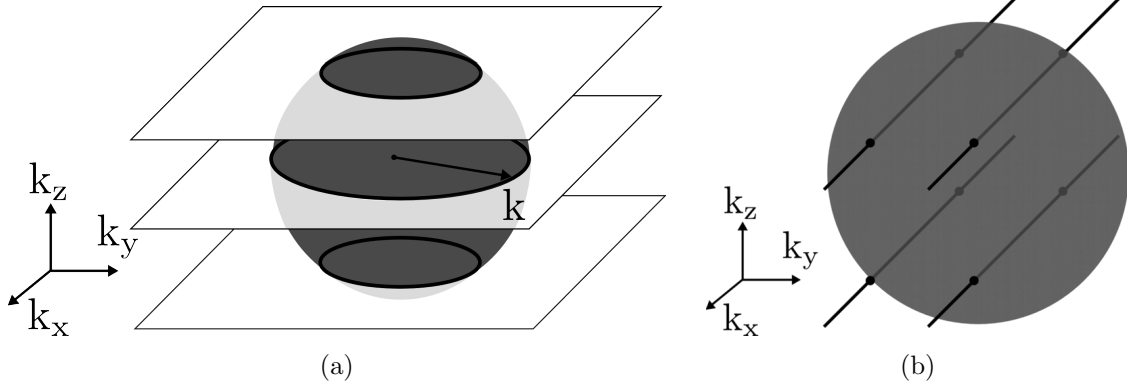

(a)   (b)

Figure 2.7: (a) The k-space representation of the resonant states of a planar microcavity. Due to the discrete nature of the wave vector component perpendicular to the mirrors (k_z), possible k values are restricted to the xy-planes. The intersection with a spherical shell of radius k results in rings, which correspond to the allowed modes for a given frequency $\omega = ck$. (b) Analogous, for a rectangular waveguide, possible resonant states are points, located on lines parallel to the unconfined axis of the resonator.

The density for dipoles parallel to z reads:

$$g_{\parallel}(k) = \frac{1}{2\pi^2} k_c k \sum_{m\,even} (1 - (m\frac{k_c}{k})^2) \quad \text{with the cutoff vector} \quad k_c = \frac{\pi}{L_z} \quad , \qquad (2.33)$$

where the sum restriction accounts for the fact that the parallel dipole couples to even order modes, due to the cosine-type field in z-direction. The evaluation of this sum yields:

$$g_{\parallel}(k) = \frac{1}{2\pi^2} k_c k \left(1 + 2 \left(P - \frac{1}{6} \left(\frac{2k_c}{k} \right)^2 P(P+1)(2P+1) \right) \right) \quad . \qquad (2.34)$$

The value P is the largest integer, less or equal to the ratio of $k/2k_c$. An analogous treatment for the dipoles perpendicular to z gives:

$$g_{\perp}(k) = \frac{1}{2\pi^2} k_c k \left(S + \left(\frac{k_c}{k} \right)^2 \left(\frac{4}{3} S^3 - \frac{1}{3} S \right) \right) \quad . \qquad (2.35)$$

Here, S is the largest integer, less or equal to $\frac{1}{2}(k/k_c+1)$. The normalized mode density

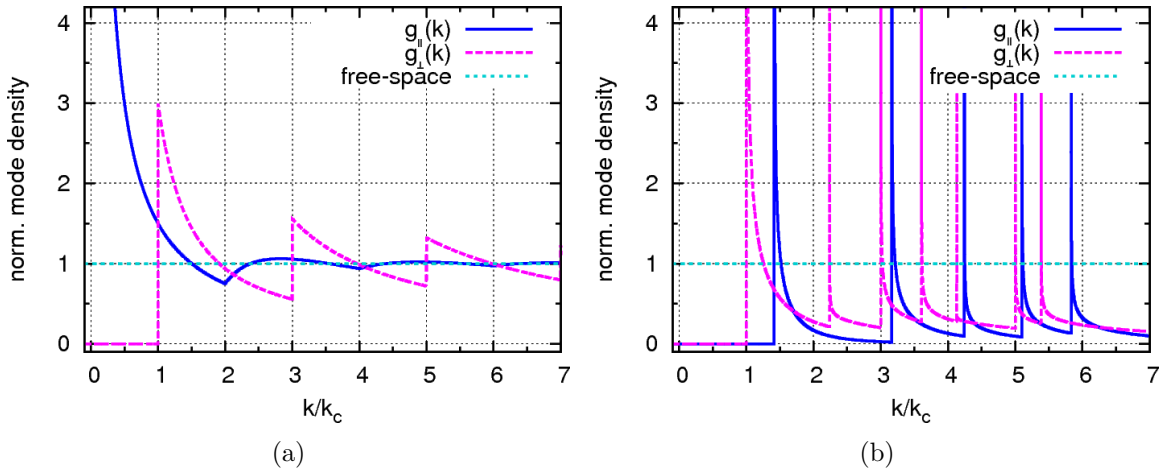with respect to a free space emission is plotted in Figure 2.8(a)

Figure 2.8: (a) Normalized mode density for the case of a photonic well for a parallel and perpendicularly oriented dipole with respect to the confined direction, shown in multiples of the cutoff frequency k_c. (b) The same for a photonic wire with $L_x = L_y$. Values larger than unity imply an enhancement compared to free-space emission, lower than one means a suppression. [29]

From this figure, one can see that the mode density in the confined system is at some points significantly larger or smaller compared to free space, but approaching it in the high frequency limit. For values larger than one, the transition probability of a suitable emitter is increased, which means that it will relax faster, when it is excited. On the other hand, an inhibition of emission occurs, when the value is below one, which would result in the limiting case in an infinite life time [30].

For the majority of the planar resonator samples within this thesis, $\lambda/2$ - cavities are used, which includes that the interesting spectral region is close to the cutoff frequency. This is a result of the broad, but finite emission spectrum of the active material, thus supporting a comparatively small wave-vector range. For both orientations of dipoles with respect to the z-axis, one has an enhancement for k_c which decreases for larger k values. For the perpendicular case, this corresponds to a maximum emission into the direction of confinement, decreasing for oblique angles. The parallel oriented dipole is not contributing to emission directed outwards the cavity, but into the plane. The normalized density is divergent in the low frequency limit, thus exceeding the maximum value of the perpendicular dipoles. In practice, this behaviour is not relevant for a $\lambda/2$-cavity, as no emission occurs within this wavelength region and the dielectric mirrors are not highly reflective anymore.

This is different for a photonic wire, which is a system confined in two dimensions $(L_x, L_y \sim \lambda \ll L_z)$, e.g. a waveguide. The small footprint of such a structure results in a series of lines in k - space parallel to the unconfined direction (z). Again, the procedure of mode counting gives a sum, which in this case cannot be written in a

closed form. The mode density of dipoles parallel to the unconfined direction is related to the cutoff wave-vectors $k_{c,x} = \pi/L_x$ and $k_{c,y} = \pi/L_y$ via:

$$g_{\parallel}(k) \propto \sum_{m \, odd} \sum_{n \, odd} (k^2 - (mk_{c,x})^2 - (nk_{c,y})^2)^{-1/2} \quad , \tag{2.36}$$

and for dipoles perpendicular to z:

$$g_{\perp}(k) \propto \sum_{m \, odd} \sum_{n \, even} (k^2 - (mk_{c,x})^2 - (nk_{c,y})^2)^{-1/2} \quad . \tag{2.37}$$

Both densities, normalized to the free space value, are shown in figure 2.8(b). As already apparent from the equations above, one has singularities at many points, corresponding to multiples of the cutoff wave-vectors. If an emitter has a sufficiently narrow transition which matches the corresponding wavelength at one of these positions, the emission rate will be significantly increased. Beside these narrow bands, the normalized density is lower than one, which means that emission at these k-vectors is suppressed compared to free space.

The last, and in the context of this work, most interesting system is a resonator confined in three dimensions, a photonic dot. Here, all lengths are on the order of the regarded wavelengths, which results in a series of points in k-space. The resonant states can be determined by $k_{mnp}^2 = (m\pi/L_x)^2 + (n\pi/L_y)^2 + (p\pi/L_z)^2$, with m, n, p being integers. The effective mode density for an emitter aligned parallel to e.g. the z direction can then be written as:

$$g(k)dk \propto \sum_{m \, odd} \sum_{n \, odd} \sum_{p \, odd} \frac{p^2}{m^2 + n^2 + p^2} \delta(k - |k_{mnp}|) \quad . \tag{2.38}$$

This result is depicted in figure 2.9. Besides the delta-like discrete resonances, which are defined by the dimensions of the box, the mode density is zero. The modes are not equidistant, but increase quadratically with k. Not visible in the graph is the different magnitude of each resonance, due to a degeneracy of the modes for the cubic case calculated here. A non-square shape in lateral direction will lift this degeneracy and may increase the total number of modes per frequency range. For an emitter in the box, this mode structure effectively means an infinite lifetime for transitions not exactly matching the resonance and an immediate emission when they coincide.

In realistic structures, one needs to account for many effects which alter the considered mode densities. A major role plays the reflectivity of the mirrors, which was assumed unity and frequency-independent. For dielectric mirrors, one further needs to include the polarization of the light and an effective penetration depth of the electric field into the mirror layers in the mode counting algorithm. Additional losses lead all
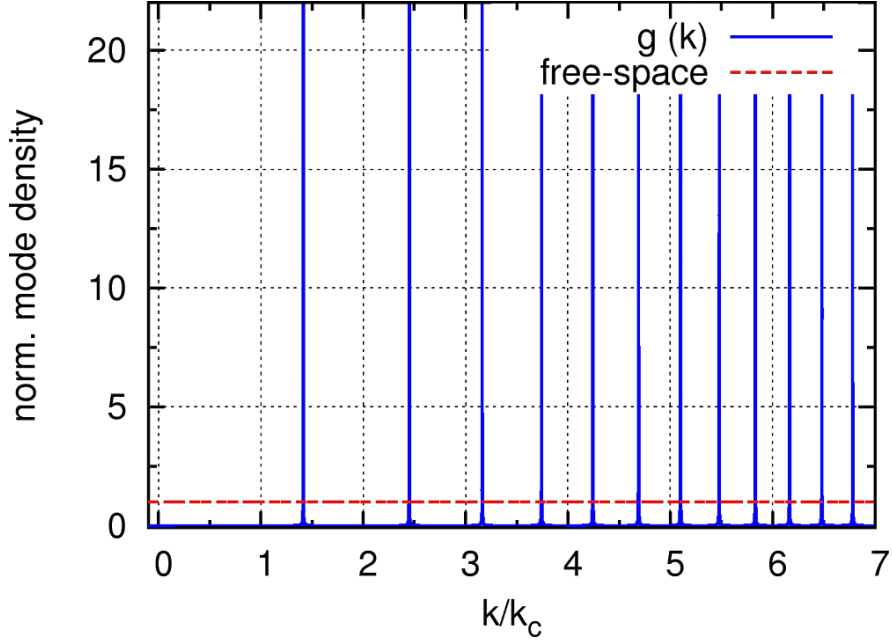
Figure 2.9: Normalized mode density for a photonic dot, with $L_x = L_y = L_z$ and a finite linewidth of the resonances. It is obvious that emission will occur only at positions of cavity resonances, since the density is zero in the residual parts.

in all to a smear-out effect of the peaks in the functions, and an approach towards the free space mode density. In case of the box, the delta-functions are approximated by Lorentzians, with their widths defined by the cavity lifetime.

2.4   Rate equations

2.4.1   Model of Yokoyama

To describe lasing processes in microresonators, it is necessary to estimate the rates of photon creation, inversion, and exit through the mirrors. From the previous section, the altered mode density due to different confinement dimensions is already known. When a dipole in such a resonator interacts with a quasi-single-mode field, the emission rate can be extracted from Fermi's golden rule [31]:

$$\Gamma_{em} \propto \frac{\omega}{V}(s+1)\rho(\omega) = A_r \cdot (s+1) \quad . \tag{2.39}$$

This equation contains the effective mode volume V, the mode density ρ at frequency ω, summarized by the factor of the emission rate into the mode A_r. The coefficient $(s+1)$, with s as the initial number of photons in the resonator describes the spontaneous (factor proportional to 1) and stimulated (factor proportional to s) emission. Assuming that each emitted photon is in resonance with the single existing mode

(closed resonator), one can write for the rate of photons $\dot{s}$ and inverted emitters $\dot{n}$ in the cavity:

$$\dot{s} = A_r(s+1)n - \gamma s \tag{2.40}$$

$$\dot{n} = p - A_r(s+1)n \quad . \tag{2.41}$$

The term γ describes the losses of photons through the mirrors (outcoupling of stimulated emission) and p is the pumping rate of the system. In a stationary state, this laser would be thresholdless, as $s = p/\gamma$. However, even the best confined system has in reality more than one possible emission channel and thus an altered rate equation:

$$\dot{s} = \beta A(s+1)n - \gamma s \tag{2.42}$$

$$\dot{n} = p - (1-\beta)An - \beta A(s+1)n \quad . \tag{2.43}$$

This set of differential equations now contains the factor β, which accounts for the ratio of light, which couples to the mode of interest, whereas the part $1-\beta$ couples to the residual modes of the system. A further difference is the emission rate A in these equations, which is a weighted average of the free space and resonator rates (A_f and A_r). For a weak confinement, it corresponds to the free space value, whereas for strong confinement, it reaches the emission rate of the resonator. Sometimes [32], the notation
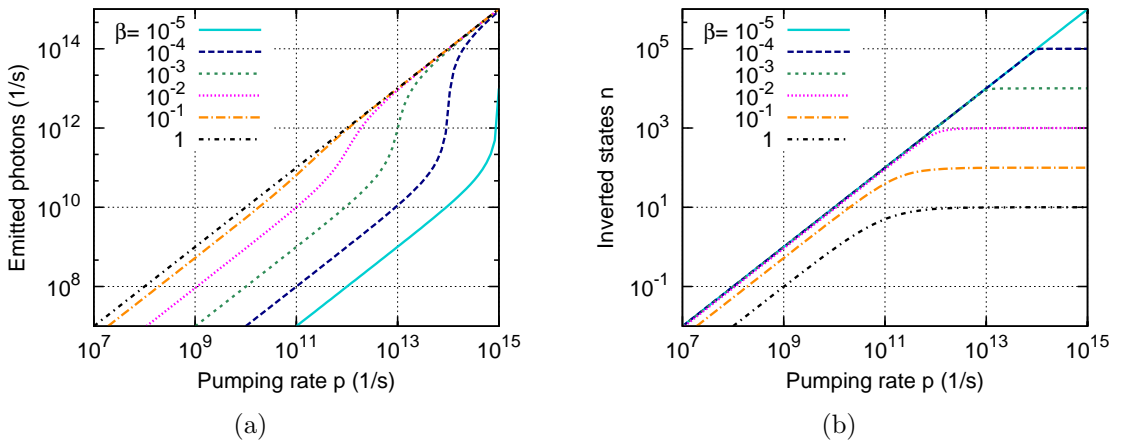
Figure 2.10: (a) Number of emitted photons/s and (b) inverted states n for a given pumping rate p, calculated from equation 2.42, with values of $A_f = 10^9 s^{-1}$, $A_r = 10^{10} s^{-1}$ and $\gamma = 10^{11} s^{-1}$ (after [31]). Whereas in the input-output curves the transition between the spontaneous and stimulated emission regime vanishes with increasing β, the behaviour of the population inversion changes from a linear increase to a constant value, when overcoming the lasing threshold.

of β is used differently, to describe the part of the solid angle which is covered by the cavity mode with respect to the free space modes. For small values of this factor, the difference is negligible, whereas for values close to unity, one has to be careful to avoid

confusion.

In figure 2.10(a), the number of photons emitted into the cavity mode is depicted for various values of β together with the corresponding number of inverted states n (Fig. 2.10(b)), obtained from the steady-state solution of equation 2.42. In this log-log plot, the linear parts of the curves correspond to either mainly spontaneous emitted photons (low pumping region) or mainly stimulated emitted photons (high pumping region). If every emitted photon is in the cavity mode ($\beta = 1$), a transition between both regimes is not visible in the output, whereas for typical resonators, a more or less pronounced super-linear increase of the photon number in the cavity mode defines the threshold. The less photons are confined in the cavity mode, the more power is needed to obtain stimulated emission from the resonator. This effect is also apparent in the graph of the inverted states, as more and more emitters need to be excited before a saturation takes place, equal to $\gamma/(\beta A)$.

2.4.2   Necessary adjustments for the investigated systems

Although the above equations can describe the experimental curves quite well, some deviations occur, which are not explicitly treated in each case but will be explained in the following. The origin of the variations is related to the emitter itself, but also to experimental conditions. For the majority of samples, an organic dye system is employed, where a high percentage of a diluted emitter needs to be inverted to overcome the threshold. This implies inhomogenous broadening of the free space emission, as well as the occurence of saturation due to interferences between the time constants of energy transfer and short pump pulses. The broadening affects mainly the transition between spontaneous and stimulated emission, wheras the second effect may explain differences in the output curves between the various pumping schemes. The organic molecules are present as an amorphous film, which gives rise to a large number of interactions between an emitter and neighboring molecules. The coupling to a specific resonator mode depends on the orientation of the molecules and also the position within the cavity layer. If the stimulated emission starts, only emitters with a good coupling to the mode contribute to the lasing process. If the pumping power is now increased, molecules which do not fit perfectly may start to contribute to the stimulated emission, e.g. with slightly off-resonant transition or located near the node of the field. To include this in the output characteristics, a weighted averaging of the photon density is introduced [33], which treats the inhomogenously broadened system as an ensemble of various homogenously broadened emitters with different β values. The number of photons at some specific frequency ω_e and the average number of photons per mode

can be expressed as follows:

$$s(\omega_e) = \frac{1}{2\gamma}\left[p - \frac{\gamma}{\beta(\omega_e)} + \sqrt{\left(p - \frac{\gamma}{\beta(\omega_e)}\right)^2 + 4\gamma p}\right] \tag{2.44}$$

$$\langle s \rangle = \int_{-\infty}^{\infty} f(\omega_e, \omega_c)s(\omega_e)d\omega_e \quad .$$

The weighting is in the factor $f(\omega_e, \omega_c)$, with ω_e being the frequency of the specific emitter, and ω_c those of the cavity mode. It can be seen in figure 2.11 how the output curve is changed, with a steeper increase and a smoother transition towards the asymptote of the linear lasing regime at high pumping, for f of a Gaussian-type. As can be seen in the graph, the simple average of the β-values of the different emitters gives a different result.
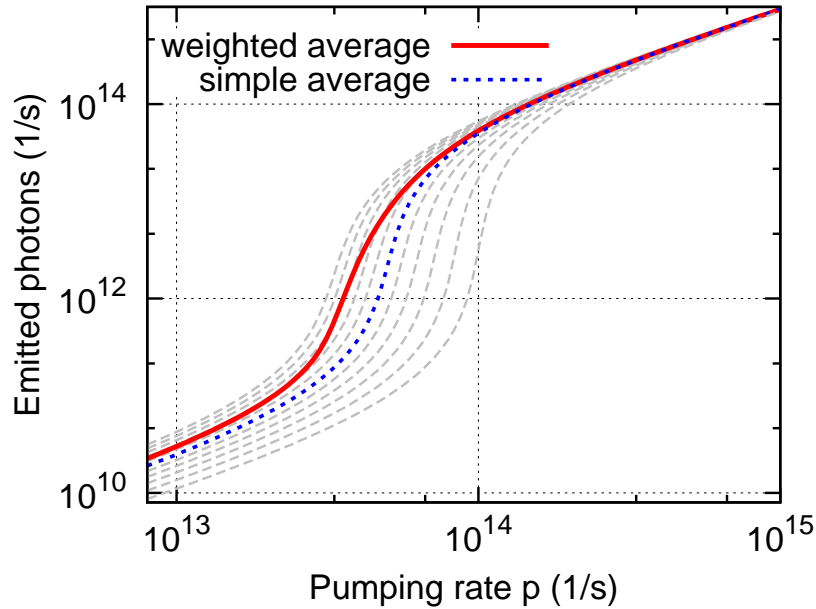

Figure 2.11: Modification of the threshold region by the introduction of an wheigted average photon density $\langle s \rangle$, based on the gray curves of different β values $(1 - 3 \cdot 10^{-4})$ and the photon escape rate $\gamma = 10^9\text{s}^{-1}$. The curve deviates clearly from the average β value in the superlinear transition region.

To consider ultrashort pump pulse effects in the rate equations, a modification is necessary, which accounts for initial excitation and subsequent relaxation [34]. One has furthermore to account for the high fraction of inverted emitters in the pumped region of a guest-host $\lambda/2$-cavity to overcome threshold, which plays a key role for saturation effects. The result of this procedure is comparable to those, presented in [35] for a low emitter count due to the reduced mode volume in microcavities. Within the rate equations, the pump term p is modified by the amount of molecules N_m which separates

into excited (n_e) and ground state (n_g) species via:

$$p \rightarrow p(n_g - n_e) = p(N_m - 2n_e) \qquad (2.45)$$

The excited states have a certain transfer time to the lasing state n, which is accounted for by a rate $k_t n_e$, such that the rate equations now read:

$$\dot{s} = \beta A(s+1)n - \gamma s \qquad (2.46)$$

$$\dot{n}_e = p(N_m - 2n_e) - k_t n_e \qquad (2.47)$$

$$\dot{n} = k_t n_e - (1-\beta)An - \beta A(s+1)n \quad . \qquad (2.48)$$

When the pulse durations are on the order of k_t^{-1}, n_g might be depopulated (the material gets transparent) and a further linear increase of photons in the lasing regime is not possible (see figure 2.12(b)). For longer pulses, a successive photon emission of the molecules can contribute to a further increase of measured photons from the cavity by an integration during the detection, although the actual maximum number is limited by the relation between cavity life time τ_C and k_t^{-1}.
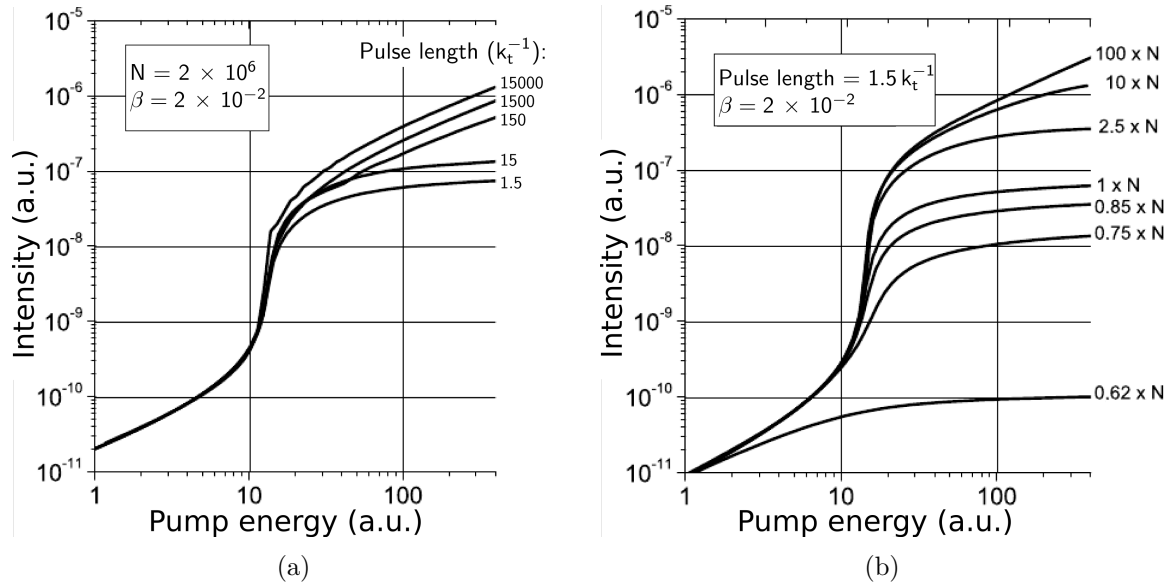
Figure 2.12: (a) Input-output curves calculated from the time-integrated solution of the modified rate equations for constant emitter concentration and various pulse lengths. When the pumping energy is distributed over a longer period, multiple excitation processes can contribute to an overall higher intensity. (b) The same situation for a constant pulse duration, but a different total number of emitters. A saturation effect for low concentrations can be seen directly after the onset of lasing. The simulation parameters are correlated to typical microcavities containing 2wt% of DCM and the different thresholds of the curves have been aligned for better comparability. (after [34])

The asymptotic approach towards a maximum intensity instead of the linear in-

crease of p/γ can also be seen in figure 2.12(a), where various emitter concentrations are shown for a short pulse length. The lowest concentration stays in the spontaneous emission regime, whereas a high concentration assures a linear increase orders above threshold. In sum, the relation between the field enhancement, the coupling of light into a mode and the emitter number is crucial for the functionality and emission property of a microcavity laser. On the other hand, one has to be careful when extracting the coupling factor β of a measured input-output curve. As it can be seen in figure 2.12(b), the initial part after the threshold kink could be misinterpreted as the beginning of the mainly stimulated emission regime suggesting a 10 times smaller β.

2.5   Waveguide theory

2.5.1   Light propagation in a dielectric channel

Although a guiding of waves is not wanted in case of microcavity lasers, as this light cannot exit the structure, the theory can be used to approximate the resonant modes of a structured resonator, e.g. a photonic dot. Generally spoken, a waveguide is a device with one or two dimensions on the desired wavelength scale, and a refractive index n_w larger than the surrounding n_s. Thus, it is possible to channel photons without losses by total internal reflection. When z is the propagation direction, the electric and magnetic fields of the waveguide can be obtained directly from Maxwell's equations [25]:

$$\mathbf{E}(x,y,t) = \mathbf{E}_m(x,y)\exp[i(\omega t - k_z z)] \tag{2.49}$$

$$\mathbf{H}(x,y,t) = \mathbf{H}_m(x,y)\exp[i(\omega t - k_z z)] \quad, \tag{2.50}$$

where the subscript m denotes the respective mode number. This set of equations would allow any mode, so one has to introduce boundary conditions. The propagation constant k_z is limited in the following manner:

$$\frac{n_s \omega}{c} < k_z < \frac{n_w \omega}{c} \quad, \tag{2.51}$$

to obtain guided modes. An application of ray optics or the use of the continuity conditions of the fields at the interfaces leads to the solutions of the modes $\mathbf{E}_m$ and $\mathbf{H}_m$, either graphically or numerically.

2.5.2   Resonant modes

One can imagine the path of a photon in a waveguide mode as a zigzag path (see figure 2.13). Beside the condition of total reflection of the light at the boundaries, it

is necessary that the total phase shift of the traveled path L is an integral multiple of 2π. As the phase shift during reflection at the sidewalls depends on the polarization of the mode, the propagation constant k_z and such the frequency ω_m is different, which leads to a splitting. In a a symmetrical waveguide with square shaped footprint, the resonant modes have an increasing number of antinodes in their intensity cross section, the smaller the propagation constant k_z becomes, which corresponds to a steeper angle towards the interface (see figure 2.13).
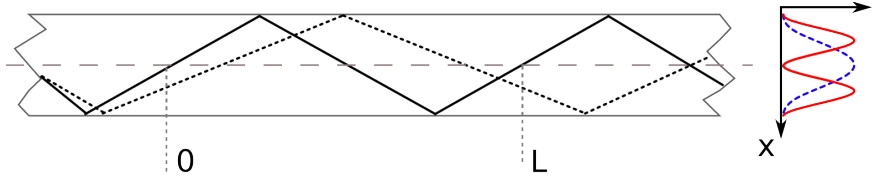

Figure 2.13: Zigzag path of the first two modes in a symmetric waveguide and the intensity profile of a cross section. To fullfil the resonant condition, it is necessary that the phase shift of the bouncing ray between 0 and L is a multiple of 2π.

Aside from the specific transverse field distribution, some properties are common for waveguides, regardless of their geometry. It can be shown [25] that the surface integrated scalar product of the field of two modes vanishes:

$$\iint \mathbf{E_1} \cdot \mathbf{E_2} \, dx dy = 0 \quad . \tag{2.52}$$

Thus, the resonant modes are orthogonal, furthermore they can be normalized to form an orthonormal system. In this case, the sum of the power of each mode gives the total power flow of the waveguide. Another feature may occur when the dieletric tensor of the guide $\epsilon(x, y, z)$ is not homogenous, but has (small) differences, expressed as pertubations $\Delta\epsilon(x, y, z)$. The application of pertubation theory and orthonormality on the transverse wave equation reveals a coupling of modes. This effectively means that the energy of a single excited mode can be transfered to other modes, which then build up during propagation of the wave. This effect also connects modes of different polarization and its strength is proportional to the pertubation $\Delta\epsilon$.

2.5.3   Influence of positive and negative optical losses

To include the effects of absorption or gain, it is necessary to use the complex dielectric function in the wave equation:

$$\left[\nabla^2 - \partial^2/\partial z^2 + \left(\frac{\omega^2}{c^2} n^2(x, y) - k_z^2 \right) \right] \mathbf{E_m}(x, y) = 0 \quad . \tag{2.53}$$
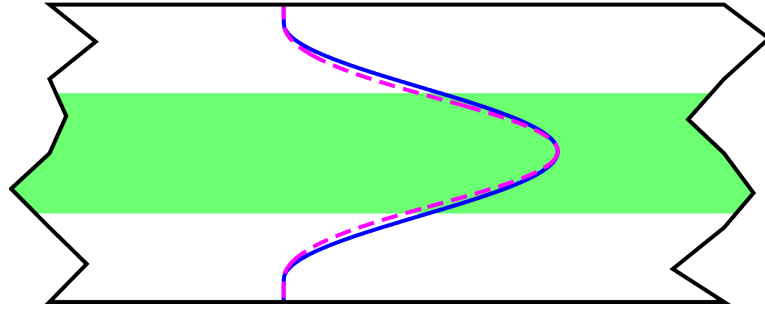
Figure 2.14: Modification of the normalized transverse field intensity distribution induced by a region with gain in the center of the waveguide (calculated numerically). The altered field (dashed) is more concentrated in the center in comparison to the mode of a lossless guide (straight).

Often, the complex part of n^2 is in the notation added to the propagation constant, which then decreases for lossy waveguides or increases in an inverted medium. When it comes to more complex designs, e.g. lossy waveguides with gain sections in the xy-plane, the field distribution of a certain mode becomes deformed. Furthermore, one can derive an integral or net absorption κ_m of a mode, which determines whether it will be damped ($\kappa_m > 0$) or amplified ($\kappa_m < 0$) during propagation. This depends not only on the amount of loss, but also on the overlap of a certain mode with the gain region. As a consequence of the modified transverse field profile (see figure 2.14), the resonant frequencies are also shifted.

3 Sample fabrication and characterization

This chapter discusses the experimental steps towards high quality resonator samples and the subsequent characterization setups. At the beginning, the standard processing of the dielectric mirrors and the organic emission layers is presented. This is followed by the description of some techniques, developed and applied within this work, to enhance or modify the properties of the microcavity samples. The last section covers the various measurement setups used for the investigation of the optical features.

3.1 Basic microcavity preparation techniques

3.1.1 High vacuum deposition of thin layers

The samples described within this thesis are mainly processed in a multi-purpose high vacuum chamber[1] by various means of physical vapor deposition (see Fig.: 3.1). The main apparatus is an electron beam evaporation stage, containing a rotatable, water-cooled mounting for 4 material crucibles. The emission of electrons from a tungsten filament is accelerated by 8 kV high voltage and directed onto the material by magnetic force. The tightly focussed beam generates a large amount of heat at its point of impact even at moderate emission currents (several 10 mA) due to the absorption of the kinetic energy of the electrons. Thus it is possible to reach the evaporation temperatures of nearly any solid material, which is useful for non-conducting oxides.

To modify the ablation of material, the beam can be deflected by additional fields to scan the complete area of the crucible[2]. This can be done manually by setting the point of impact, semi-automatically with frequency and amplitude modulation in x- and y-direction respectively, or fully automatic with predefined patterns. By this, materials which form a molten bath are heated more homogeneously, whereas the formation of deep trenches in fine-grain substances is reduced. The combination of deflection

---

[1] Lab 500, Leybold Optics
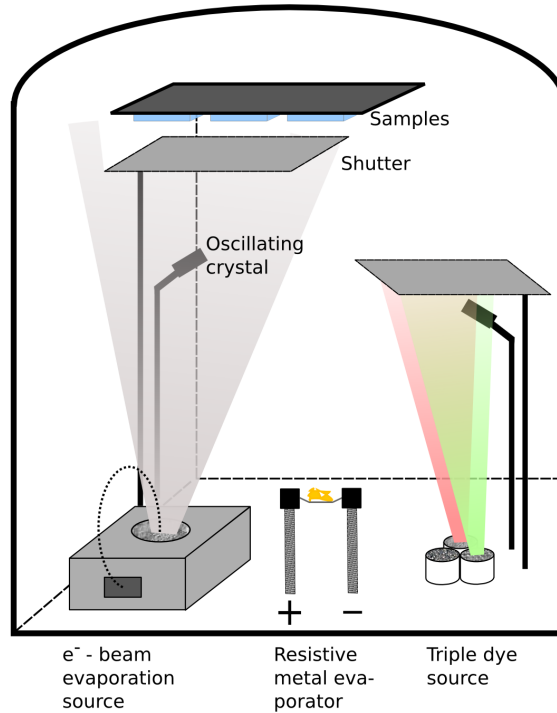[2] ESV14, Leybold Optics

Figure 3.1: Schematic of the high vacuum chamber, indicating the crucial parts for the preparation of the samples.

settings and emission current finally defines the deposition rate of the material at a given pressure. If not marked differently, the layer growth is kept at $2\mathring{A}/s$, providing a good trade-off between film quality and preparation time [36].

The thickness and rate monitoring is done via 6 MHz water-cooled oscillating crystals[3]. By taking into account geometric factors, material density, and adhesion, the controller estimates the layer growth with good accuracy from the shift of their eigen frequency. The drawback of this method is that the measurement is done at a different place than the sample location. This can induce measurement errors, when fluctuations of the material vapour or the evaporation lobe take place. In case of single films, one can neglect these effects, but for dielectric mirrors, which consist of many identical layers, it can reduce their quality. A way to overcome this problem is to observe the material deposition by optical means, e.g. in situ reflection or transmission , with the positive side effect of an additional monitoring of the optical constants, which may partially change with evaporation parameters [37].

During each deposition of oxide materials, the base pressure of 10^{-6} mbar is raised specifically to a partial pressure of $2 \cdot 10^{-4}$ mbar of pure oxygen[4]. This is necessary to prevent a decomposition of the dioxides to highly absorptive monoxide, as it happens e.g. in the case of titanium dioxide [38, 39].

---

[3]Leybold Inficon Inc. with control units XTC/2, XTM/2
[4]Air Liquide UN 1072 oxygen N48

Although the electron beam is suitable for nearly any inorganic material, it cannot be used for the deposition of organic molecules, since their bonds are too fragile. They are evaporated from ceramic crucibles, of which the temperature is controlled via heating wires and cooling water. A thermo-sensor in the bottom controls the heating current, defined by the settings of the controller[5].

A third type of deposition technique is applied for metal layers. A tungsten wire is fitted into a high current feedthrough and pieces or a wire of the metal is wrapped around it. The application of several 10 A melts the metal and often leads to the formation of a molten sphere, which has an ideal evaporation geometry. Instead of the tungsten wire, one can also use a tantalum boat, which is useful for grainy materials.

3.1.2 The dielectric mirror materials TiO_2 and SiO_2

As described in section 2.2.1, the material choice drastically influences the properties of the mirror and thus the resonator. For this reason, all microcavity samples within this thesis consist of $\lambda/4$ layers of titanium dioxide and silicon dioxide. Among all transparent materials in the visible spectral region (between 400 and 800 nm), they provide one of the largest gaps between their respective refractive indices (see Fig. 3.2(a)) of $\Delta n \approx 0.6$. This results in high reflection coefficients at a moderate number of necessary layers. If not stated differently, the standard mirror consists of 10.5 alternating pairs of the two oxides, starting with TiO_2. The reflection typically overcomes 99.9% at the design wavelength, and is higher than 99% within a $\approx$ 150 nm region of the stopband (see Fig. 3.2(b)).
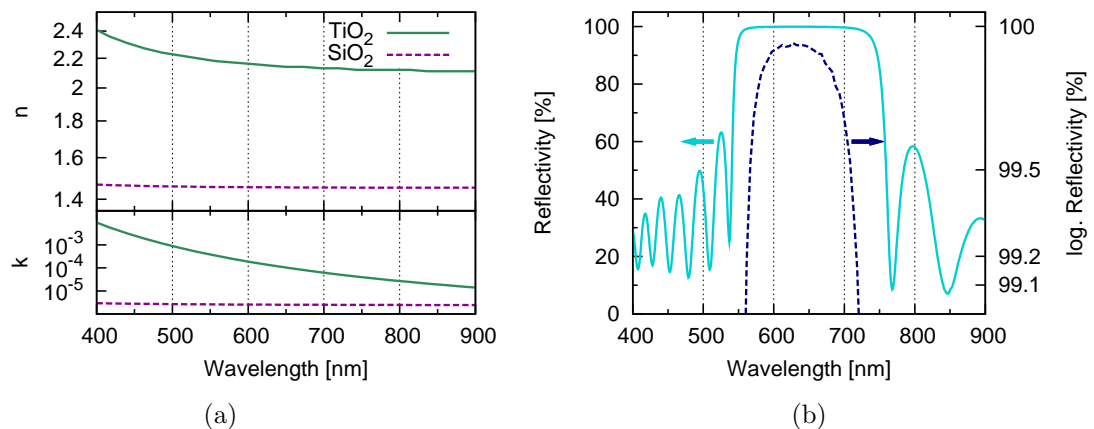

Figure 3.2: (a) Optical constants of SiO_2 and TiO_2. (b) Reflectivity spectrum of a 21 layer mirror of the two materials.

The films are grown from a molten bath of TiO_2-tablets and fine grains (2 - 5 mm)

---

[5]Triple evaporation source 3xDE-FR/2.1, CreaPhys

of SiO_2 [6]. The different melting behaviour of the two materials influences the angular distribution of the deposited material. Whereas the particle flow from the TiO_2-source can be regarded as Lambertian, the grains of SiO_2 melt separately, resembling a directed beam through the partial scattering at surrounding media. This effect becomes even worse with increasing layer number due to the formation of trenches within the grains and must be compensated with an alternating deflection pattern of the electron beam.

Due to the evaporation conditions, both materials show a columnar growth instead of a continuous accumulation [37]. The column diameter is too small to show any optical scattering effects, but they introduce a measurable anisotropy, which becomes stronger for higher deposition angles. Ultimately, the overall roughness cannot be decreased below a certain level, which is crucial for metal contacts to avoid shorts. A way to overcome the latter, is to deposit the upmost layer with a different technique, e.g. sputtering or plasma ion-assisted evaporation [40, 41].

3.1.3 Conductive layers

For any kind of electrical transport into the investigated structures, a conducting layer is needed. Within the framework of this thesis thin metal layers are prepared for this purpose. The weakness of metals is their absorptive behaviour, since the large number of roundtrips in a resonator accumulates even smallest losses. In theory, the losses can be compensated when the layers are placed exactly at the nodes of the amplitude of the electric field of the resonator. Practically, it is nearly impossible to achieve the needed precission of layer growth within the given setup. A set of test samples showed no significant difference in absorption between the case of several thin ($\approx 10\,nm$) layers of metal, sandwiched between mirror layers and the same thickness of a single layer on top of the mirror. Here again, the thickness control by optical means can help to prepare such type of samples. A way to have metal contacts without losses perpendicular to the mirror layers, is to build lateral structures in the active region. Thus, it is possible to use low-resisitive, thick layers which can inject charge carriers into the organics of the cavity layer. Furthermore, one can construct optically active patterns, since the refractive indices of metals differ strongly from those of the organic materials.

For the growth of metal layers, the deposition via tungsten wire/boat leads to a more homogenous coverage in comparison to the electron beam deposition. To achieve a thin closed surface, it is necessary to work with either very low or rather high deposition rates. In the first case, the particle mobility on the sample surface is too low to show a pronounced aggregation, wheras in the latter case, the fast growth of the film leads to a fixation of the first layers by the following particles. Within this thesis, high deposition rates (0.5-1 nm/s) are applied for the preparation of metal layers. In some cases, a 1-

---

[6]TiO_2 (level of purity: 99,9%), SiO_2 (level of purity: 99,997%), Prof. Feierabend GmbH
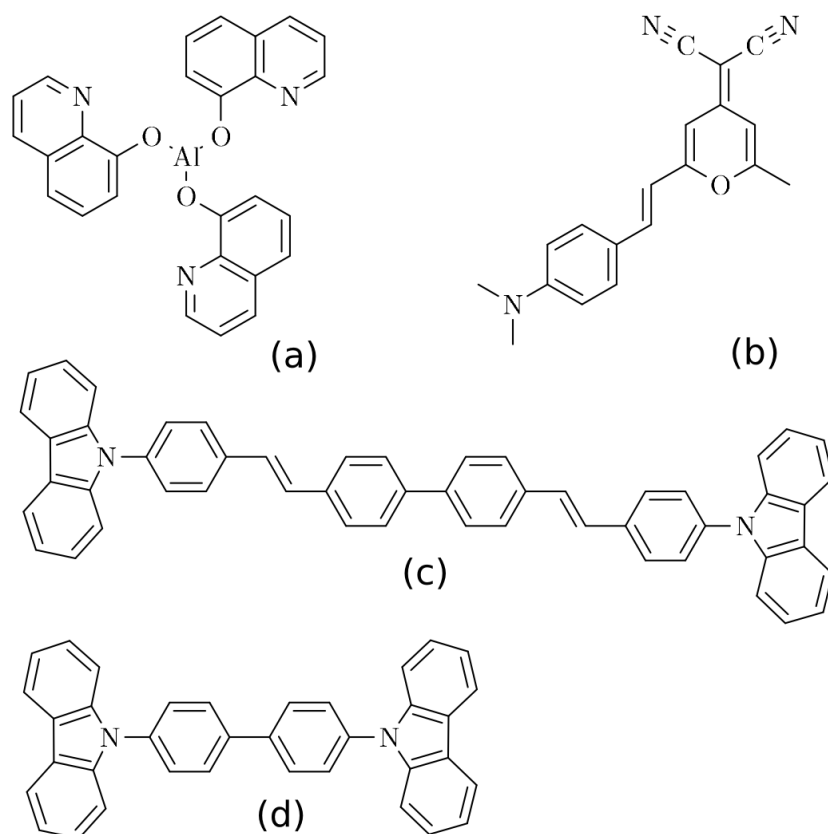
Figure 3.3: Chemical structures of (a) tris-(8-hydroxyquinoline)aluminum - Alq$_3$, (b) 4-(dicyanomethylene)-2-methyl-6-(4-(dimethylamino)styryl)-4H-pyran - DCM, (c) 4,4'-bis[(*N*-carbazole)styryl]biphenyl - BSB-Cz, (d) 4,4'-di(*N*-carbazolyl)biphenyl - CBP.

2 nm layer of Cr is further introduced as adhesive layer, which helps to achieve closed layers at reduced overall thickness.

3.1.4   The organic semiconductor systems Alq$_3$:DCM and CBP:BSB-Cz

For the active cavity layer, numerous organic dyes can be applied, as long as they can sustain the temperatures of the second mirror deposition (up to 150°C). Furthermore, for optical excitation, the absorption band should not be below ≈370 nm, since the losses in the TiO$_2$-layers increase drastically in this wavelength region. The majority of the investigated samples within this thesis contain a well-known host-guest system of the two dyes tris-(8-hydroxyquinoline)aluminum short Alq$_3$, and 4-(dicyanomethylene)-2-methyl-6-(4-(dimethylamino)styryl)-4H-pyran or DCM. Typically, a ratio of 1:50 of DCM-molecules in Alq$_3$-matrix is set, which is a highly efficient 4-level laser system [42, 43]. Both materials are commercially available [7] and are sublimated twice before the deposition. The mixed layer is prepared by co-evaporation, with a rate of 10 $\mathring{A}$/s for

---

[7]DCM - Radiant Dyes Laser & Accessories GmbH, Alq$_3$ - Sensient Imaging Technologies GmbH

Alq$_3$ and 0.2 Å/s for DCM. A feature of this system is its highly efficient nonradiative energy transfer (Förster-Transfer [44]), resulting from the large overlap of the matrix and dopand spectrum (Fig.: 3.4(a)). Alq$_3$ has a residual excitation shoulder at 390 nm, and emits at 520 nm, whereas the dissolved DCM molecules absorb at 490 nm, to emit at $\approx$ 630 nm. This opens the opportunity, to pump the system in two different regimes, either using the energy transfer and pump the Alq$_3$ matrix, or directly excite the DCM molecules. Depending on the specific measurement setup, both excitation types are applied.
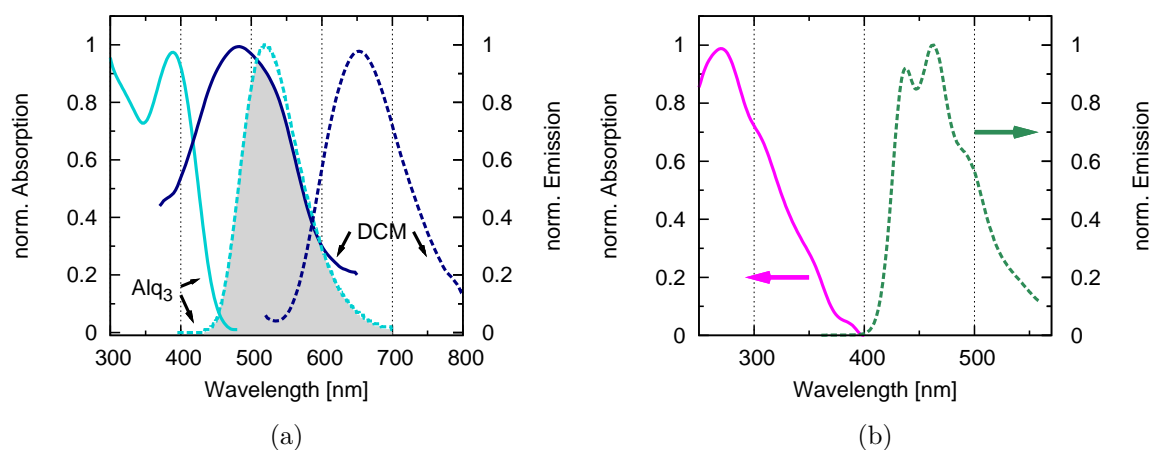

Figure 3.4: (a) Normalized absorption (straight line) and emission (broken line) spectra of Alq$_3$ and DCM. Indicated is the overlap of the two spectra, where the Förster-Transfer can take place. (b) Normalized absorption and emission spectrum of the compound BSB-Cz in CBP matrix.

Another efficient emitter is 4,4'-bis[(*N*-carbazole)styryl]biphenyl (BSB-Cz) [45–47], which has shown a large radiative decay rate, and a photoluminescence quantum efficiency of 100%, when dissolved (6wt %) in a matrix of 4,4'-di(*N*-carbazolyl)biphenyl (CBP) [45]. The compound has interesting properties, such as a low threshold for amplified spontaneous emission (ASE), as well as a strong anisotropy of its refractive index. The dopand is synthesized by the group of Prof. Adachi [8], and is co-evaporated with CBP at the same ratio but half the rate of the Alq$_3$:DCM deposition. Besides an unstable deposition rate of the BSB-Cz, crystallization occured for the compound (see Fig.: 3.5(a)), which spoils the upper mirror. Since the crystallization tendency of CBP is known, it can help to use equivalent matrix materials, e.g. spiro-CBP. Nevertheless, it is possible to fabricate microcavity samples with the dye system, but stimulated emission could not be achieved, which is partially accounted for the excitation conditions needed (see Fig.: 3.4(b)). Currently, it is possible to observe microcavity lasing in experiments incorporating the spiro-compound.

---

[8]Center for Future Chemistry, Kyushu University, Fukuoka (Japan)

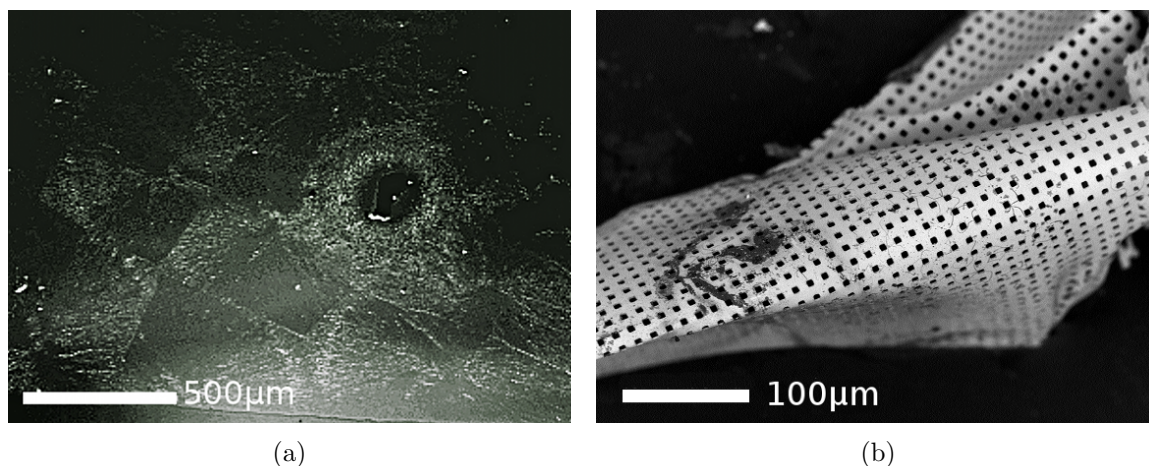(a)   (b)

Figure 3.5: (a) Crystalline structure of the CBP:BSB-Cz layer, observed with an optical microscope in dark field mode. (b) Raster electron microscope (REM) image of some debris of the applied shadow mask.

3.2 Advanced processing steps

3.2.1 Shadow mask structuring of the cavity layer

The aspect of this work is the influence of lateral structures in the cavity layer. To obtain geometric deviations from a plane surface, the technique of shadow mask deposition through small openings of a mask is applied. This method can be used universally for any kind of evaporated material, but is limited regarding possible patterns, very small sizes, and sharpness of the grown structure. Lithographic patterning would be more precise, but experiments with focussed ion beam etching showed, that it is nearly impossible to apply it to layers of organic material without severe damage and thus optical inactivation.

The shadow masks applied within this work are alienated calibration grids for electron microscopy [9]. They allow a parallel deposition of several 100,000 square posts with a size of $5 \times 5 \, \mu m^2$ and a periodicity of $12 \, \mu m$ in x- and y-direction (see Fig.: 3.5(b)). Additionally, transmission electron microscopy carrier nets with openings down to $1 \, \mu m$ are probed, which result in functional but inefficient structures.

3.2.2 Diminishing and initiating continuous inhomogeneities

The beam characteristics of any evaporation source define the homogeneity over the full area of a single sample or a set of samples. Although a maximum possible distance ($>40 \, cm$) is kept each time, the angular deviation is strong enough to create thickness gradients on the samples. Typically, the difference is on the order of 2-3 % over a

---

[9]Plano GmbH, 2000 mesh nickel foil, $25 \times 25 \, mm^2$

2.5 cm sample. The consequence is that for multiple processing steps, the position and direction of the sample needs to be considered. A straightforward way is to move the sample during the deposition in such way, that each part obtains the same amount of material. Industrially prepared filters use for this purpose a planetary gear type mounting. The method applied here for mirror layers is to mount a sample via a flange on a motor and rotate it at moderate speed around its center. Alternatively, a set of substrates can be mounted around the axis of the motor to obtain several identical samples. In each case, the gradient is reduced, which is even visible with bare eye. On the contrary, a pronounced gradient can provide the possibility to change the sample parameters smoothly over a certain range. For this purpose, several shutters are prepared, which can be mounted on a motor. Their profile is chosen such that, depending on the distance towards the rotation axis, the covering time during one convolution varies (see Fig.: 3.6 (a)). The achieved variation is always a relative one and does not depend on the orbital speed. One can create wedges covering several 100 nm in height, but always at the the expense of a stronger variation of the sample properties within the measurement spot.
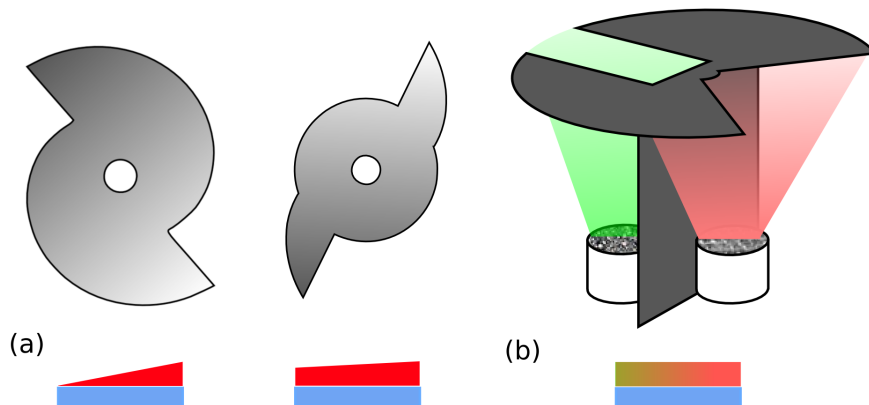

Figure 3.6: Shutter designs for gradient deposition and resulting layer growth: (a) 100 % and 25 % height variation disks, (b) setup for concentration gradients.

A way to smoothly vary the dopand concentration along a direction of a sample can be applied for any co-evaporation process. The two sources are separated and adjusted for a respective rate, and the sample is again mounted on a motor and rotates into the beam of each source. Now, sheets are introduced close to the sample to partially cover the beam of a source, which controls the deposition time on each part of the sample and hence the amount of material (see Fig.: 3.6 (b)). If the arrangement of the sheet forms a segment, the ablation should be homogenous, whereas a different opening leads to a gradient of material. For this technique, it is crucial to use a high speed of the motor to achieve a mixing similar to the standard co-evaporation process, instead of a layer by layer growth. Furthermore, it is necessary to design the openings of the sheets for matrix and dopand interdependently, to avoid a thickness gradient, which arises

when only one of the materials growths inhomogenous.

3.3   Sample characterization techniques

3.3.1   Basic determination of optical properties

For the standard determination of transmission, reflection, and absorption of planar samples, commercial spectral photometers [10] are applied. They use up to two high power light sources guided through a monochromator, and then split into two beams, the reference and sample part. Except for absorption measurements, the reference compartment is usually kept empty. For the simulation of the layers, this implies the use of a substrate layer to account for the partial reflections. The width of the beam can be adjusted via slits, to enable either precise position dependent measurements at the cost of stronger noise or an averaging over a wider area which blurs distinct features. Since the spectrometers use a monochromator only for the incoupling of light, possible luminescence needs to be taken into account for any analyzed sample. Especially the measurement of organic dye layers can be significantly modified by photons originating from the molecules itself. In this case, filters are installed behind the sample (e.g. dielectric edge filters). The determination of the relative absorption and emission spectra of investigated materials is done with fluorescence spectrometers[11]. Again, the light of a Xe-lamp is guided through a monochromator and a slit to select the excitation wavelength (Czerny-Turner-configuration). The sample or cuvette is mounted under an angle towards the incoming beam, to avoid direct light propagation towards the detector. The emitted photons are coupled into a second identical monochromator and are detected. Since the sensitivity of the instrument needs to be very high, scattered excitation light can enter the signal path and introduces strong peaks at multiples of its wavelength. To avoid this, it is necessary, to use filters, blocking the excitation wavelength and to carefully select the scanning region of the corresponding spectrum.

3.3.2   The microphotoluminescence setup

Since the above described methods are not suitable for samples structured on the wavelength scale, it is necessary to use a different device. For this purpose, a microphotoluminescence setup is applied, basically consisting of a set of highly magnifying objectives and lenses, coupled to a monochromator and a charge coupled device (CCD) matrix detector. In detail, the light of either a halogen lamp, a pulsed green (532 nm, 1.5 ns,

---

[10]Shimadzu UV - 2101 / 3101 PC, Perkin Elmer Lambda 900
[11]Fluoromax from SPEX, Edinburgh Instruments FS 920

2 kHz) solid state laser[12], or a deep blue diode laser [13] (407 nm, cw) is used on the incoupling side. To attenuate the power, a neutral density filter wheel is applied, covering a range of 3 orders of magnitude. A following microscope objective projects a light spot of $\approx$2-3 μm diameter onto the sample, which is installed on a 3-axis micrometer stage. A subsequent objective with high magnification (63 times) and aperture (NA = 0.8) collects the signal and forwards it to another lens. The interplay of position and focal length of the objective and lens allows two different types of measurement, an imaging configuration (so termed near field) and an angle resolved one (far field). In case of the latter, the focal plane is located at the entrance of the monochromator, which can be confined with a cross-slit, whereas an magnified image of the analyzed area can be seen for the near field alignment. Via a 0.5 m monochromator[14], the spectrum is dispersed onto the 256×1024 pixel array[15], which is Peltier-cooled down to $\approx$-30 °C, to decrease its noise. The 256 rows enable the simultaneous detection of multiple aligned spectra, which form either the spatial coordinate (near field) or detection angle (far field) but can also be integrated for homogoneous samples with low signals. For the alignment of the sample position and the focus of the microscope objectives, it is possible to direct the signal after the cross-slit via a flipping mirror onto a camera system, providing a magnified image of the investigated area. If a laser is applied for a measurement, it is necessary to install filters into the signal path (color-filter, notch filter), to avoid oversaturation or even damaging of the sensitive detector, but this may alter the absolute value of the detected signal.
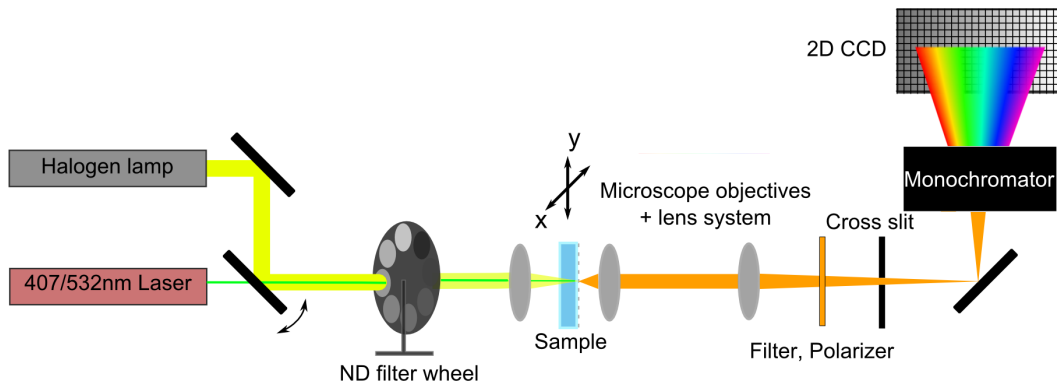

Figure 3.7: Schematic layout of the microphotoluminescence setup.

---

[12]CryLas FDSS-532-Q2
[13]Coherent Vioflame, 4 mW cw
[14]Jobin-Yvon 500M
[15]Princeton Instruments TE/CCD-1024EM/UV

3.3.3 Measurement of lasing characteristics

To measure the samples in the stimulated emission regime, either the microphotolumi-nescence setup or a multi stage fs-setup from Coherent is used. Since all measurements are performed under ambient conditions without protective athmosphere, it is necessary to pump the dyes in a pulsed regime. For this reason, the blue diode laser is used in the μ-PL setup just for luminescence experiments at low power, and the green one to measure stimulated emission from the structures. The neutral density filter wheel and additional grey filters are employed to vary the intensity of the pumping as well as the emitted beam. For different wavelengths than 532 nm, the use of the ultra short pulse system is advisable. The detection side is basically the same as for the μ-PL setup, with the advantage of multiple gratings in the monochromator, to allow different resolutions. The incoming beam is focussed via a parabolic mirror onto the sample, which is necessary to keep the ultrashort pulse in shape. The disadvantage is a wider excitation focus of $\approx 50 \, \mu m$ diameter, of which the detected area can partially be selected with the cross slit at the entrance of the monochromator. For the generation of the pump beam, a complex laser system was used, which is now replaced by a new one. In the original complex system, a home-built Ti:Sapphire - Laser was pumped by a frequency-doubled Nd:YVO$_4$ - Laser (Millenia V - Spectra Physics). The pulses were subsequently amplified several orders of magnitude (from 1 nJ to 0.7 mJ) in a regenerative Ti:Sapphire - amplifier (Spitfire - Spectra Physics). To invert the Ti:Sapphire - system, a frequency-doubled Nd:YLF - Laser (Merlin - Spectra Physics) is used. The pulses of the amplifier system (800 nm, 200fs, 1kHz) were frequency-doubled in a β - barium borate - crystal (BBO) to obtain the desired wavelength of 400 nm [48, 49]). A better flexibility regarding possible wavelengths and simplier operation is obtained with the new setup. Here again, a Ti:Sapphire - Laser (Micra-5 - Coherent) pumps a regenerative Ti:Sapphire-amplifier (Elite Legend Duo - Coherent). The pulse energy is increased from 4 nJ to 1.2 mJ at a reduction of the repetition rate from 80 MHz to 5 kHz. This beam can again be converted to 400 nm with the BBO-crystal, or it is directed into an optical parametric amplifier (OPerA Solo - Coherent). This device can modulate the wavelength of the beam via nonlinear optical processes to an output between 400 and 2600 nm.
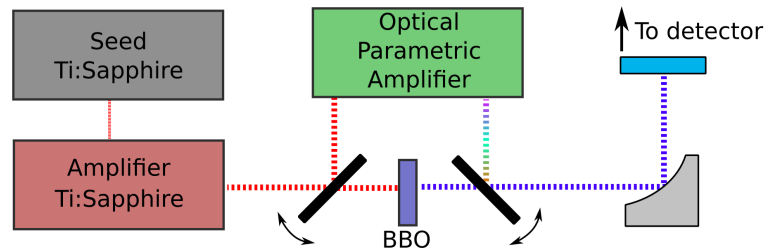

Figure 3.8: Layout of the ultrashort pulse beam generation setup.

4 Resonant mode properties of dielectric mirror resonators

The following sections give an insight into the properties of the resonant modes of microcavities. At the beginning, a wedge is utilized to study a remarkable polarization splitting in detuned resonator systems. Then, the spectral features of photonic boxes with lateral extensions on the micron scale are presented and explained. A polarization dependence for the resonant modes is also apparent, which is treated differently.

4.1 Planar systems

4.1.1 Polarization splitting in wedged microcavities

In a double DBR resonator, ideally one matches the cavity layer thickness and thus the modal wavelength λ_m to the design wavelength of the mirrors λ_d. If no material anisotropies are present, light of both polarizations shows the same dispersion, with the only difference of a linewidth sharpening for TE and broadening for TM modes at larger angles (see figure 2.6). Variations due to a different penetration depth of light into the innermost mirror layers can mostly be neglected. When λ_m is now shifted away from the center of the stop band, either intentionally or by fluctuations in the preparation process, the curvature of the dispersion at large angles strongly depends on the polarization. Thus, even a $\lambda/2$-cavity gets two resonant wavelengths at a close spectral distance. This effect was observed in many experiments [50–55] and described by Panzarini et al. in [28]. They derived an approximate expression to calculate the spectral distance Δ between the two cross polarized modes ω_m^{TM} and ω_m^{TE} for the external observation angle θ:

$$\Delta(\theta) = \omega_{\mathrm{m}}^{TM}(\theta) - \omega_{\mathrm{m}}^{TE}(\theta) \simeq \frac{L_{\mathrm{c}} \left(L_{\mathrm{DBR}}^{TM}(\theta) - L_{\mathrm{DBR}}^{TE}(\theta) \right) \left(\omega_{\mathrm{d}}(0) - \omega_{\mathrm{c}}(0) \right)}{\left(L_{\mathrm{c}} + L_{\mathrm{DBR}}(0) \right)^2 \cos\theta_{\mathrm{eff}}}. \tag{4.1}$$
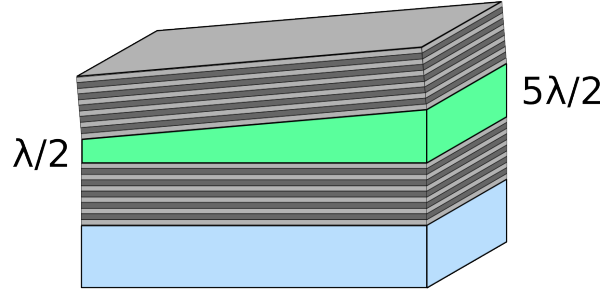
Figure 4.1: Schematic of the investigated wedged microcavity.

The lengths L_j^i are the cavity thickness and DBR penetration depths at the corresponding polarization, ω_d defines the center of the stop band and ω_c is the frequency of the cavity mode under normal incidence and neglect of the penetration depth L_{DBR}. The angle θ_{eff} is regarded as common angle within the cavity, when the refractive indices of the involved materials are close to each other.

To study the influence of the cavity mode position within the stop band at normal incidence ($\omega_c(0)$) on the spectral distance between TE and TM polarization at a fixed oblique angle, a cavity with wedge shaped cavity layer (Fig. 4.1) is employed. Thus, it is possible to study different detunings for one and the same sample in a wide wavelength range by varying the spatial position and such the investigation region along the sample, which is supported by the broad photoluminescence spectrum. The incorporated organic medium in this sample is CBP:BSB-Cz (2 wt %), deposited with a shutter to obtain the wedge. For the dielectric mirrors, the standard symmetric design of 21 alternating $\lambda/4$-layers of TiO_2 and SiO_2 is used. The stop band is centered around 420 nm close to the first emission maximum of the dye system (see Fig. 3.4(b)).

For the excitation, the blue diode laser (cw, 407 nm, 4 mW) is used, although the excitation wavelength is already at the edge of the absorption band. The pumping power is decreased with neutral density filters to reduce thermal degradation of the material. The beam is focused in the cavity layer to a spot size of about $3\,\mu$m in diameter. Because of the wedge shaped cavity layer, the spot leads to a total variation of the spectral cavity mode position of about 0.12 nm, which alters the spectral halfwidth of the mode, but can be neglected in the following. The splitting is analyzed in the confocal microscope setup in far field geometry. With the help of the micrometer stage, the measurement position is changed alongside the wedge of the cavity, which tunes the cavity mode position within the stop band provided by the DBRs.

Figure 4.2 shows the angular resolved PL spectra (upper panels) at four different positions on the sample, with the respective polarization of the resonator mode indicated. The typical parabolic shape of the microcavity dispersion is visible, both for the resonance and the stop band. Adjacent on the low energy side are the well-marked side band lines, where residual emission of the dye system can escape the mirrors, which
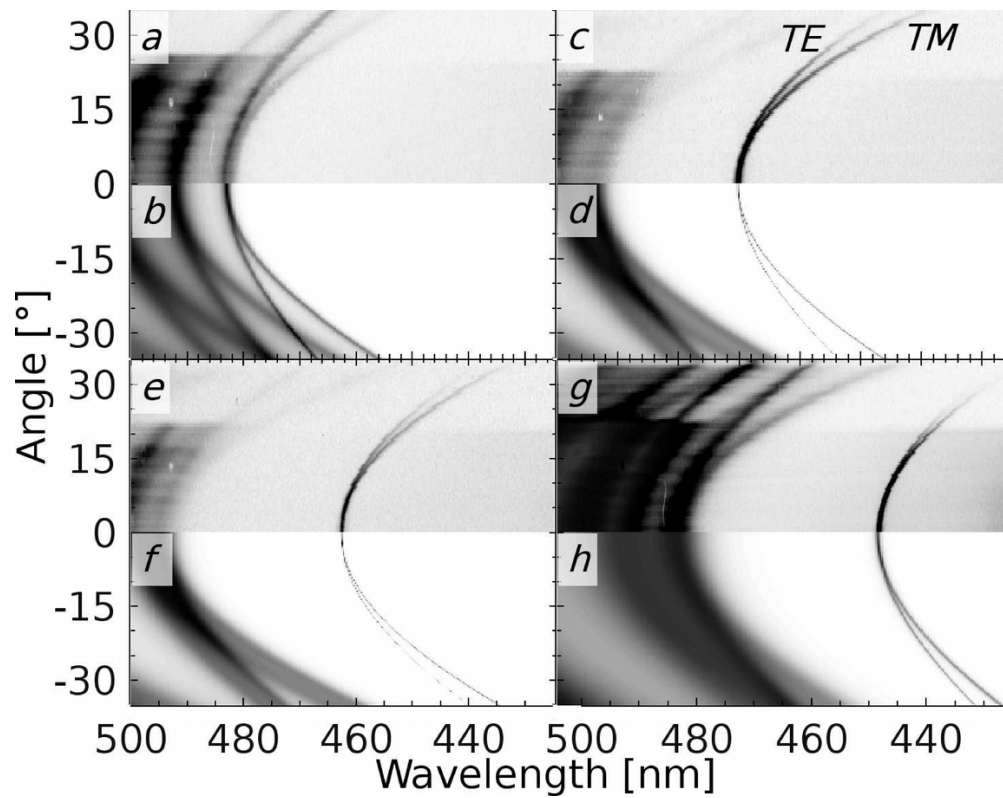
Figure 4.2: Emission spectra of the cavity for 4 different mode detunings. For each measurement (a, c, e, g), a transfer matrix calculation is performed (b, d, f, h). The data was acquired by former diploma student F. Becker under my supervision.

are highly transmissive in this spectral region. Following the series from a/b to g/h, the resonator thickness decreases and thus the position of the cavity mode shifts to shorter wavelengths. The increasing spectral distance of the two cross-polarized modes for larger observation angle is clearly visible. From the comparison of the splitting, one can see the trend to larger values for a thicker cavity layer or longer resonance wavelength. As a direct consequence of the reduced reflectivity of the DBR mirrors apart from their design wavelength, the spectral width (FWHM) of the cavity mode increases [28, 52], when it reaches the stop band edge.

The measurements are compared with corresponding transfer matrix calculations (Fig. 4.2, lower panels). Due to the broad emission spectrum, it is sufficient to calculate the TE-, TM- and randomly polarized transmission spectra. The direct comparison of the simulation and measurement panels shows a good agreement of the stop band position and resonant mode behaviour.
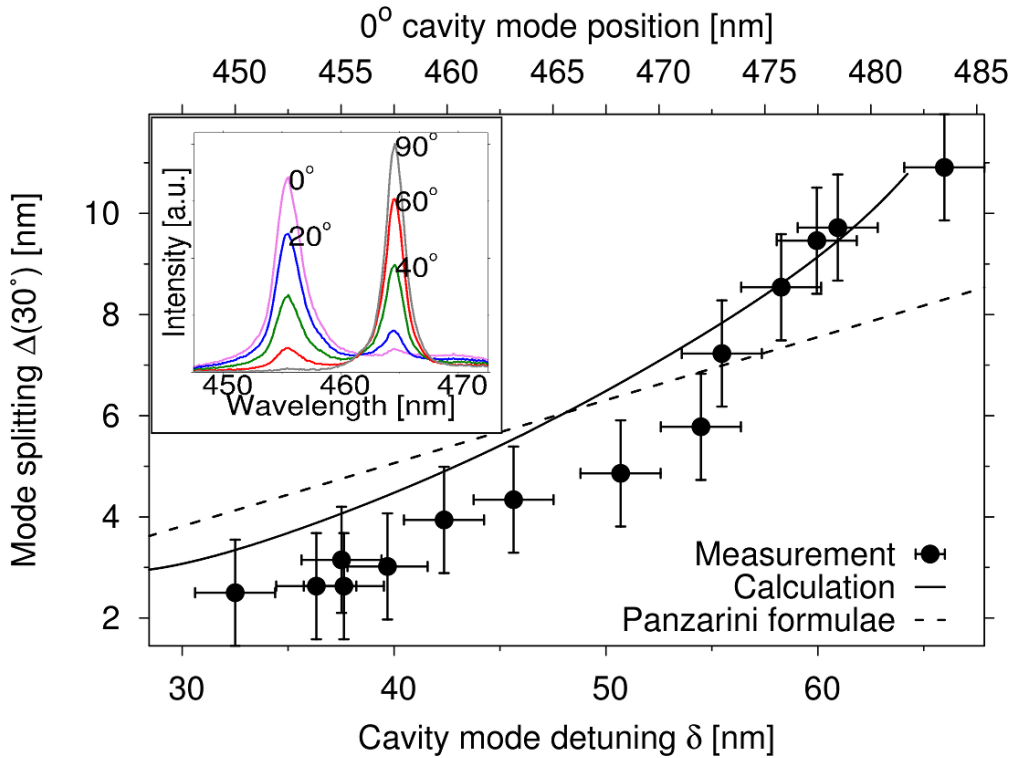
Figure 4.3: Dependence of the polarization splitting $\Delta(30°)$ on the cavity mode position and the detuning δ. Symbols: Measurement. Solid line: Corresponding transfer matrix calculations. Dashed line: Calculation according to equation (4.1). Inset: Polarization resolved measurement of the cross-polarized cavity-modes (482 nm at 0°) for an emission angle of 30°. Indicated are the relative polarizer settings.

To resolve the dependence of the spectral splitting distance on the respective detuning, a polarizer is inserted in the signal path and the cavity mode positions at normal and 30° observation angle are recorded. For a series of polarizer settings, the lines

of oblique emission are shown in the inset of Fig. 4.3, exemplarily for a cavity mode position of 482 nm. This plot clearly shows that the splitted cavity modes are well and orthogonally polarized. The shorter wavelength peak corresponds to TM polarization, which is the case when the wavelength of the resonant mode is larger than the wavelength of the stop band center (see equation (4.1)). Vice versa, the TE mode would be emitted at shorter wavelengths than the TM mode, if the resonant mode moves to the short wavelength side of the stop band. The spectral width of the TM mode at ~ 456 nm is slightly broader compared to the TE one at ~ 464 nm. This is surprising, since the spectral position closer to the mirror design wavelength should support a higher reflectivity and thus smaller linewidth. However, a look at figure 2.4(b) can explain this effect as a result of the increasing reflectivity of TE polarization with incident angle, whereas the reflection of TM light drops. The Q factor of the depicted modes can be estimated from the spectral FWHM, and is with ≈ 200 below typical values for the involved preparation method (several 1000 [56]), which may be attributed to the problematic growth of the dye compound and the wedge-induced height variation in the investigation area.

The dependence of the polarization splitting on the detuning of the cavity can be seen in figure 4.3, where the distance $\Delta(30°)$ between the splitted resonant states is plotted for a series of measurement positions on the sample (symbols). The detuning δ of the cavity mode at normal emission with respect to the center of the DBR stop band is set as the abscissa. Clearly, a parabolic trend towards larger values (>10 nm or 2%) is visible when reaching the stop band edge. To fit this behaviour with equation (4.1), one can reduce it due to the constant observation angle to the following expression:

$$\Delta(L_c) \simeq const.\frac{L_c\omega_d(0) - \frac{c}{2n_c}}{(L_c + L_{DBR}(0))^2}. \tag{4.2}$$

The result is plotted as dashed line. The values for smaller detunings are comparable with the measurements, but diverge with higher δ, as the calculated dependence $\delta(\Delta)$ is practically linear and depends mostly on the difference $\omega_d - \omega_c$. The deviation is due to the fact that equation (4.1) is a linear approximation, which is only valid within a small range around the stop band center.

A better agreement is possible by using the results of transfer matrix calculation (solid line). For the calculation, $n_{TiO_2} = 2.19$ and $n_{SiO_2} = 1.46$ are set as optical constants for the mirror layers and $n_{CBP} = 1.75$ for the organic cavity layer. The parabola thus obtained follows the trend of the measurement and confirms the large splitting values for highly detuned microcavities. Of further experimental interest might be a coupling between the two crosspolarized states, as this could result in generation of frequencies in the THz region.

4.2 Photonic boxes

4.2.1 Spatial and angular mode profile

Many results in this work are related to microcavities, where the active region is laterally restricted to a small volume. These so-called photonic boxes have been investigated in the field of inorganic-type semiconductors [57–62] for some time. Due to the lower stability of organics, it is more complicated to fabricate such structures with standard etching techniques. Nevertheless, in 2006, Adawi *et al.* [22], proved that it is possible to confine light in an organic system with extensions on the wavelength scale in a focussed ion-beam etched film.

In the following, results of non-destructively prepared, laterally confined microstructures are presented. By the use of shadow mask structuring for the organic layer, the simultaneous preparation of a huge amount of photonic boxes provides a nearly unlimited number of measurement positions on a single sample. From all probed sizes and geometries, the $5 \times 5 \, \mu m^2$ square shaped structures have proven to be the best choice. Although every photonic box should have the same properties, some features vary within the full sample size. Due to the hanging position of the thin mask foil, it is not always possible to have the smallest distance achievable between it and the sample surface. This leads to variations in size (mostly smaller) and form (from cornered to round) and thus often to a weaker signal, which can be seen in the monitoring system. To reduce the hanging effect, a permanent magnet is applied to pull the foil towards the sample.

To understand the response of these highly confined systems at high pumping powers (lasing regime), it is useful to investigate the transmission and spontaneous emission properties. The measurement results are taken from various samples, with a common box size and height close to half of the design wavelength of the mirrors. The organic dye is deposited directly through the openings of the shadow mask onto the bottom mirror made of TiO_2 and SiO_2 alternating pairs. Subsequently, the second mirror is evaporated on top and encloses the active region. To map the transmission and fluorescence signal, the μ-photoluminescence setup is used in near and far field regime. One has to mention that the setup allows to measure only a cross section of the sample area, since the 2D CCD matrix uses the second coordinate for the spectral analysis. A real 2D mapping of the structure would require a spectral selection of the image before it is projected onto a CCD.

The boxes are either excited with the blue (407 nm) cw-laser, or a halogen lamp screens the transmission. Figure 4.4 shows the spatially resolved transmission of the cross section of 4 equally spaced boxes with a periodicity of $12 \, \mu m$. The positions of the confining structures can be clearly discerned by the modes, distributed within the
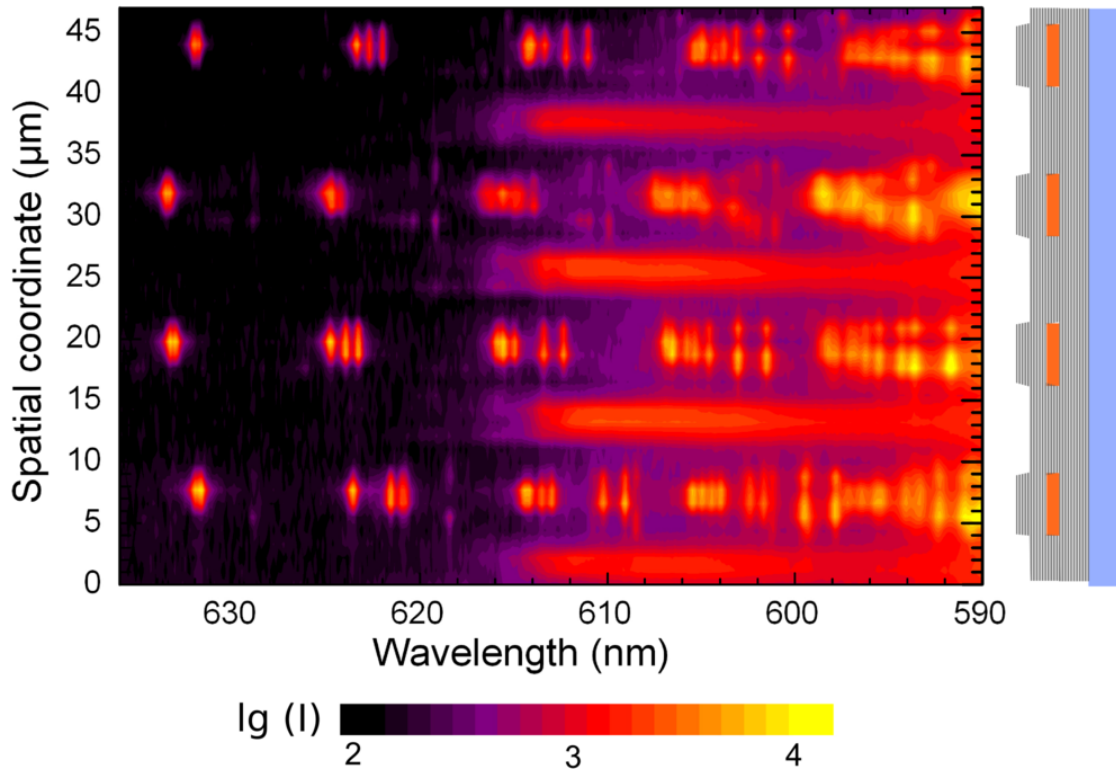
Figure 4.4: (a) Imaging spectrum in near field configuration, presenting the transmission of a cross section of 4 photonic boxes. The position and approximate size is indicated in the sketch on the right. One can clearly recognize the discrete modes of the 3D confined structures with a varying amount of antinodes in space. In between the boxes, the top mirror is directly attached to the bottom mirror creating an empty cavity with slightly different transmission properties. The bright region below 615 nm indicates already the edge of the stop band, where light is partially transmitted. The different position of the discrete states can be attributed to small height variations, which typically occur between different regions on the sample and not at a given position, as seen here.

spectrum. As expected from the considerations of the density of states, the free spectral range decreases with higher mode numbers and thus shorter wavelengths. Some modes appear at a very weak intensity, which can be explained by the measurement condition. As the cross slit before the monochromator selects a stripe of the sample surface, the signal is low, when the intensity profile of the specific mode has its antinodes around this region.

The good confinement of the structure can be dedicated from the fact that the detected signal is mainly concentrated in the center of the box. The surrounding consists of a microcavity, formed of the two mirrors facing each other with a $\lambda/4$-wave thickness of TiO_2. This would, in principle support a mode and thus resonant cavity states which can interfere with the discrete states of the box. Nevertheless, a leakage of light out of the boxes happens in practically all samples only away from the stop band center, close to the higher transmissive edges. A further way to avoid a possible leakage is to use $\lambda/8$-wave thick terminating and starting layers for the bottom and top mirror, respectively. By this, the overall reflectivity is only weakly affected, whereas the surrounding now forms a simple DBR of twice the single number of layers, which cannot support any resonant state in its center.
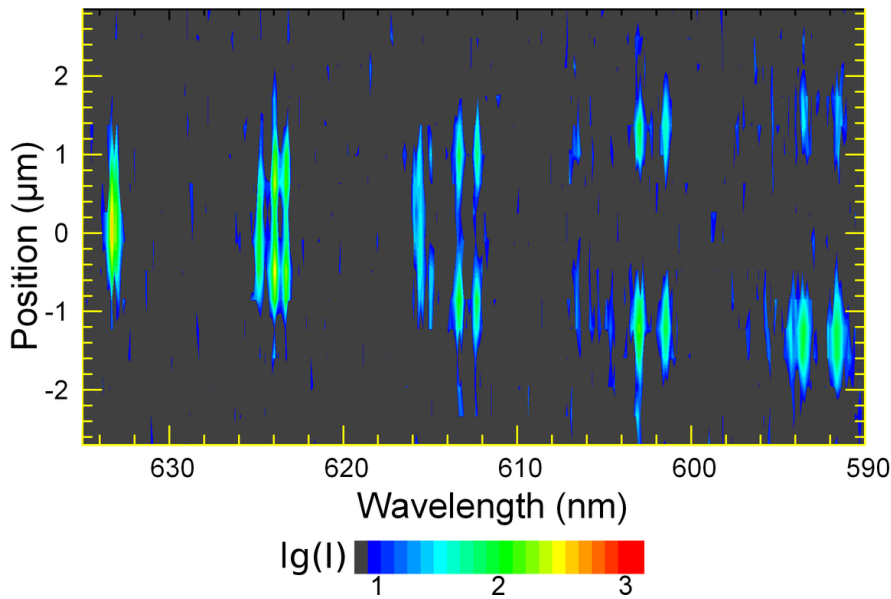
Figure 4.5: Local intensity distribution of the emission of a single photonic dot, excited with the diode laser at $405\,nm$.

In figure 4.5, the spectrum of a single structure can be seen, in this case at emission following optical excitation. The features are basically the same compared to the transmission picture, with the difference, that the photons are now generated in the box, instead of being inserted from outside. It can be seen that the intensity distribution of the modes concentrates more and more to the edges with increasing mode number. As a first approach for the field profile in the boxes, perfect reflecting sidewalls are

assumed as boundary condition. Thus, the resonant modes consist of standing waves of sine- and cosine-type in all three coordinates. As many of the box structures are close to $\lambda/2$ thick, $\mathbf{k}_z$ is fixed, and the energy of the modes can be derived via:

$$E_{n_x,n_y} = \sqrt{E_0^2 + \frac{\hbar^2 c_0^2}{n_{\mathrm{Org}}^2} \frac{\pi^2}{L^2}(n_x^2 + n_y^2)} \quad \text{with} \quad E_0 = \frac{hc_0}{2n_{\mathrm{Org}}d_c} \quad . \tag{4.3}$$

Herein, n_x and n_y are integers, explaining the numbers of antinodes of the standing waves, and E_0 is the energy of the fundamental cavity mode of a d_c thick resonator without lateral confinement. It should be noted here that the ground mode in laterally confined cavities is always shifted to higher energies, as the boundary conditions do not allow a state without a x- and y-component of the wave vector. This is, in theory, completely different in standard microcavities, where the fundamental mode could be assumed as plane wave with wave fronts parallel to the mirrors. Practically, optical losses and inhomogenities lead to a limited extent of the mode in space and thus to a similar but much smaller effect.
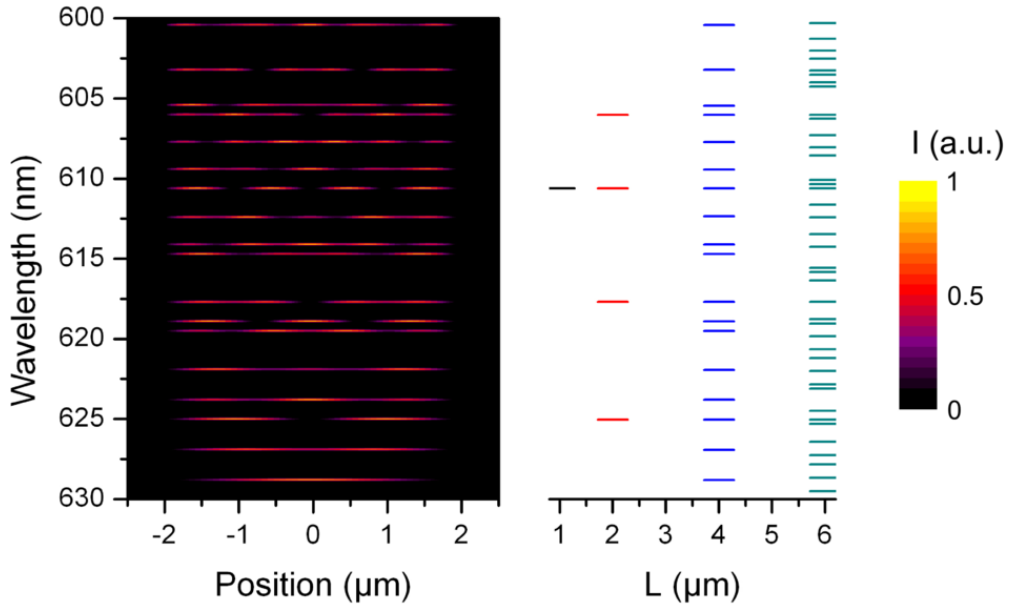

Figure 4.6: Integrated intensity profiles for the modes of a square shaped box, calculated for a $\lambda/2$ thick structure ($\lambda_D = 630\,\mathrm{nm}$) with $L = 4\mu\mathrm{m}$ and $n_{\mathrm{Org}}=1.75$. The trend to an increasing number of antinodes towards higher energies can be seen, together with a grouping of the modes. Right to this are the energetic positions of the respective modes for 4 different values of L. Besides the strong shift of the fundamental mode, the amount of modes per spectral window increases drastically.

In figure 4.6, the energetic position and lateral intensity distribution of the modes is shown for a box structure with $\lambda/2$ height at $630\,\mathrm{nm}$, a lateral size L of $4\,\mu\mathrm{m}$, and a refractive index of $n_{\mathrm{Org}} = 1.75$, using the above assumption for the simulation. The spectrum of each mode is space integrated along the axis perpendicular to the

abscissa, to cover all antinodes, which is important for the degenerated modes. In the experiment, the spatial extension is restricted with a cross-slit, as only one coordinate can be resolved by the spectrometer. Thus, the field profile is taken at a certain cross section (mainly central) and modes with nodes at this specific position will not appear in the spectrum. Within this model, the contribution of molecule emission to a specific mode number of degenerate states is equally weighted, which is sufficient, as no polarization dependence is involved, and the emitters in the experiment have an arbitrary orientation.

Most of the qualitative features can be clearly recognized in the simulation. A grouping due to the nonlinear distance between modes is visible together with the increasing number of antinodes in the spectrum. This also leads to the effect of the shift of maxima away from the center to the edges in the lower part of the spectrum. Right to this simulation, the energetic positions of the modes are plotted as a function of the lateral box size. The lines clearly demonstrate the increasing number of states per wavelength range towards a continuum for large "lateral confinements". Furthermore, it can be seen how the fundamental mode is shifted from the initial value of 630 nm for unconfined microcavities to higher energies in very small structures. A comparison of the mode distance from theory with the experiment leads to the conclusion, that an effective size is appropriate to use, instead of the physical size. A good compromise is found to be $\approx 3\,\mu$m, which can vary slightly across the samples. The origin of the effective side length is found in the preparation process, where shadowing effects may occur, which decrease the available lateral size.

When the optical setup is changed to the far field modus, the angle-dependent spectra are detected. As it can be seen in figure 4.7, the emission occurs in a region restricted by a dispersion parabola, similar to those of standard microcavities. Again, the discrete states are present and the emission of a certain state is not limited to the respective angle of the parabola, but also happens into the direction of the cavity normal. This is a consequence of the mode distribution in the box, which can be regarded as multiple phase-locked emitters, which form an interference pattern in the far field. To simulate these patterns, a Fourier transform of the internal field [63] can be applied:

$$I(\theta,\phi) =| \iint_{-\infty}^{\infty} \mathcal{A}(x,y) \exp{(\mathbf{k}\cdot\mathbf{r})}dxdy|^2 \quad . \tag{4.4}$$

The function $\mathcal{A}(x,y)$ defines the local amplitude of the respective mode, as it can be detected in the near field configuration. The result of this procedure can be seen in figure 4.8, calculated for the $\lambda/2$ box of $4\,\mu$m width. This time, the local field amplitudes are taken only from a central cross section (i.e. for x=0) of the box, thus neglecting the contribution of modes with a node in the center, which is the often
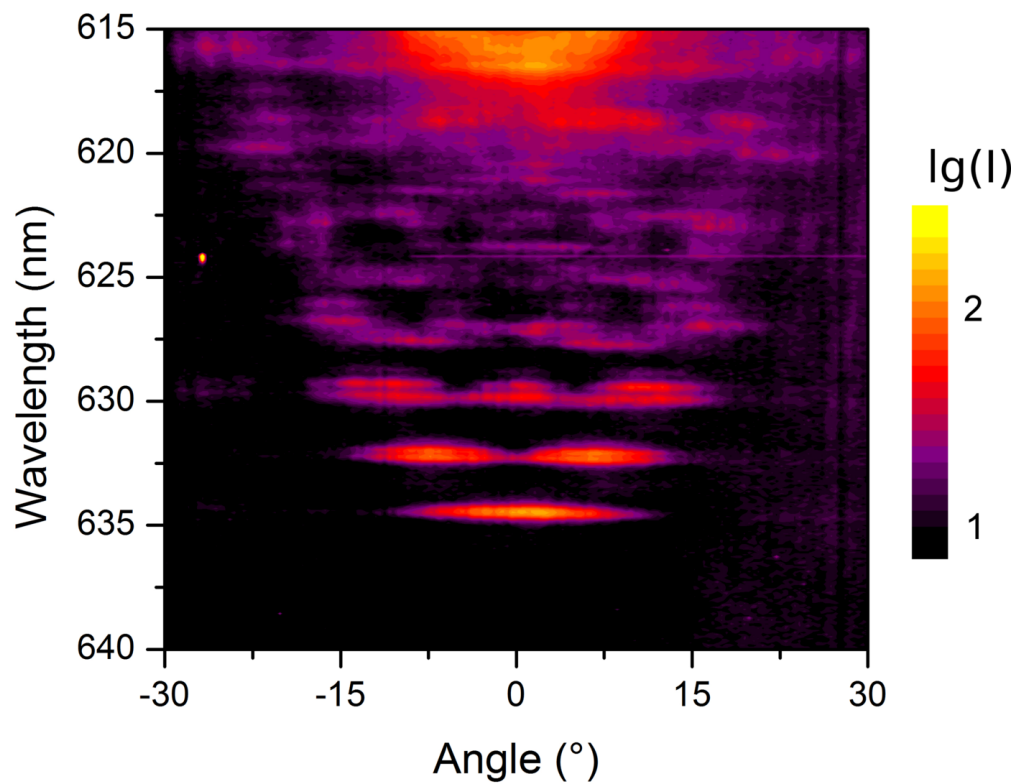
Figure 4.7: Far field spectrum of a single photonic dot. Like in the near field spectrum, discrete modes appear with an increasing number of maxima. Different to unstructured microcavities, the emission at higher mode energies can be detected even at small angles, although it is restricted to a parabola shaped region.

realized experimental case. The increasing number of antinodes in the lateral field profile leads to a larger angle of emission in the far field. This fundamental interplay between the distance of single emitters and the spread of the interference pattern also leads to larger emission angles for smaller box sizes and vice versa. The comparison with
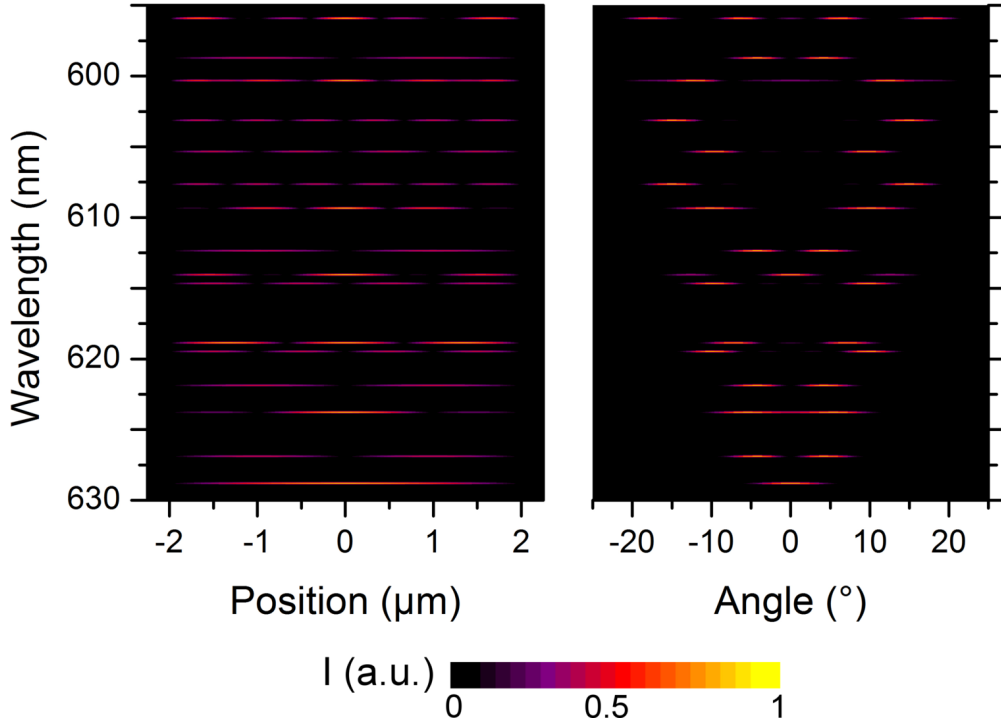

Figure 4.8: Central intensity profile for the modes of the square shaped box of figure 4.6. The far field simulation is calculated from a Fourier transform of the near field intensity distribution and shows similar qualitative features of the experiment, such as the central emission of some of the modes and the parabolic restriction.

the experimental spectrum shows a qualitative agreement of the intensity distribution of modes, but indicates again a smaller effective size than the physical one, as the observed angles are slightly larger than the simulation predicts. For the quantitative agreement, various modifications needs to be included in the simulation. The reflection coefficient and the refractive index need to be wavelength dependent, which alters the linewidth of the modes and the spectral position, respectively. Furthermore, the box design is not fully sufficient and should be replaced with a truncated pyramid, due to the shadowing of the mask during growth. This influences both, mode energy and intensity distribution in space, thus also in far field. Another aspect, which needs to be considered is the influence of polarization, which will be discussed in the next section.

4.2.2   Polarization influence on spectral position

A polarization splitting for microcavities due to the different penetration into the mirror layers might also play a role for photonic boxes, where the largest surface is sandwiched

between DBRs. However, also for 3D confined structures, in which the cavity mode matches the mirror design wavelength, one can observe a number of modes, which appear and disappear when a polarizer is inserted in the signal path. In addition to reflection at the bottom and top mirrors, here one must account for additional phase shifts due to multiple total internal reflections at the lateral interfaces, i.e. the side walls of a structure. The effect is often neglected, and, apart from Kuther *et al.* [63], no experimental observation of TE-TM polarization splitting due to total internal reflection was reported yet. Probably this is caused by a rather small splitting in inorganic structures (≤ 0.5 meV for micron-sized GaAs-based structures), as evaluated by several authors [26, 61, 64, 65], using a vectorial approach. Therefore, most of the experimental observations in such 3D confined systems were compared with scalar models, and a potential polarization splitting was attributed to an asymmetry of the structure. It is worth noting that one of the main reasons for observing a larger splitting in our samples is the broad emission spectrum of the organic emitter, and its large Stokes' shift [42]. In inorganic semiconductors, the spectral range would be obstructed by strong absorption features, inhibiting emission measurements.

The sample for this experiment is a laterally structured DBR microcavity with the dye system Alq_3:DCM (2wt%), having 21 layer TiO_2/SiO_2 - mirrors, and the extension of each shadow mask structured post is $5 \times 5 \, \mu m^2$. The design wavelength is set around 640 nm, close to the emission maximum of the dye compound. For the measurement, the confocal μ-PL setup is used in conjunction with the 407 nm diode laser at low power to remain in the spontaneous emission regime. With the help of a polarizer, TE and TM polarization with respect to the measurement plane are identified.

In figure 4.9 the μ-PL spectra are shown as a function of the emission angle for TM and TE polarizer setting and without a polarizer. The emission at wavelengths larger than 620 nm consists of resonator modes only, where the light is nearly completely confined in the box. The growing spatial delocalization of the modes within the dot in combination with a reducing mirror reflectivity leads to a broadening of the lines. For higher energies, the discrete lines become superimposed by a continuous parabola. An explanation for this effect is the smooth transition at the dot edges [66], which supports the emission of some outer lying molecules of the photonic dot to couple into the cavity mode of the neighbouring planar structure. In accordance, the continuous dispersion curve exhibits higher output intensities at larger observation angles, as the photons need some lateral component of the wave vector to enter the planar region between the photonic dots. The energetic offset of the cut off between the two overlaid dispersion dependencies is allocated to a slightly smaller cavity thickness of the planar structure compared to the height of the organic photonic dots. This is likely caused by small deviation during growth of the last layer of the bottom or the first of the top mirror.
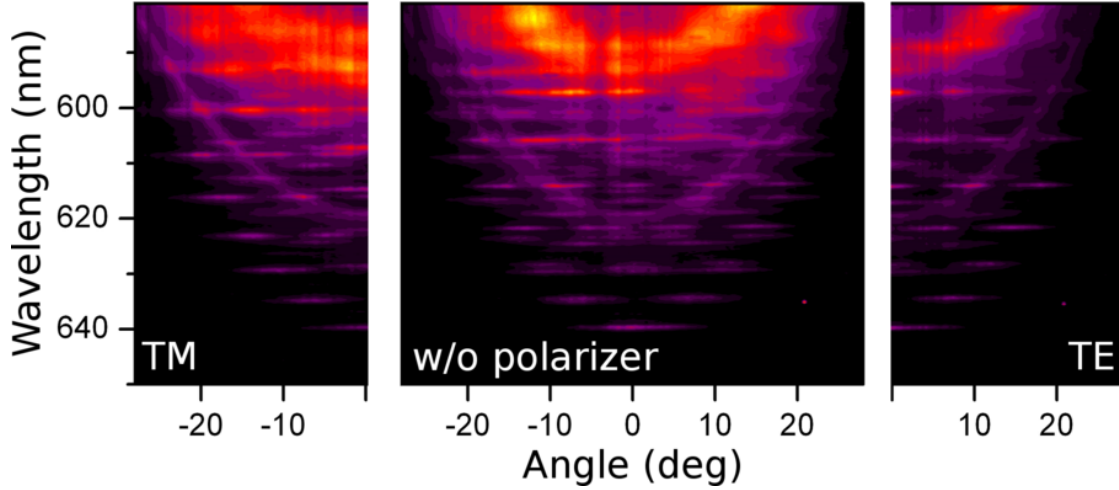
Figure 4.9: Far-field photoluminescence spectrum of a homogeneously excited organic photonic dot $(5 \times 5\,\mu\mathrm{m}^2)$ for TM polarization (left), without polarizer (center) and TE polarization with respect to the observation plane. Within the discrete states some spectrally separated mode doublets appear in the unpolarized spectrum, which separate into the respective polarizations. Additionally, the typical slope difference for the superimposed continuous mode is observed. The measurement was performed by former diploma student E. Siebert under my supervision.

A polarization dependent occurence of some of the discrete modes is clearly visible when comparing the right with the left panel. The superimposed line also splits in the unpolarized picture into two branches. This behaviour can be attributed to the splitting in a detuned planar MC, as described in section 4.1.1. In contrast, the distance of similar discrete modes does not depend on the observation angle, but instead on the energy of the respective mode. For higher order modes, it increases up to several nm.

As mentioned above, the origin of the polarization splitting of the discrete states of the photonic dots cannot be found in material anisotropies or detuning effects, but in polarization dependent phase shifts at the side walls. Following Gerard *et al.* [18], the energy and intensity distribution of 3D confined modes in a photonic box can be deduced from the guided modes of an equivalent waveguide. To model the structure, a $\lambda_c/2$ - slice of a slab waveguide with refractive index n_{slab} is set up, which is repeated Q times in z-direction. Here, Q is the quality factor of the cavity with thickness $\lambda_c/2$. With this approximation, one neglects entirely the polarization influence of the DBRs, which causes the splitting in planar microcavities. Again, this is a reasonable assumption as the organic cavity mode ω_c of the sample should match well the center of the stop band ω_s. Thus, only the reflections at the lateral boundaries contribute to phase shifts between light of TE- and TM-polarization. For simplicity, the structure of the adjacent layers in lateral directions is regarded as a single material with a background refractive index, $n_0 < n_{slab}$. The solution to this electromagnetic problem is known, and its eigenvalues may be calculated analytically [67] or with
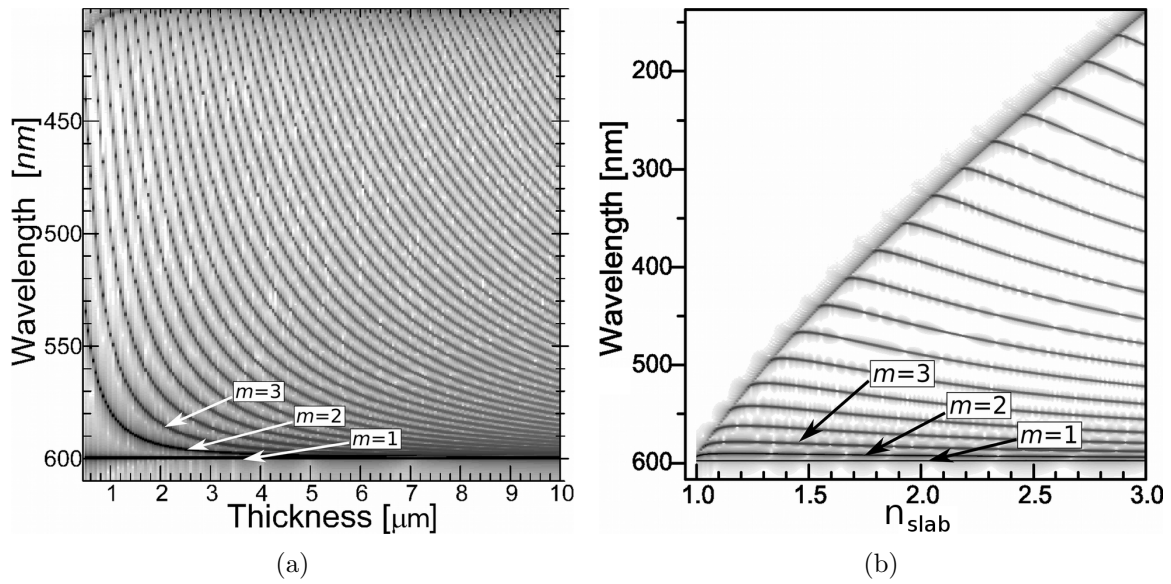
Figure 4.10: (a) Calculated positions of modes for various thicknesses of the waveguide ($n_{slab} = 1.75$ and $n_0 = 1.0$). The total number of modes increases drastically with the slab diameter, while their energetic distance decreases. (b) Dependence of mode number and position on the refractive index of the waveguide material n_{slab} for an air-post structure of $2 \times 2\,\mu\text{m}^2$. The spectrum and therefore the number of modes is limited by a spectrally decreasing cut-off wavelength λ_{cut} resulting from the increase of internal reflection and hence confined states for a larger difference of the refractive indices.

numerical tools, e.g. using finite difference methods.

The applied simulation routine calculates an effective mode index, n_{eff}^m, with m as the mode number, beside the lateral field distribution. With the help of the resonance condition $\lambda^m = 2\,n_{eff}^m d$, it is possible to recalculate the spectral position of the mode.

Figure 4.10(a) shows the resonant states and their spectral position of square shaped waveguides with a given diameter. Starting from 3 resonant states, their number increases non-linearly with the size of the waveguide, especially in the low energy range of the spectrum, which results here in a virtually continous band of modes. To see the influence of the index difference between the surrounding media and the cavity material on the mode position and total number, the refractive index of the waveguide is varied in another simulation, detaining a diameter of $2\,\mu\text{m}$. In the resulting graph (see Fig. 4.10(b)) one can identify a cut-off wavelength λ_{cut}, which is determined by the condition of internal reflection. The larger the photon energy is, the more the lateral component of the wave vector increases until the critical angle is reached. Photons of shorter wavelengths are not reflected at the sidewalls, but can escape the structure. The critical angle towards the longitudinal axis of the waveguide increases for a larger refractive index material. This results in a shift of the cut-off wavelength to higher energies and an increasing number of modes. The latter one is furthermore a result of the larger optical path for higher indices.
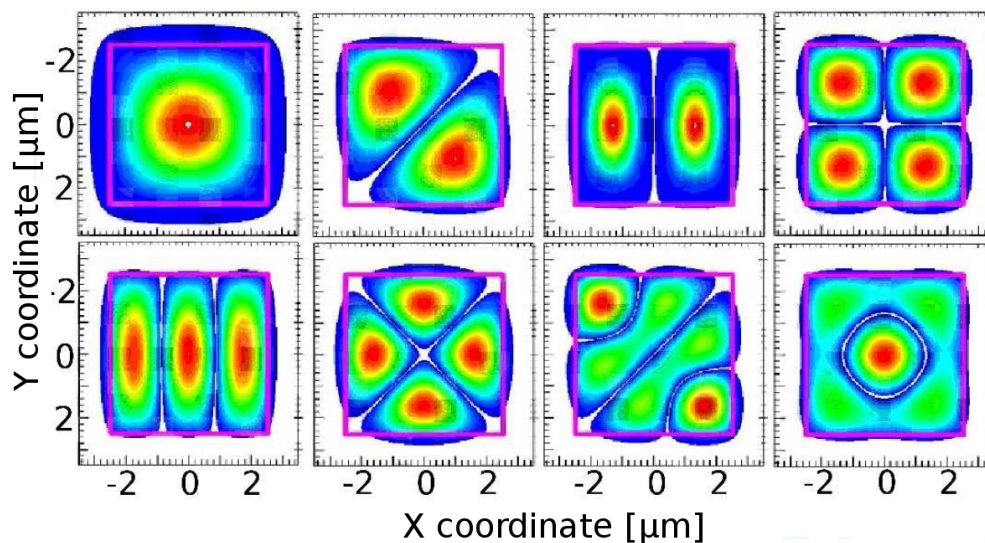
Figure 4.11: Spatial distribution of electric field amplitudes for the lowest energy transversal modes of a $5 \times 5 \mu m^2$ photonic dot ($n_{slab} = 1.7$). The calculation assumes an air-post structure ($n_0 = 1$) and shows the increasing number of antinodes as well as the different penetration depths into the surrounding.
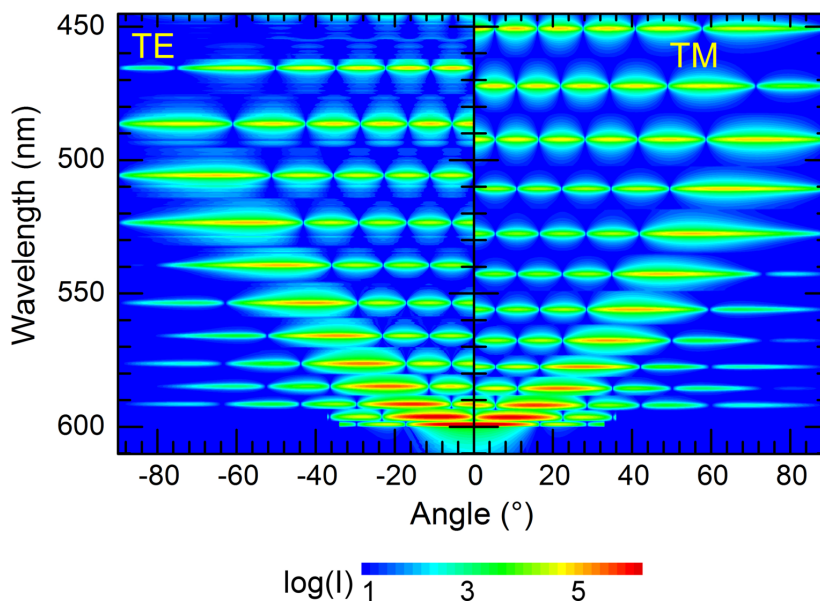
Figure 4.12: Calculated far field spectrum for TE and TM polarization of a $4.2 \times 4.2 \, \mu m^2$ structure ($n_{slab} = 1.75$, $n_0 = 1.0$). The slightly different spacing between the respective modes results in a polarization splitting.

Figure 4.11 presents the calculated spatial intensity distribution for the lowest energy modes of a $5 \times 5 \, \mu m^2$ footprint guide. It should be noted though, that some of the shown distributions are twofold degenerate in a perfect square shape, with their counterpart being rotated 90 degrees. Apparently, the electric waves penetrate into the surrounding forming an evanescent field. The increasing number of nodes and antinodes explains the number and spread of lines in the measurement, and was demonstrated in several experiments mapping the local field distribution [58,62]. The lateral mode profiles show no visible dependence on the polarization, thus, the energetic offset originates from different phase shifts during reflection at one of the side walls [25]:

$$\Phi_{TE} = 2 \arctan \sqrt{\frac{k^2 - n_0^2 k_0^2}{n_{slab}^2 k_0^2 - k^2}}, \tag{4.5}$$

$$\Phi_{TM} = 2 \arctan \frac{n_{slab}^2}{n_0^2} \sqrt{\frac{k^2 - n_0^2 k_0^2}{n_{slab}^2 k_0^2 - k^2}} \quad . \tag{4.6}$$

Depending on the mode number, multiple reflections take place at the lateral interfaces, even for the principal mode. The successive adding of a phase shift leads in sum to a different eigenvalue for the mode energy.

For the final simulation of the splitting, parameters are chosen as $n_{slab} = 1.75$ for the waveguide as a typical value for organics, $n_0 = 1.0$ for the surrounding, and a size of $4.2 \times 4.2 \, \mu m^2$. These values provide good agreement with the experimentally observed splitting and are noticeably smaller than the physical size, as for the approach with the box model. A Fourier transform of the local intensity profile of each mode together with its energetic position allows to determine the far field spectrum. The result is shown in Fig. 4.12, for TE- and TM-polarization with respect to the observation plane. The angular intensity distribution for both polarizations is the same, but the lines appear at different energy eigenvalues. The modes are more closely spaced in the TM case in comparison to TE polarization. This effect results in splitting values up to a few nm. In analogy to the experiment, the distance increases from zero for $m = 0$ to larger splittings for higher order modes, as the reflection angle towards the sidewalls increases. In summary, the different phase shifts during reflections at the side walls of a photonic dot provide a reasonable explanation for the observation of polarization splitting of the resonant states. The applied technique of expansion of the $\lambda/2$ box to a corresponding waveguide is suitable to provide spectral positions and field profiles of the modes, which also show a good agreement with the ones deduced analytically in section 4.2.1. Improvements of the model are possible, regarding the spectral response of the cavity material and the surrounding as well as taking into account the phase sensitive nature of all reflectors. An even more complicated mode structure will arise, when birefringent active materials are applied, or the side lengths of the box vary.

Since this increases the number of states and thus reduces the effective emitter count for a certain wavelength and polarization, it is not desirable for the realization of an efficient organic laser.

5 Lasing from laterally modified organic cavity systems

In this chapter, the stimulated emission properties of microcavity structures are presented. At the beginning, the lasing in a standard planar sample is shown for comparison, followed by a closer analysis of the influence of emitter concentration and pumping condition on the threshold. Additionally, the stability of the emissive compound is investigated, before the lasing of photonic boxes is characterized. Here, the improved perfomance and the simultaneous stimulated emission into many modes is of special interest, as this differs from planar systems and provides some interesting features. The chapter is finished with an analysis of the lasing performance at close distance to an extended metal contact, incorporated in the central cavity layer.

5.1 Planar systems

5.1.1 Input-Output behavior, laser threshold

Since the first demonstration of organic solid state microcavity lasing by the group of Tessler [9], various experiments have been performed [13, 15, 43, 68–70] using either vapor deposited small molecule or polymer layers. The application of dielectric resonators on one or both sides enables high quality factors, which in combination with efficient dyes supports lasing (much) below the damage threshold of the material, often at room temperature.

The samples presented in the following consist of a 10.5 pair mirror on both sides of a $\lambda/2$ - layer, containing Alq_3:DCM with typically 2wt% doping ratio. For the measurement of the spectrum and lasing characteristics, the micro-photoluminescence setup is used in far field configuration. To obtain the input-output characteristics, the incident beam of the pump laser is attenuated with neutral density filters.

Figure 5.1 shows the far field spectra of a microcavity at three pumping powers, slightly below, exactly at, and slightly above the lasing threshold. In all three graphs, the cavity mode parabola is visible, with the apex at 622 nm. Additionally, one can
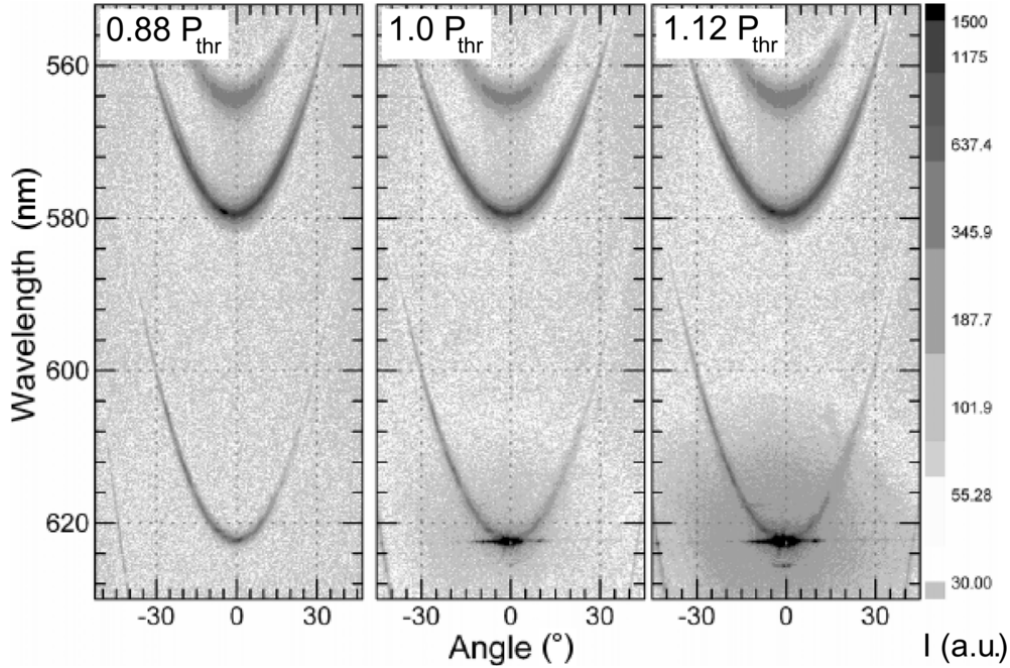
Figure 5.1: Far field spectrum of a microcavity, excited at three different incidence energies near the lasing threshold. The parabola at 622 nm is the cavity mode, whereas the parabolas below 580 nm originate from residual emission through the mirror modes at these spectral positions. The lasing is restricted to the fundamental mode and thus mainly emitted perpendicular.

see two parabola, which stem from residual emission through the highly transmissive mirror modes. The onset of lasing is concentrated in the $\mathbf{k_x}, \mathbf{k_y} \approx 0$ wave vector region, which can be seen by the distinct peak intensity at the fundamental mode. The increase of the pump power does not change this effect, but the overall intensity. An angular divergence is visible, which shows up as extension of the emission to $\pm 10°$. Whereas, the outer part of this can be attributed to blooming of the CCD, the central fraction results from the the small excitation spot (diam. $\approx 5 \,\mu$m).

The input-output curves of two similar microcavities with different cavity mode positions are presented in figure 5.2 in log-log plot of emission intensity over the pump energy. One can clearly distinguish the three regions of spontaneous emission regime, transition region, and stimulated emission by the different slopes. Although the emission at 594 nm is rather far away from the gain maximum of the compound, the difference between both curves is not pronounced. A similar result was also obtained in a cavity with a wedge shaped central layer, where the lasing threshold did not change drastically along a shift of the cavity mode of nearly 50 nm [71]. The stability of the system in the considered range of pumping can be seen by the fact, that no significant intensity drop is apparent, although more than two orders of magnitude of pumping above the threshold are applied and the values are recorded multiple times. For the measured points, a fit with the standard rate equation of Yokoyama (see equation 2.42)
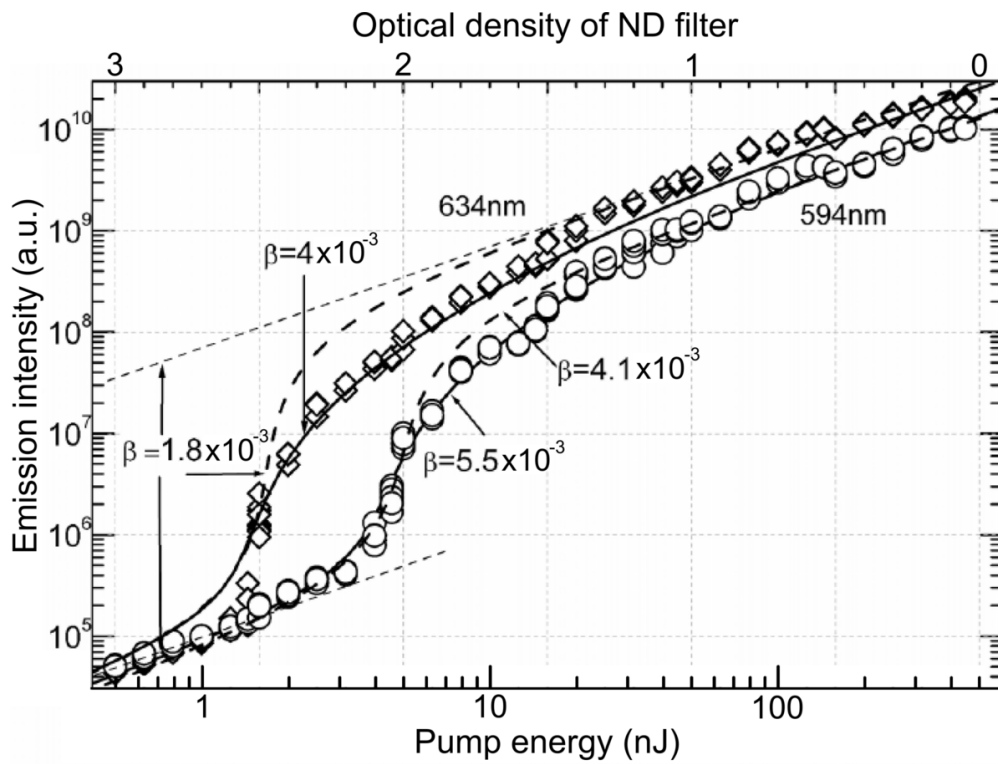
Figure 5.2: Input-output curves for two microcavities with different spectral cavity mode positions. The values are fitted with the steady state standard rate equation (dashed curves) and the formulae including inhomogeneous broadening (solid lines). The such extracted β-values are in the range of 2-5×10^{-3} and the lasing starts at 1.25 nJ (634 nm) and 3.2 nJ (594 nm).

is performed, and the best result is plotted as dashed curve, together with the derived β-value. The numbers are typical for a $\lambda/2$-cavity of the given quality and indicate that 1-2 out of approximately 500 photons in the microcavity contribute to the lasing process. As already pointed out in section 2.4.1, the linear regimes are fitted with good coincidence, whereas the transition region shows a clear offset. To match this part, the modified equations including inhomogeneous broadening are applied, which fit the data points much better. The central β-values are indicated in the figure and vary only slightly from the ones derived with the standard equations.

5.1.2   The experimental influence of DCM concentration

The use of the Alq_3 matrix for an effective emission of the DCM molecules is necessary to avoid quenching occuring e.g. via excimer formation or bimolecular annihilation. A neat layer of DCM has low luminescence, whereas the diluted layers show quantum efficiencies close to unity [72]. This is one of the reasons why they are widely applied in organic semiconductor lasers [12,15,73,74]. Another reason is the high tunability of the lasing process [71] and the possibility to use the Förster-transfer for indirect pumping below a reasonable absorption of DCM. Due to the interplay between both emitter molecules and the residual Alq_3 emission in case of low concentrations, the spectrum of the dye compound changes together with the luminescence efficiency [12,75,76]. To investigate whether this dependency has a strong influence on the lasing threshold in the microcavity or on the stability, a set of samples is prepared with identical mirror layers, but a variation of DCM concentration along the cavity layer. As a side effect of this measurement, it might be possible to explain a bad performance of samples originating from concentration fluctuations during preparation or find experimentally an optimum value.

The microcavities consist of 21 layers of TiO_2 and SiO_2 on borosilicate glass, followed by the co-evaporation of the organic layer. To achieve the concentration gradient in the active region, the sample rotates at high speed above both dye crucibles, masked each with an opening, which varies in diameter along the radius. The amount of DCM in Alq_3 changes three times along the 2.5 cm width of the sample. A set of samples with low concentrations vary from 0.7 to 2.2 wt%, another set from 1.4 to 4.5 wt%. This is on one hand the region where the maximum yield of the compound should be located [12] and on the other hand the worst case deviation assumed during the usual preparation of the microcavities.

For the measurement of the lasing characteristics, the frequency doubled 400 nm, 5 kHz beam of the fs-system is applied. The pump intensity is varied with neutral density filters in the path. The focussing with a parabolic mirror results in a diameter of the excitation area of 50 μm. With a micrometer stage, three positions of each sample

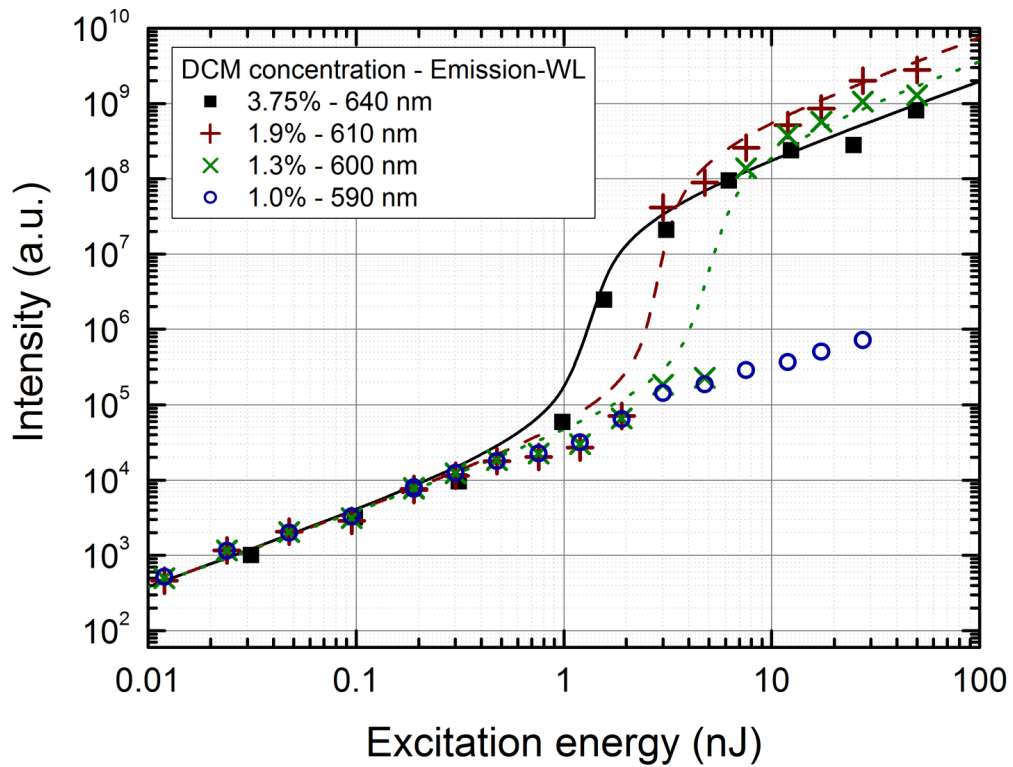**Figure 5.3:** Emission intensity over pump energy for various emitter concentrations of DCM in Alq_3 following pulsed excitation at 400 nm. The two highest and two lowest concentrations belong to one sample each with a three times concentration gradient of DCM. Besides the 1.0% - concentration position, where no lasing is observed, all positions show stimulated emission with similar threshold and coupling factor β.

are selected (high, medium, low concentration) and measured twice at a parallel spot. For the detection of the signal, the integrated output of an imaging CCD spectrometer is applied. At low excitation power, the measurement is integrated for 10 s, which is stepwise reduced to 0.1 s for the maximum values. To exclude that degradation during the high power pulses modifies the maximum intensities, a few measurements are repeated backwards and they show no visible deviation of the initial values.

In figure 5.3, the input-output curve for 4 emitter concentrations is depicted with the concentration and the corresponding emission wavelength. Although carefully adjusting the masking to achieve the concentration gradient along the cavity layer, a slight shift of the spectral position of the lasing mode is present. This might alterate the position of threshold, but not on a large scale, as the influence of the mode position on the threshold is not very pronounced [71], and the emission spectrum of the compound itself shifts to the red for higher concentrations of DCM.

The obtained curves look similar, thus indicating a comparable quality of the cavities at each measured point, which is supported by a low variation of the coupling factor β ($3 \pm 2 \times 10^{-3}$). Apparently, the position with just 1 wt% of DCM cannot be inverted in the regarded pumping range. Although one might benefit from a momentary storage of pump energy in the Alq_3 matrix (long radiative lifetime of 20 ns [15]), which could result in a subsequent Förster-transfer after the initial one, the number of photons, emitted by the DCM molecules within the cavity lifetime is too low. At slightly higher ratio, the onset of stimulated emission can be clearly discerned and is in the low nJ range. The threshold reduces with increasing concentration, as the effectivity of the Förster-transfer and the total number of DCM emitter molecules increases. Figure 5.4 presents the obtained values for the different concentrations.

Although not varying on a large scale, the difference of the thresholds is exceeding a simple proportionality between number of molecules and pump energy. Instead, a minimum at ≈ 2.5 wt% occurs, with nearly 10 times smaller threshold than the 1.3 wt% value. This is explained by the indirect pumping via the non-radiative Förster-transfer, which becomes more effective when half the distance between two emitter molecules approaches or becomes less than the effective Förster-radius R_0. In case of the compound Alq_3:DCM, this is equal to one dopant per ≈ 6 matrix molecules ($R_0 = 32.5 \mathring{A}$). The following increase of the threshold for high concentrations seems in this context contradictory, but can be attributed to a higher aggregation and the residual absorption of the emitter molecules at the lasing wavelength which becomes relevant. These results agree well with those obtained by the group of Forrest [12] in slab waveguides. They show an optimization potential to minimize the lasing threshold of this compound in microcavities, but its extent is rather small.
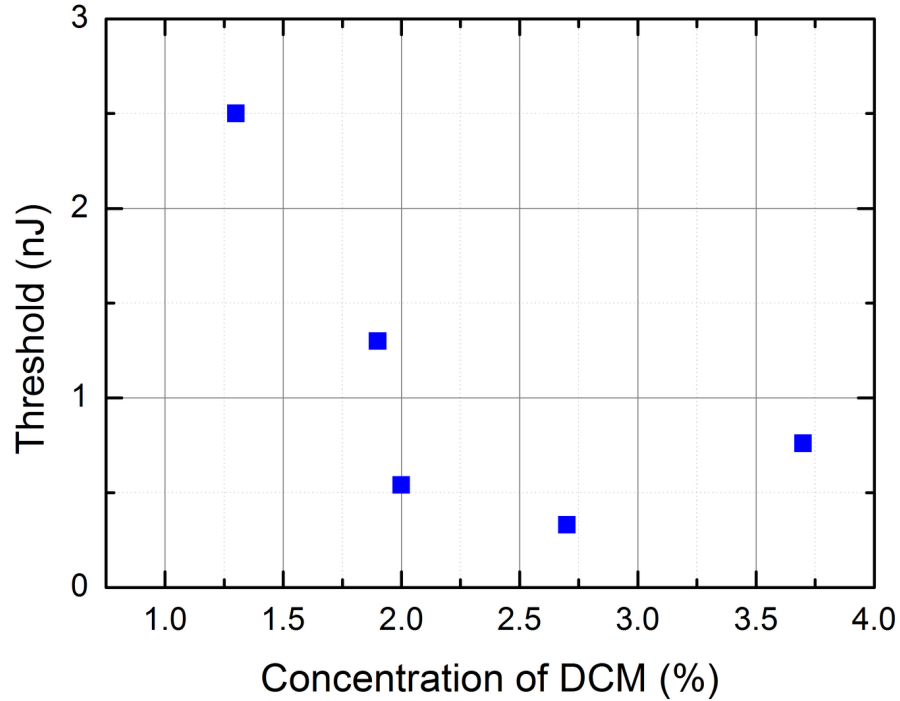
Figure 5.4: Threshold dependence on the concentration of DCM in the Alq$_3$ matrix. It decreases to a dip at ≈ 2.5 wt%, due to the enhanced Förster-transfer for a smaller average spacing of the dopand molecules. The subsequent increase is related to an increasing aggregation of DCM and an increasing residual absorption at the lasing wavelength.

5.1.3   Different pumping regimes and saturation

Instead of using the Förster-transfer for the pumping of the system, one can directly pump the DCM molecules at their absorption band and use the Alq$_3$ as a solid, reasonably transparent matrix. This might be of interest, to compare both pumping regimes about the respective threshold power, as well as to estimate the ratio of molecules needed to excite for lasing. As the maximum absorption of the host guest system is located at ≈ 495 nm, the output of the optical parametric amplifier is used to excite the sample in the same configuration as described in the last section. The sample with the lower concentration is excited at 512 nm, and the higher concentration one is pumped at 500 nm. The chosen positions and thus concentrations of DCM are identical to those of the indirect pumping via the Förster-transfer from Alq$_3$.

In figure 5.5, the measured curves for 4 concentrations are shown together with corresponding fits. They coincide at large with the measurement presented in figure 5.3, especially the threshold levels differ only weakly. One could expect a different behaviour, as for the direct pumping of DCM, 30-100 times less molecules are absorbing the incident photons compared to the case of the excitation of Alq$_3$ at 405 nm. The measured absorption of a neat $\lambda/2$-layer containing 2wt% of DCM in Alq$_3$ is $\approx 65\%$ of the incident power at 400 nm, and $\approx 25\%$ at 500 nm, which corresponds to a nearly
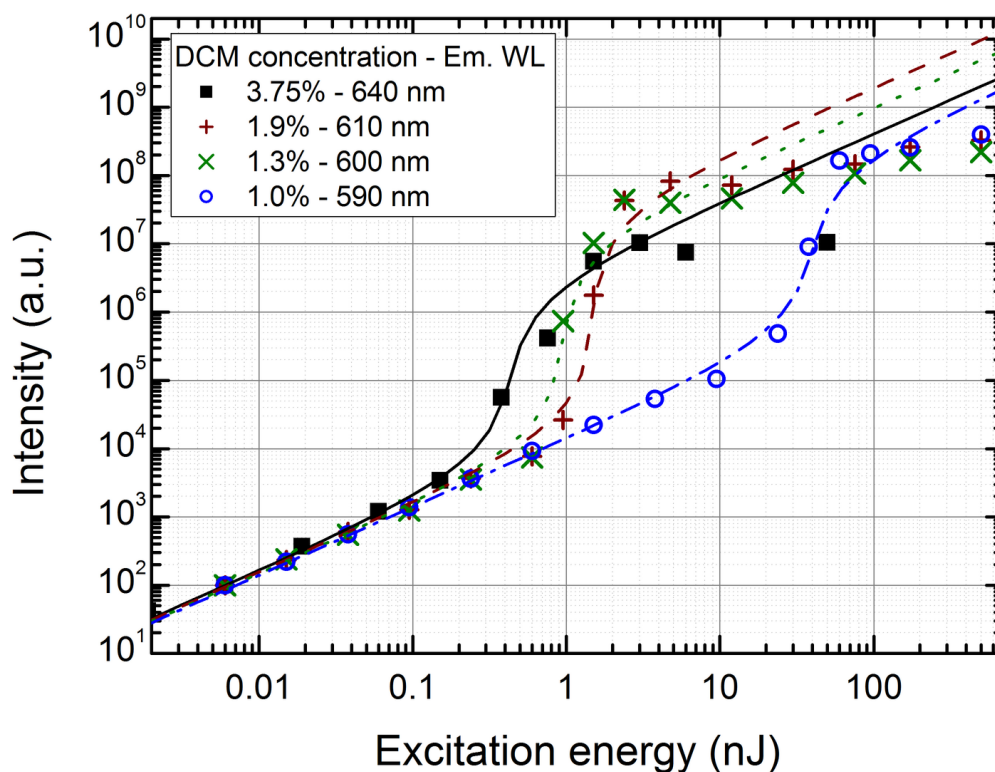
Figure 5.5: Input-Output curve for direct pumping of DCM (500/512 nm) at different positions in the concentration gradient samples. Similar to the results at 400 nm pumping, the lasing threshold for DCM amounts larger than 1% differs not significantly, whereas the lowest concentration shows a nearly two orders of magnitude higher transition energy. For all measurements, a clear deviation from the theoretical curves (lines) above the threshold is apparent, caused by an absorption saturation.

14 times higher absorption cross section of the DCM molecules compared to Alq$_3$. The dielectric mirrors modify only minimally the absorption of the layer via multiple round trips, as both excitation wavelengths are located outside the stop band, so the reflectivity is rather low ($\approx 50\%$). Additional to the difference in the absorption cross section, transfer losses can be found, which align the threshold of the indirect and direct pumping schemes. First to name is the Förster-transfer rate, which is directly proportional to the luminescence efficiency of the host Alq$_3$ ($\Phi_{PL} = 35\%$ [12]). Furthermore, non-radiative losses occur, e.g. exciton-exciton annihilation [77], which reduce the transferred amount of energy to the emitter. By summing up all parameters, the necessary power for inversion in this system is by chance independent of the pumping scheme.

A significant difference can be seen above the lasing threshold. Instead of a slope of unity, the intensity increases just slightly or stays constant. A degradation effect is excluded by repeated high power measurements. This effect needs to be accounted to the low relative number of emitters, which can contribute to the lasing process. A 2wt% DCM concentration in the considered excited region of 50μm diameter means $\approx 1\times 10^{10}$ emitter molecules ($\rho_{Host} = 1.6$g/cm^3, molecular weight of Alq$_3 \approx 460$ g/mol). At the excitation wavelength of 500 nm, a threshold energy of 1 nJ and ideally 25% of the photons being absorbed, one has 6.3×10^8 inverted molecules. This gives, at least, 1-2 orders of magnitude reserve of intensity above the onset of lasing, not considering non-radiative losses of excited molecules and/or inactive molecules, e.g. by degradation or defects during evaporation. To simulate the behaviour above threshold, curves are fitted to the measurement using the modified rate equations 2.46 - 2.48. Figure 5.6(a) shows the result for three concentrations, with varied molecule numbers. The sublinear increase of the intensity above threshold is matched much better, as the limited number of emitters is now included.

In figure 5.6(b), the lasing threshold values are plotted along the concentration of the DCM molecules. Different to the indirect pumping, no distinct minimum can be seen, as for this pumping scheme, just the amount of active emitters is important. The difference between the 1.9 and 2 wt% value may originate from the slightly more effective pumping at 500 nm. Nevertheless, the decrease with approximately one order of magnitude per 5% will not continue further, as the losses will increase, the denser the DCM molecules are arranged. In summary, the green pumping with very short pulses shows already the limit, at which these systems are operated. When longer pulses are applied, multiple excitations during the pulse duration can shift the saturation region away from the threshold, as it can be seen, e.g. in figure 5.2.
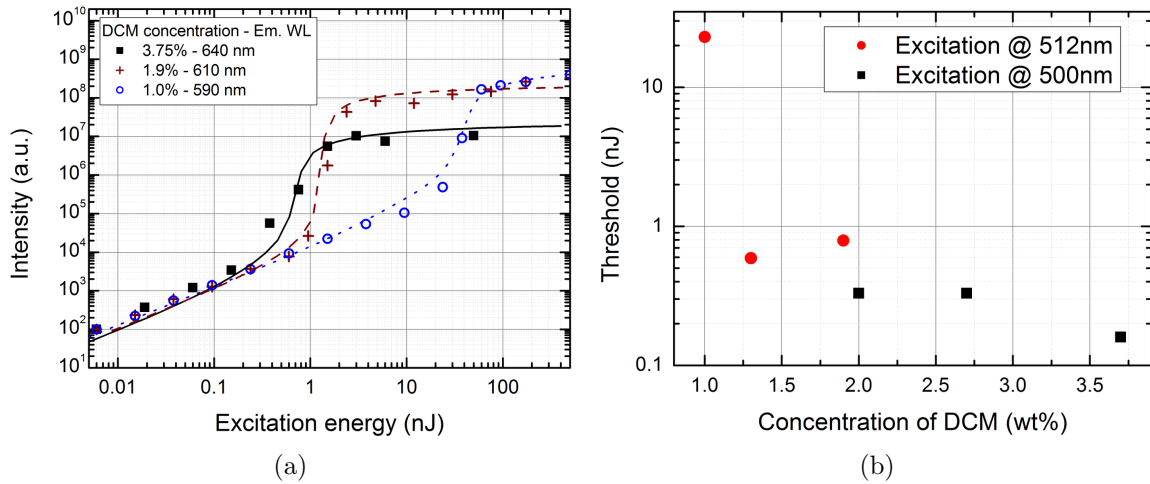
Figure 5.6: (a) Fit of the measurement data for three concentrations, using equation 2.46 with parameters $k_t = 1 \times 10^{13}\mathrm{s}^{-1}$, $A = 2.5 \times 10^8\mathrm{s}^{-1}$ and a pulse duration of 120 fs. The part above the lasing threshold is approximated better in comparison to the standard model. (b) Progression of the threshold values in dependence of the DCM concentration. After the initial drop, the threshold reduces slightly with the DCM concentration and has a minimum at the maximum ratio of dopant molecules.

5.1.4   Degradation

The question of material stability is raised during the input-output measurements, especially at high pumping powers. For the ease of sample manipulation and also the quality of the optical system, no external protection is applied, and all samples are investigated under ambient conditions at room temperature. Thus, there is a vulnerability of the organic layer against oxygen and water, which can penetrate the top-DBR due to its micro-porosity. From literature, some information can be gathered for degradation mechanisms of neat and DCM-doped layers of Alq_3, e.g. photoinduced aggregation of the dye molecules [78], oligomer formation and bleaching of the DCM [79], photodegradation of Alq_3 [80], and its reaction with water [81]. To avoid any unnecessary damage of the cavity layer during most of the measurements, the excitation beam is blocked except for the short integration time during the measurement. If an indication of destroyed emitter molecules is apparent (drop or decrease of slope), a backward detection of some points is performed to see a difference to the former signal. In the following, the results of some systematic measurements are presented, where standard microcavity samples and box structures are continuously pumped at different energies.

For the unstructured microcavity, a sample with 2wt% of DCM is excited at 5 kHz with 120 fs pulses either at 400 nm or 512 nm. The area is excited for several minutes and a spectrum is recorded every 1 to 5 s, depending on the total measurement time. To check the influence of the lasing process, the intensity of the incident beam is first

reduced far below the previously determined threshold and then, at a slightly shifted position, the measurement is performed in the lasing regime. In case of the stimulated emission, a simple detection of the input-output curve before and after the kinetic series is applied, to see if lasing still occurs. For the measurement of structured microcavities, a sample with boxes was analyzed with the 400 nm beam of the home-built system, at a 5 times lower repetition rate of 1 kHz.

Figure 5.7 shows the determined evolution of the emission peak against the exposed time. It is not surprising that the intensity drop is more pronounced in case of excitation
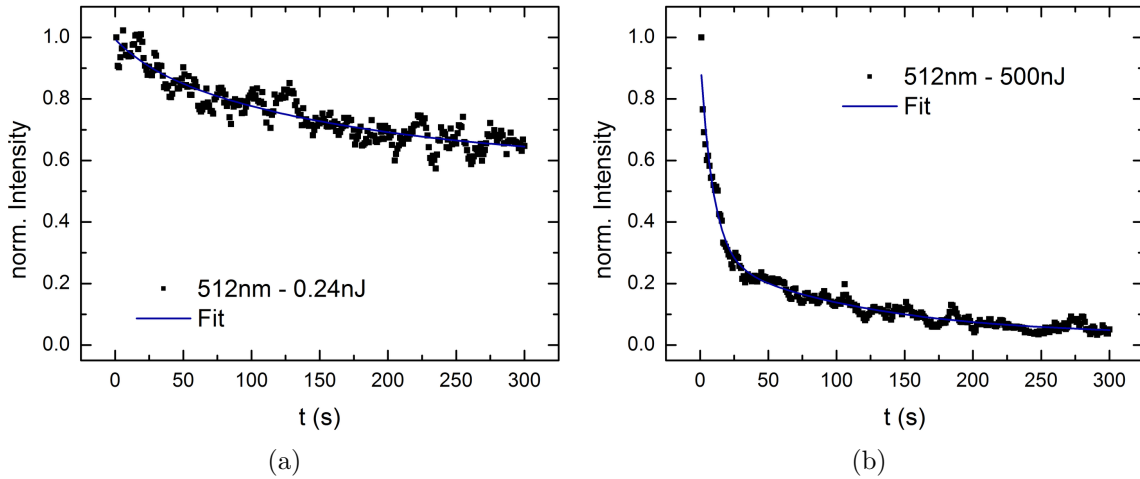

Figure 5.7: (a) Decrease of peak intensity for 512 nm pumping of a $\lambda/2$ microcavity at 0.24 nJ below the lasing threshold and (b) above at the maximum output of the pump laser of 500 nJ. The exponential-type decay, which is present in both graphs, is accompanied by an initial fast drop in the case of lasing.

with high energy, as the amount of non-radiative losses and photoinduced degradation mechanisms depends on the number of absorbed photons and thus pump power. As a first assumption, a single exponential decay might fit the data points, but especially above threshold, the use of two decay parameters gives a much better result, in the form of:

$$I(t)/I(0) = A + B \cdot e^{(-t/t_1)} + C \cdot e^{(-t/t_2)} \quad , \tag{5.1}$$

which gives for the high pumping case a short half life of $\approx 7\,\mathrm{s}$ and a longer one of $\approx 80\,\mathrm{s}$. The short time can be attributed to initial effects, such as reorientation of molecules and breaks of bonds. The slower processes are more related to chemical reactions with residual water or oxygen in the microcavity or the surrounding, induced by the excitation of the molecules. Alternatively, a stretched exponential decay [82] in the form of $\propto exp(-t/\tau)^a$ could be fitted to the data. To compare results of different pumping regimes and energies, it is not useful to operate in the time domain, but instead in the energy regime. The amount of energy in each pulse is therefore accumulated over the frequency of the pulse and measurement time. Still, there are error sources

when different pulse lengths and repetition rates are combined, regarding bleaching or deviating regeneration times.

Figure 5.8 presents the result of this procedure for indirect (400 nm) and direct (512 nm) excitation of the DCM in the microcavities. In each case, measurements are performed below and above the threshold, and for a comparison, data of the fundamental mode of a photonic box, excited at 400 nm but with 1 kHz are plotted in figure 5.8(a). For the 400 nm pumping of the standard microcavity, only a weak variation can be seen for the low excitation energy, whereas the pumping above threshold shows a stronger decay. Nevertheless, it does not drop remarkably and is at the end of the measurement still orders of magnitude above the signal for spontaneous emission. This can not so easily be discerned in case of the photonic box cavity, where, due to the higher β factor, the distance between the lines is only one order of magnitude. Also

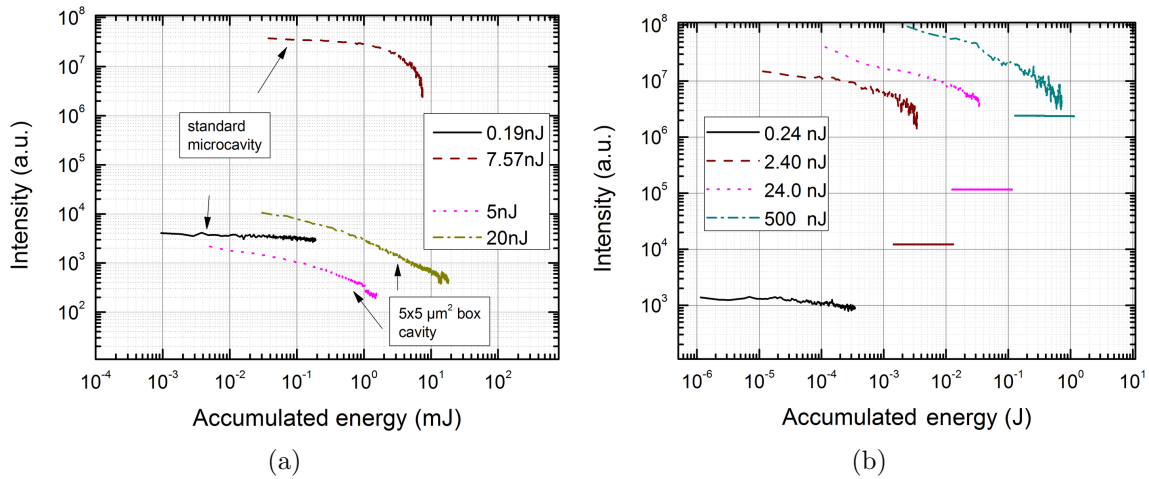(a)   (b)

Figure 5.8: (a) Decay of the peak intensity over the accumulated energy for pumping at 400 nm below and above the threshold. Presented are curves for a standard microcavity and a photonic box structure. (b) Signal decrease for pumping at 512 nm, recorded below and for three values above threshold. The horizontal lines indicate the energetic position of the spontaneous emission branch, estimated by an extension of the first linear part of the input-output curve.

in this case, an abrupt intensity drop is missing for the measurement above threshold. Compared to the unstructured microcavity, the signal decays on a lower level, which is either due to the lower duty cycle or a result of the better coupling of the molecules to the mode, which shortens the time of the excited state before a photon is emitted.

Similar results of the intensity decay can be seen for the green pumping (figure 5.8(b)). To obtain an idea whether the mode is still in the lasing regime, lines indicate the hypothetical intensity of spontaneous emission at the given pumping energy, derived from the input-output curve. In all cases, the stimulated emission regime should still be present, as no crossing of the lines is visible. Summarizing the measurement and fit results, the degradation process is weaker for higher energy pumping in terms of

the total amount of excitation energy. This is reasonable if one considers the fact that the release of absorbed energy is much faster in case of stimulated emission, and thus, some of the photoinduced processes are reduced.
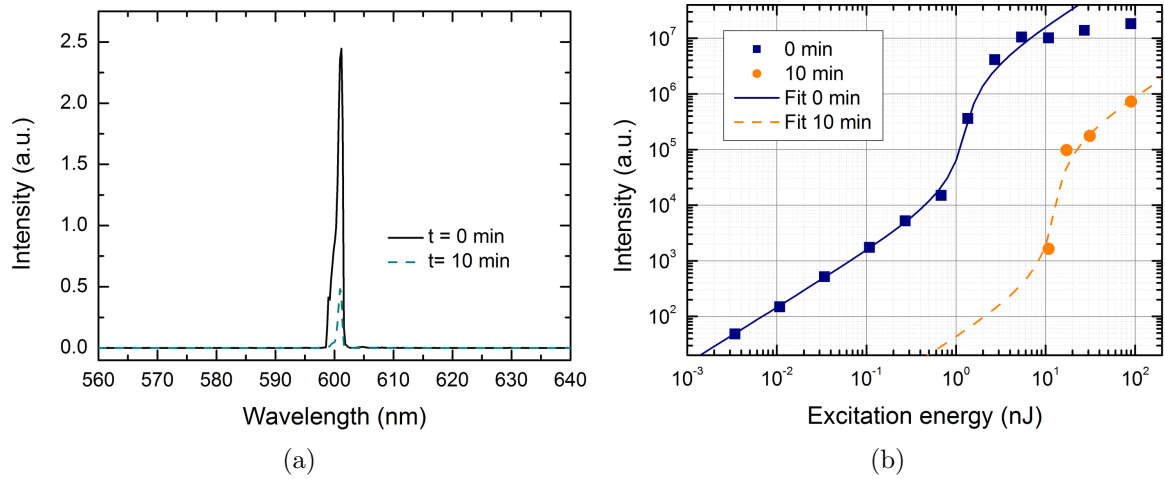

Figure 5.9: (a) Emission spectrum at the beginning and end of a 10 min degradation measurement with 512 nm excitation at 90 nJ. Although, the intensity reduces severall times, the overall shape and linewidth stays constant. (b) Input-output curve, taken before a degradation measurement and after 10 min. Although the intensity drops remarkably, lasing still occurs, as a distinct threshold is visible. It is shifted approximately one order of magnitude to higher energies due to the decreased number of active molecules and added absorption.

For a clear proof that the lasing capability of the sample itself is not affected by the degradation mechanisms, the spectrum and input-output curves before a 10 minutes series of 512 nm excitation is recorded (see figure 5.9). The linewidth of the emission remains narrow and the intensity progression still has a kink connecting the spontaneous and stimulated emission regime, although the threshold is now shifted to higher energies. From the previous results of the concentration dependent measurements, this shift cannot alone be attributed to a lower number of emitting molecules, but is also due to increased losses, as the levels of spontaneous emission should be more aligned. Regarding the experimental results, it might be of interest to pump the system for a such long time that the transition between the emission regimes can be detected, to see the ultimate limit. It is however remarkable that several million laser pulses can be obtained from the investigated systems, without any special protection, even from the fragile photonic box structures.
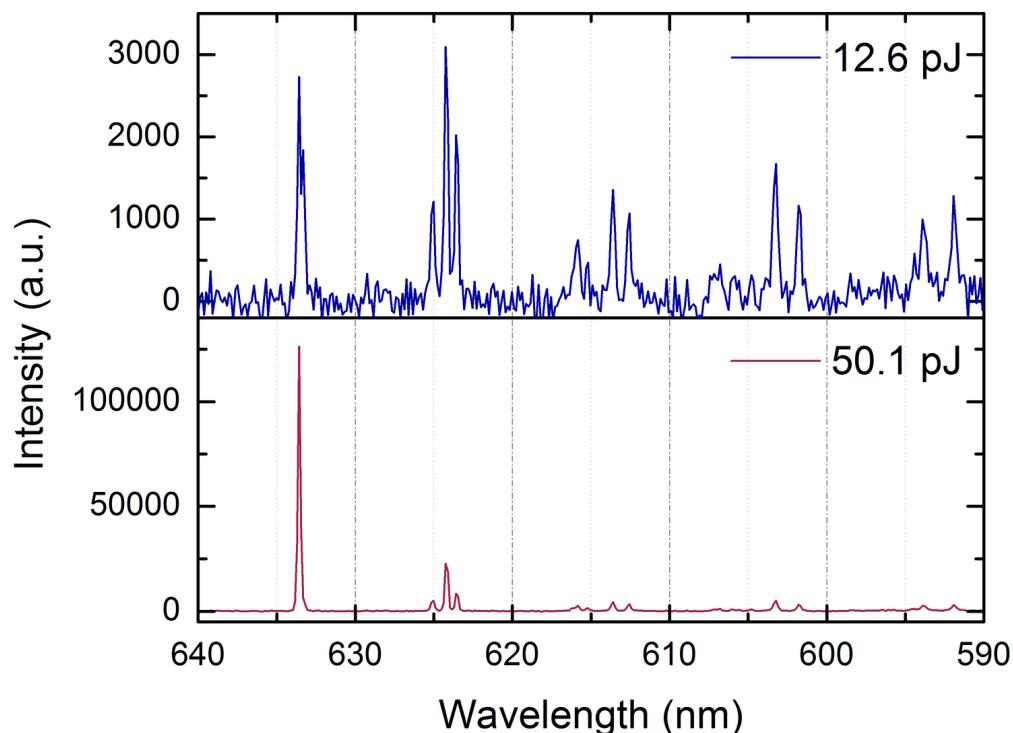
Figure 5.10: Emission spectrum of a single excited photonic dot (532 nm, 1.5 ns) for two pumping energies. Whereas at low power, the intensities of the various modes are in the same range, the fundamental mode is in the lasing regime for higher pumping.

5.2   Laterally structured organic microcavities

5.2.1   Impact on laser characteristics

From the theoretical consideration of chapter three follows that an additional lateral confinement of light in the microcavity influences the laser operating characteristics, besides the modification of the mode spectrum. The spontaneous emission rate into a mode is strongly affected by the properties of the cavity, i.e. it increases with larger quality factor (Q-factor) and decreases with larger mode volume [83,84]. The enhanced spontaneous emission to a resonant mode in combination with the modified mode structure in the photonic boxes alters the fraction of photons which can couple into these modes (β-factor). This was shown in experiments with inorganic 3D - confined systems [85–90], where the stimulated emission typically occurs with higher β-factors and lower thresholds [91]. From these results, it is not consequent that stimulated emission may also happen in the organic photonic box structure, since the broad emission spectrum in combination with equivalent densities of state might reduce the number of suitable emitters to a level, where the necessary lasing threshold overcomes the stability of the molecules. Nevertheless, it is possible to invert the system and obtain lasing with some interesting properties, which will be discussed in the following.

The investigated organic photonic dots are produced with the technique described

earlier, although for many of the investigated samples, the $\lambda/8$-buffer layer (see section 4.2.1) is applied together with a thickness wedge of the active layer. Thus, it is possible, to find positions on the sample where the fundamental mode is spectrally well aligned with the mirror parameters. For the excitation, a few attempts were performed with the 407 nm cw laser of the μ-PL setup. This results in a fast degradation of the organic layer, which becomes apparent as black spots in the monitoring system. Due to the very small focus of the pump beam ($\varnothing \lessapprox 5\mu$m) and the absence of cooling and a protective athmosphere, a continuous wave excitation poses a too high permanent stress. Although the use of a cryostat could provide protection of the sample, it would be at the expense of manipulation flexibility and optical resolution. Instead, only pulsed sources are applied for the excitation, e.g. the 532 nm frequency-doubled Nd:YAG or the fs-system at 400 nm. To measure the input-output response of the system, the incident beam is attenuated with neutral density filters. From the measured signal, either the maxima or FWHM - integrated values are taken, which practically give the same results.

Figure 5.10 presents the integrated emission spectrum upon homogenous excitation below and above the lasing threshold of a photonic box. For the excitation, the 532 nm laser directly pumps the DCM. The observed discrete lines have similar intensities and linewidths for the low pumping energy, which changes in the second spectrum. Here, the fundamental mode has a signal approximately an order of magnitude higher than the residual lines. A further indication that lasing occurs is the reduced linewidth of this mode. In comparison to the spectral response of an unstructured microcavity, the difference between both emission regimes is less distinct, which is due to the fact that the spontaneous emission is already concentrated to a few lines. Additionally, the high quality factor of the box causes a good confinement, thus narrow emission lines.

The full input-output curve of this box is shown in figure 5.11, where the signal amplitudes are plotted in log-log scale along the pump energy. As a guide to the eye, lines with a slope of unity (which corresponds to the extremes of spontaneous and stimulated emission) are fitted to the data. The relative distance between these lines, which corresponds to the β-factor is close to 10^{-1}, which is at least 1-2 orders above the typical values of unstructured microcavities. Values up to 0.15 were measured in other samples, which shows the potential of the lateral confinement. The high β is a direct consequence of the altered mode density and thus the stronger relative emission of the excited molecules to a certain mode. Additionally to the intensities, the progression of the halfwidth of the emission line is shown. In the region of the threshold, the FWHM drops from 0.65 nm to 0.2 nm and remains at this value. The transition is not as pronounced as for a planar organic microcavity system, but shows a smooth decrease. This effect can again be attributed to the three-dimensional confinement, which leads to a high fraction of the box molecules to emit already into the respective

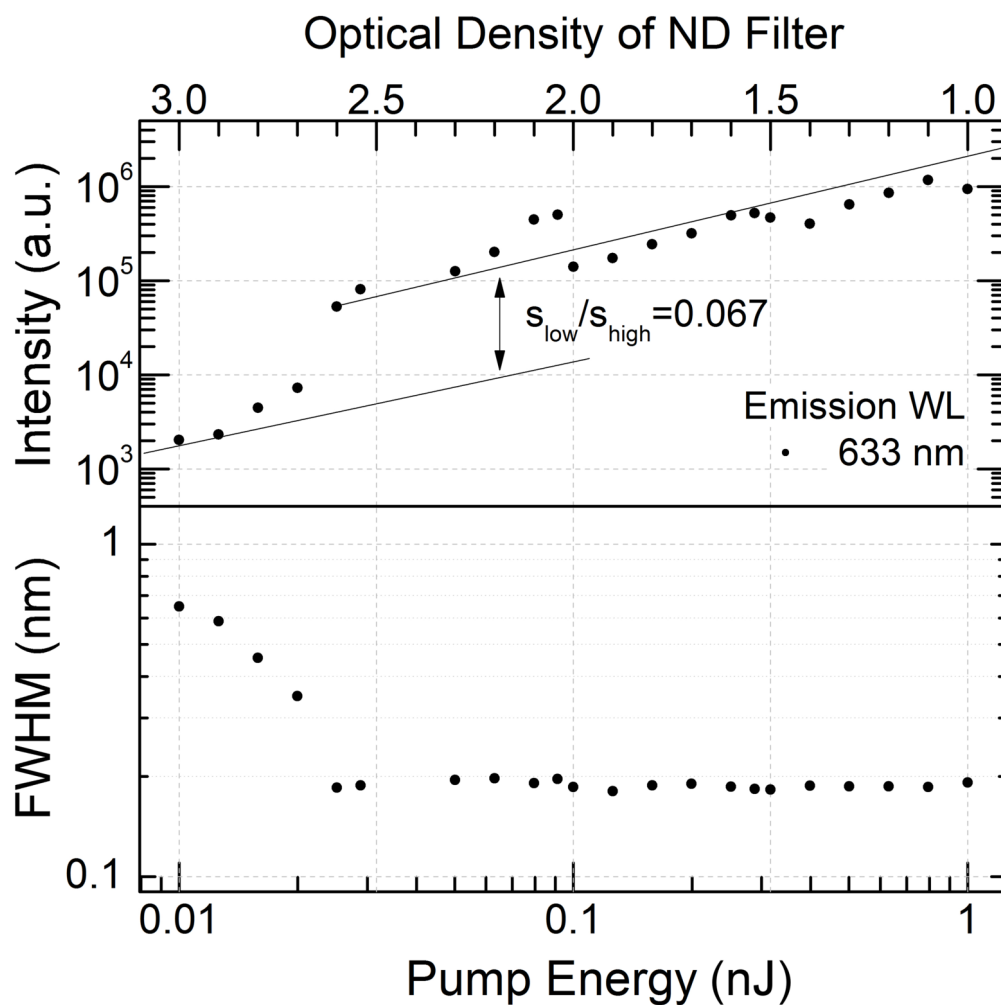**Figure 5.11:** Input-output data of the photonic box, indicating the transition from spontaneous to stimulated emission at $\approx 25\,\text{pJ}$. Additionally, the determined FWHM values are plotted, which show a remarkable drop beyond the threshold.

mode at moderate excitation energies.

Regarding the increase of intensity in the lasing regime, no drop of intensity becomes apparent. This is in so far not self-evident, as the ambient measurement conditions with at least some 1000 pulses per data point yields a large stress to the small structure. Nevertheless, lasing can be observed for over two orders of magnitude. In this context it is helpful for the stability of the system, that the direct excitation of DCM at 532 nm is used. Reminding the considerations of section 5.1.3, the excitation of Alq_3 at ≈ 400 nm with subsequent Förster-transfer has a lower overall quantum efficiency, which together with the increasing absorption coefficients of the mirror layers results in a higher fraction of absorbed photons, which do not contribute to the lasing process.

The response of the residual modes to higher pumping energies is discussed in the next section followed by the characterization of samples, where the active region is not excited homogenously.

5.2.2   Simultaneous emission of multiple lasing lines

When an unstructured planar microcavity is pumped in one spot, only a single laser mode (at the cutoff frequency) arises, which is emitted perpendicular (under certain conditions additionally as a cone - see [92]). In the preceding section, the lasing of the ground mode of the photonic box was described. One might expect that the limited amount of invertable emitters in this structure together with the overlap of the particular mode distributions prevents any other emission line to overcome a lasing threshold, besides the favored fundamental one.

Nevertheless, in the experiment with a homogeneously excited box, higher order lines show stimulated emission at a certain pump energy, without a visible mode competition effect. Figure 5.12 shows the laterally resolved spectrum of a photonic box at three different pumping energies covering three orders of magnitude. The respective intensity distribution of 4 groups of modes is visible, which have at 20 pJ pumping a comparable emission intensity, with ground and second group being more pronounced. The step to 100 pJ in combination with the changed magnification factor would result in a halving of the intensity, if still the linear regime of spontaneous emission is present. This roughly applies for the higher order modes, whereas the fundamental mode increases, which indicates at least the transition to the stimulated emission regime. Using the same argumentation for the last spectrum (c), lasing can be observed from all 4 groups of modes. The appearance of two maxima for the higher order modes results in an oblique emission of the respective photons (compare relation between near and far field in section 4.2.1). Thus, the box emits simultaneously at various wavelengths and into different directions.

The input-output curves (figure 5.13) of the modes provide a more accurate proof
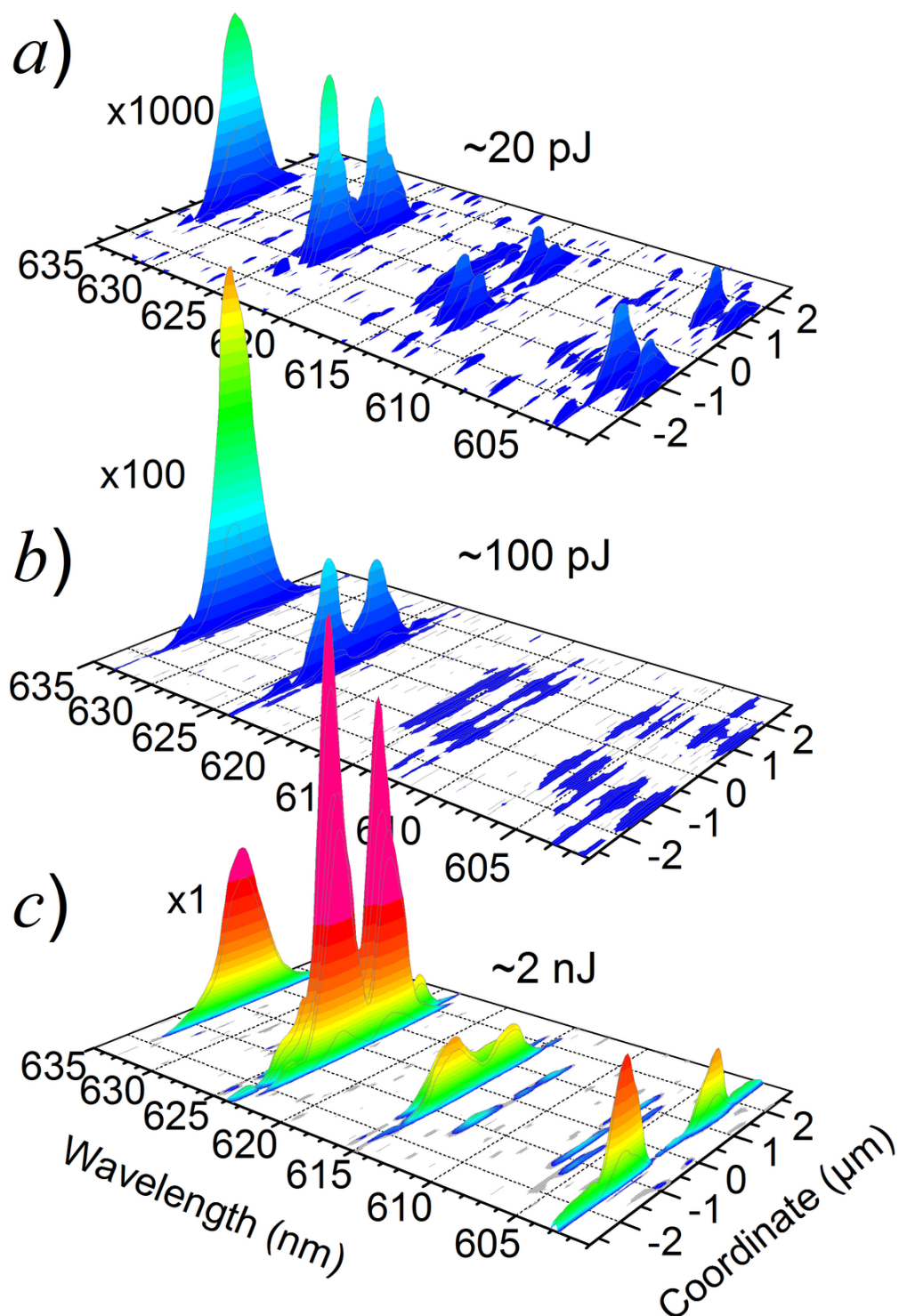
Figure 5.12: Intensity distribution measured in near field configuration for three different pumping energies. (a) For the low pumping, all lines emit spontaneously. (b) The fundamental mode is in the lasing regime for moderate excitation. At high incidence power (c), lasing can be observed for multiple modes even at higher order.
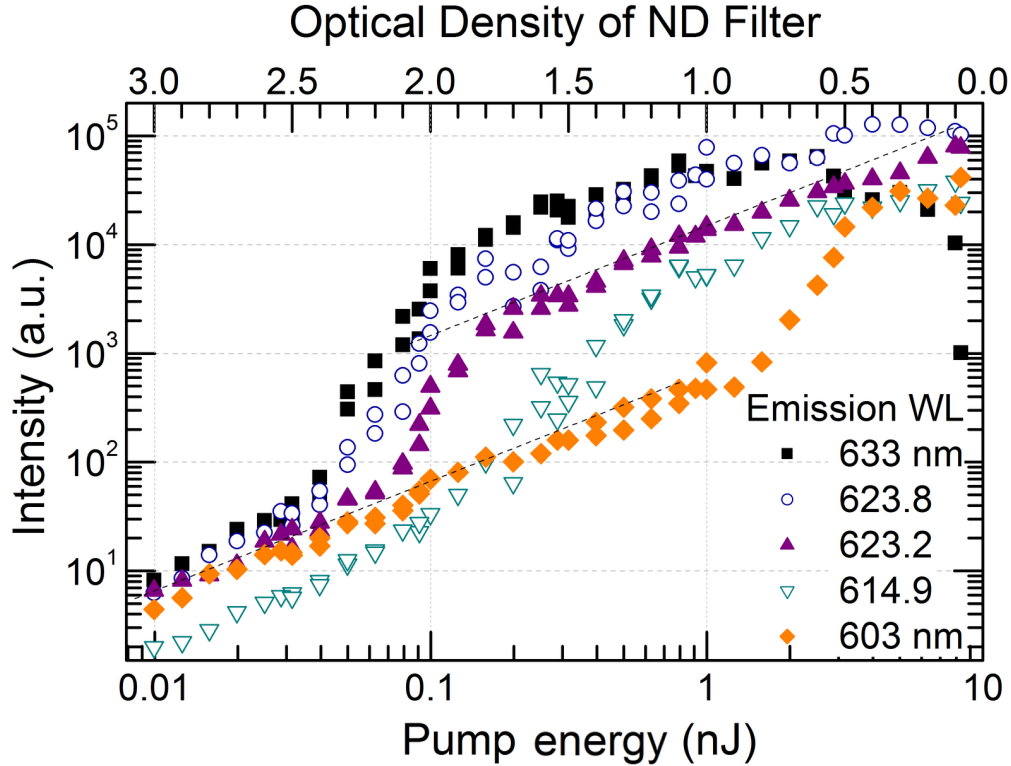
Figure 5.13: Input-output data for the lines of figure 5.12, which show lasing. Apparently, the coupling factor β is in the same range for the different wavelengths, whereas the threshold level increases, the more the emission shifts away from the gain and reflectance maximum.

that these lines exhibit laser emission. Starting from $\approx 50\,\mathrm{pJ}$, the fundamental mode gets into the transition region, closely followed by the set of two modes around $623.5\,\mathrm{nm}$. The two modes emitting at even higher energy overcome their threshold at much higher pumping energies, as summarized in table 5.1.

From these values follows the already expected result that the increasing distance from the gain maximum of the emitter system $\mathrm{Alq_3{:}DCM}$ at $\approx 630\,\mathrm{nm}$ [34] requires more energy to invert the system. Since the fundamental and the second group of modes have a similar gain coefficient, their threshold does not vary much. In a box with ideally reflecting side walls, any mode would have a similar enhanced transition rate (except for degeneracy), thus none would be preferred for starting the lasing process. The spectral properties of the emitter and reflector leads to the observed ordering of the stimulated emission. Furthermore, the modes of higher order have their maxima closer to the edges of the box, which results in a stronger influence of imperfections of the side walls onto the emission properties.

Regarding the specific coupling factors of the lines, they are all in the range of $10^{-2} - 10^{-1}$. Surprisingly, the higher order modes seem to have a noticeably higher coupling of emission into the laser mode. Away from the stop band maximum of the mirrors, one would expect a different behaviour. An explanation of this effect might

Wavelength (nm)	P_{thr} (nJ)	β-factor
633	0.04	$3.0 \cdot 10^{-2}$
623.8	0.05	$4.8 \cdot 10^{-2}$
623.2	0.07	$1.1 \cdot 10^{-1}$
614.9	0.22	$9.8 \cdot 10^{-2}$
603	1.25	$8.5 \cdot 10^{-2}$

Table 5.1: Estimated values of the threshold and coupling factor β for the lasing lines of figure 5.13

be that the reflections in lateral directions (ideally total internal reflection) are more efficient than in vertical direction. As the lateral component of the wave vector becomes larger with increasing mode number, the confinement and thus the β-factor increases, if the reflectivity of the dielectric mirrors would stay constant. Besides the various mentioned parameters, which influence the threshold of the box modes, the role of the excitation condition was not yet regarded. For the majority of lasing experiments, the beam was focussed to a size which allowed a homogenous excitation. In the following section, experimental results are presented where a smaller beam waist leads to a spatially inhomogenous inversion.

5.2.3   Selective stimulated emission

The so far discussed mode distribution in the photonic boxes upon homogenous excitation or transmission can be approximated by a product of *cosine* and *sine* functions, with nodes at the sidewalls. One can argue that the emitters interact more strongly with the electric field when located in the antinode of the specific mode, compared to emitters in free space, due to the confinement. Therefore, an impact on the stimulated emission behaviour of such a structure can be expected, when the excitation region is decreased such that the pump beam overlaps only with the antinode position of a set of specific modes. In particular, for the confined region of $5 \times 5 \, \mu m^2$ size, a micronsized excitation spot focussed into the center will pump effectively the ground mode and higher modes with antinodes in the center. Contrary, a shift of the spot towards an edge may lead to predominant excitation of modes with nodes in the center of the structure. An indication of such a process was shown in 2008 by Bajoni et al. [93]. The group demonstrated experimentally that the change of the spatial excitation symmetry can trigger polariton lasing between the ground and two excited confined modes in a cylindrical pillar cavity containing semiconductor quantum dots. It will be shown in the following, that an equivalent experiment can also succeed in organic photonic boxes. Therefore spatially controlled stimulated emission at various wavelengths and spatial as well as angular distributions in organic photonic dots is induced. At this, one benefits from the fact, that these systems intrinsically allow laser emission from

various modes (see previous section). The experimentally observed spectra are compared to the results of a numerical model, which includes absorptive and gain regions in a waveguide.

The sample is mounted on the micrometer translation stage and is excited with the Nd:YAG laser (532 nm, 1.5 ns, 2 kHz). The confocal microscope setup is in the far field configuration and the beam diameter in focus is decreased to a size of $\approx 2\,\mu$m. For the experiment, the sample is carefully shifted such that the excitation spot is positioned at three different locations within the dot structure. In the first case, it coincides with the center of the structure, whereas for the second experiment, it is moved to an edge and finally, the photonic dot is excited in one of its corners (see sketches at Fig. 5.14 (a)-(c)). The intensity of the pump beam is increased up to the point where one of the modes switches from spontaneous emission to lasing, which appears for all three excitations spots at a similar level.

Figure 5.14 (a) depicts the case when the excitation spot is located at the center of the photonic dot. Spontaneous emission from several discrete modes is visible between 642 and 620 nm, following the parabolic dispersion curve. Thereof, the ground mode at 641.5 nm shows lasing, as well as the mode at 638 nm. When the beam excites an edge of the structure, the lasing process starts only for a mode of the second group, spectrally located at 637.5 nm (see Fig. 5.14 (b)). For the last spectrum (Fig. 5.14 (c)), the incident beam is shifted towards a corner of the dot. Again, the lasing of the ground mode is missing, although it has a higher intensity than the rest of the spectrum. The lasing of the second mode is now even more pronounced, so we can better see the extension of the emission in k-space.

For the simulation of these results, a numerical software [16] using a Finite-Difference algorithm is applied. The organic post is approximated by a lossy rectangular waveguide, which is surrounded by air. The lateral size is chosen accordingly to the dimensions of the photonic dot ($5 \times 5\,\mu$m^2) while losses $\gamma \approx (1-R)/2L_c$ are determined by the reflectivity R of the DBRs and the cavity length L_c. Additional losses due to reabsorption on the lasing mode wavelength λ_m can be characterized by a background absorption coefficient $\alpha(\lambda_m)$. In this case [94], the reflection R should be substituted by the product $R^\alpha = \exp(-\alpha L_c) \cdot R$. Due to the single path transmission factor $\exp(-\alpha L_c)$, the component R^α can be (much) smaller than R in an absorptive cavity layer or approaches 100% in an inverted layer.

As a reasonable value, the loss γ is set as $3{\cdot}10^{-3}$ for the whole waveguide, corresponding to a mirror reflectivity of 99.9%. The refractive index is chosen as $n_{org} = 1.75$, which fits best for Alq$_3$ within the desired wavelength range. To simulate the effect of inversion in an excited area of the structure, a gain component g is added in this local region. In the simulation, it is realized by an overlaid negative absorption, which

---

[16] RSoft Design Passive Device Suite
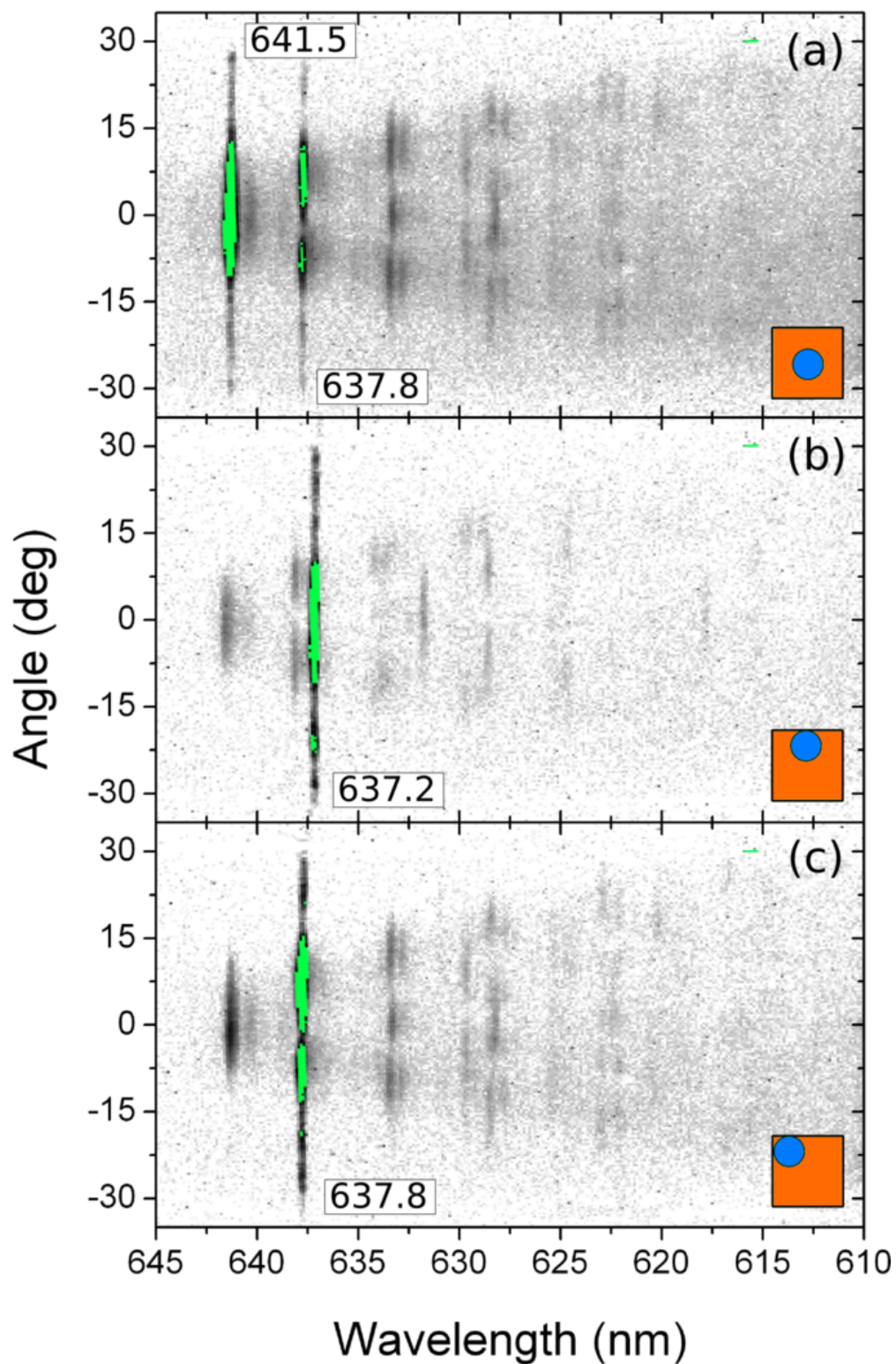
Figure 5.14: Far field spectra of a $5\,\mu$m photonic box, excited with a $\approx2\,\mu$m excitation spot at (a) the center, (b) the edge and (c) the corner. Depending on the position, the fundamental mode, or another mode of higher order starts lasing first.
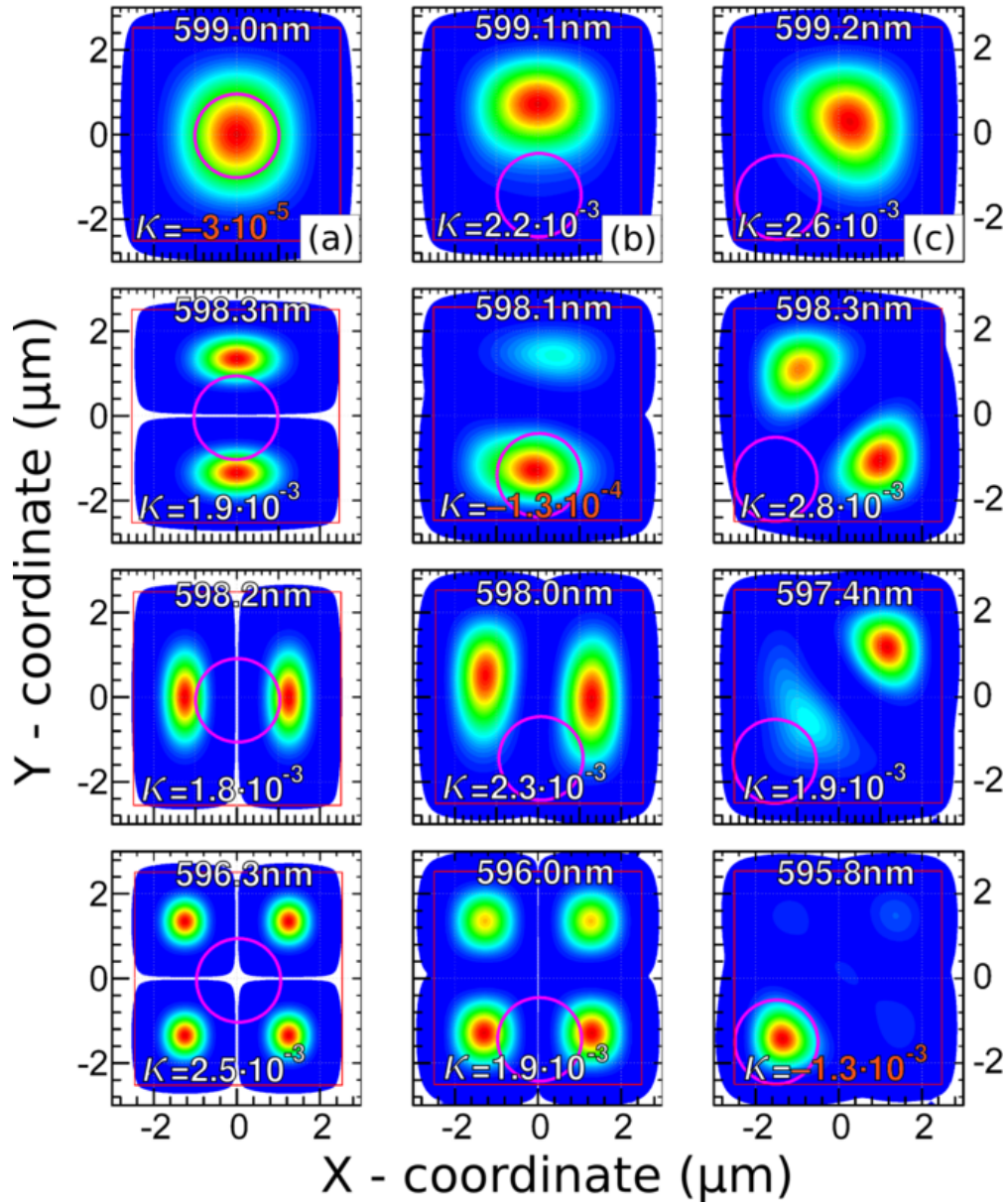
Figure 5.15: Simulated intensity distribution for the lowest modes of a waveguide with constant absorption ($\gamma = 3 \cdot 10^{-3}$) and a spatially distributed gain (pink circle), exceeding the loss (g up to $1.1 \cdot 10^{-2}$). Indicated are the calculated spectral mode positions λ as well as a net loss (positive κ) or net gain (negative κ).

Figure 5.16: Variation of the ground mode wavelength and the net absorption in the lossy guide with a central gain area of $2\,\mu$m diameter and an increasing numerical value for g. Whereas the net absorption decreases linearly, deceeding the value of zero and thus approaching the region of total negative loss, the modes energy shifts to higher energies due to the modified field profile.

shall compensate the losses in the excited region. The dimension and shape is matched to the experimental gaussian beam of $2\,\mu$m diameter, thus it is a cylinder within the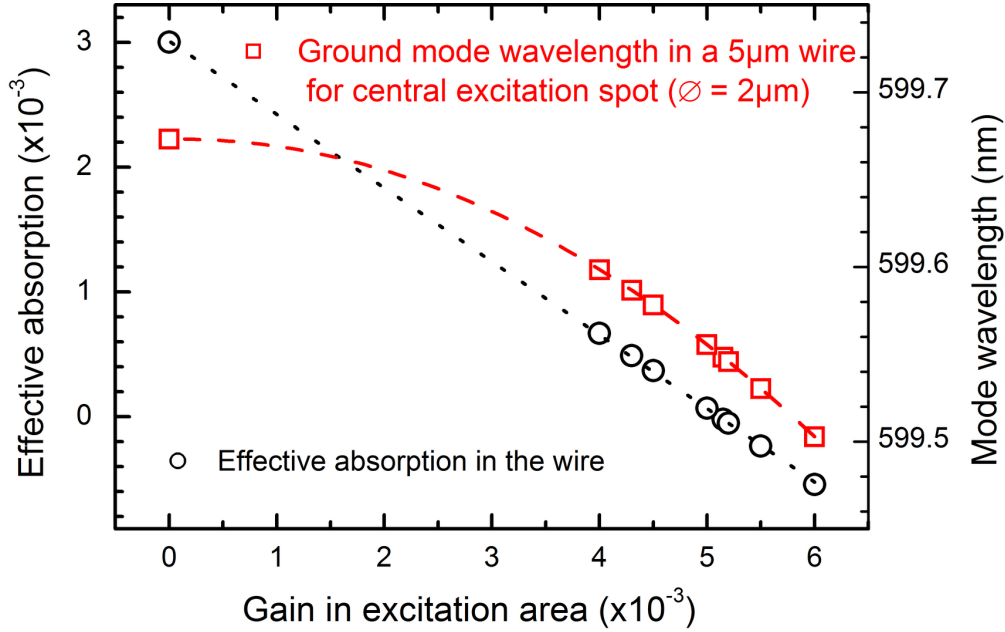 waveguide which has a gaussian gain profile. By the variation of the amount of negative absorption, one can either realize a lower loss, lossless, or gain region.

For the three considered cases, the value is chosen accordingly, and the lowest resonant modes of the waveguide (see Fig. 5.15) are calculated. Beside the modal wavelength, this gives a number for the net absorption κ the mode experiences during propagation. When these values are compared for different modes, one either has a positive number (meaning losses during propagation of the mode) or a negative number (which corresponds to gain). The latter one should be, in this simplified picture, favored to show laser emission. This is the ground mode for central excitation (Fig. 5.15 (a)), the second mode for edge excitation (Fig. 5.15 (b)) and the forth mode for corner excitation (Fig. 5.15 (c)). The inhomogenous distribution of gain leads furthermore to a deformed distribution of the electric field, which can be seen in the intensity distribution. For modes with negative net absorption, one has an enhancement, whereas for lossy modes a displacement or suppression of the antinodes is present. This effect finally shifts the resonant wavelengths, which can explain why the lasing mode of spectrum 1 (b) could not be observed at central excitation (spectrum 1 (a)).

The shift of the fundamental mode wavelength in case of central excitation for different gain values is depicted in figure 5.16. The reduction of losses leads to a

concentration of the field in the center, which acts as a kind of additional gain guiding. The values can be fitted well with a polynomial of second order, which effectively means that the higher the applied gain, the stronger the deviation from the fundamental mode frequency given by the geometry will be. In reality, this is limited by the number of invertable molecules. Additionally to the fundamental mode wavelength, the effective absorption values are shown. They follow a linear trend and cross the zero-line at nearly twice the value of loss γ. Below this point, a propagating wave will be attenuated, above it shall be amplified, i.e. the structure exhibits lasing. The variation of the modal wavelength is an issue, which needs to be considered, in case of small size excitation spots, e.g. for the design of the resonator.

5.3 Lasing performance at a metallic interface

A challenging task to take the next step towards an electrical pumping of organic micro-cavity lasers is the integration of contacts. One of the issues is an equivalent excitation density of several $100\,\mathrm{A/cm^2}$ to overcome the threshold [95], which may exceed stability limits of the dye and introduces additional losses due to interaction with charge carriers or excited state absorption, which inhibits any lasing [96]. Another issue are optically induced effects, such as modifications of the mode structure and confinement due to an altered local material composition [97,98] or the creation and interaction with optical surface states at metal interfaces. The growing interest in polariton systems during the last years and their possible applications yielded theoretical and experimental results, e.g. on so-called optical Tamm states [99–101] or strong coupling between surface plasmons and excitons [102]. It is thus reasonable to expect an influence on the lasing performance when the inversion is created close to metal layers. Retaining the vertical resonator design, it is practically impossible to apply flat contacts on bottom and top of the emissive layer, analogous to a diode design and achieve lasing. When the thin metal layers are placed in the node region of the electric field in the center of the resonator, the interaction could be decreased, but the large number of roundtrips amplifies even the smallest losses to considerable amounts. By integrating the contacts in the resonator but separating them from the zone of inversion, one could realize a device with good electrical properties, which may further benefit from the confining properties of the low refractive layers.

To investigate this, samples are prepared with 21 layer symmetric mirror microcavities, designed for $630\,\mathrm{nm}$, and a wedge shaped $\lambda/2$ layer (100% thickness gradient) of Alq$_3$:DCM (2wt%). The metal interface is realized by covering the central part with a polymer film (Opticlean solution) which is directly applied on the bottom mirror. Then, the material is deposited via electron beam evaporation (2-7 Å/s). Before the organic compound is deposited subsequently, the film is removed, leaving sharp

edges. The thickness is either 10 nm or 50 nm, and the chosen materials are silver and aluminium.

The measurement is performed in the micro-photoluminescence setup and the excitation is realized with the 512 nm Nd:YAG laser. Besides spatially resolved spectra, the input-output curve is determined at different positions, controlled with the micrometer translation stage and supervised in the monitoring system. The focussed beam (diameter $\approx 2\mu$m) is at first directed to the central part with no metal nearby, to have a reference. In the following, a position at $2.5\,\mu$m into the direction of the metal, directly at the interface ($0\,\mu$m) and $2.5\,\mu$m away, into the uncovered cavity direction (see figure 5.17(a)+(b)) is set. While scanning the samples, only the microcavities containing the aluminium stripes show lasing. As all processing steps, besides the metal evaporation, were performed in the same run, the removal of the polymer film after metal deposition might lead to non-reproducible results. Very recent experiments in the work group with a different polymer masking and following silver deposition yielded samples, which nicely show stimulated emission (to be published).
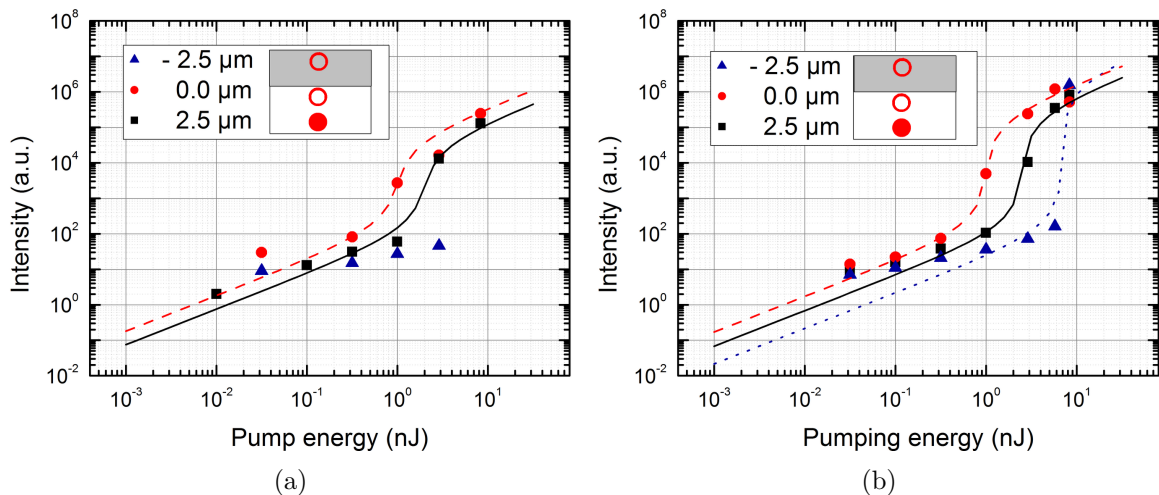
Figure 5.17: (a) Input-output measurement performed at the edge of an aluminium stripe of 50 nm height, integrated in a $\lambda/2$-thick Alq$_3$:DCM - cavity. Indicated are the respective positions of the excitation beam, and the data points are fitted with the standard rate equation model. (b) The same experiment for a 10 nm thick film. Differently, at the position within the metal, lasing was achieved, although at higher threshold.

At the position $2.5\,\mu$m away from the metal, stimulated emission is observed with similar performance compared to the center of the microcavity. The onset at ≈ 1 nJ is within the typical range and thus shows no negative effect of the close metal interface. The shift into the aluminium layer slightly reduces the threshold first ($0\,\mu$m) and then leads to a suppression of the light emission. This is ascribed to the high loss of aluminium at the design wavelength of 630 nm ($\kappa = 7.27$) and the lower refractive index (n = 1.325). Interestingly, in figure 5.17(b), the last data point indicates, that stim-

ulated emission is present even within the aluminium layer. A subsequent check with the monitoring system shows a hole in the metal layer. Obviously, the applied energy density is high enough to burn the 10 nm thick aluminium stripe, but surprisingly, this process is not very harmful for the organic cavity.

To simulate the structure, again the concept of the extension of the cavity layer to a waveguide is applied. A 2D model is created, which left of the center $(0 \, \mu m)$ consists of alternating layers of aluminium of different height (10 and 50 nm) and a $\lambda/2$ thick stripe, matching the organic material (n=1.75, $\kappa=1 \cdot 10^{-3}$). Right to the center, the waveguide is defined as a channel of organic material of the length equal $\lambda/2$ times the number of roundtrips. To reduce memory assumption and simulation time, an equivalent of Q=25 is chosen, which for the given materials provide reasonable results. The excitation is realized with a $2 \, \mu m$ wide channel of variable negative absorption and horizontal position. For each position, thickness of the aluminium, and negative absorption, the fundamental mode is calculated, and the numbers of refractive index and total absorption are evaluated.
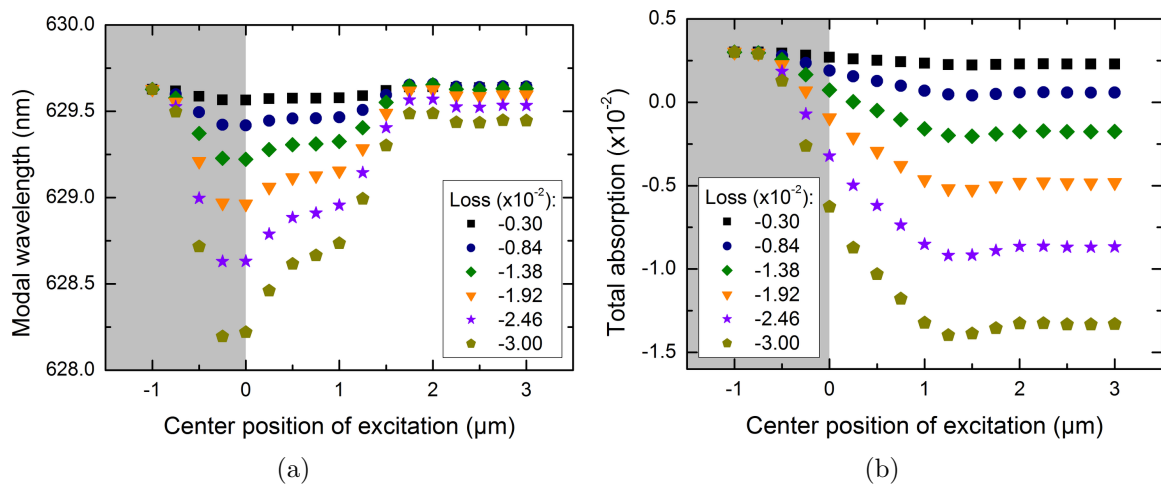
Figure 5.18: (a) Simulation results for the wavelength of the fundamental mode in a guide, partially consisting of 10 nm thick aluminium stripes at $\lambda/2$ distance (left of $0 \, \mu m$). The excitation region (width = $2 \, \mu m$) is varied in values of gain and position. (b) Total absorption, which the mode experiences as function of spatial position and gain of the center of the excitation region. At a certain gain level, the total absorption of the mode changes from positive to negative when approaching the uncovered part of the guide.

The progression of the fundamental mode wavelength (see figure 5.18(a)) is a bit complicated, but shows in principle the effect of mode confinement due to the excitation region. With increasing gain, the lateral focus of the mode is enhanced, thus the wavelength is blue-shifted. Furthermore, when the center of the excitation region is located at the interface, the energy of the resonance increases remarkably. This indicates a better concentration of the field, when just a part of the excitation region

Figure 5.19: Difference of the negative absorption value of the fundamental TM mode for the spatial position of the excitation center x $\approx 1.5\,\mu$m and x $= 2.25\,\mu$m. The curves are obtained for 10 nm thickness of three typical contact materials aluminium, silver, and gold.

lies within the organic waveguide, whereas the residual part is in the highly absorptive metal region.

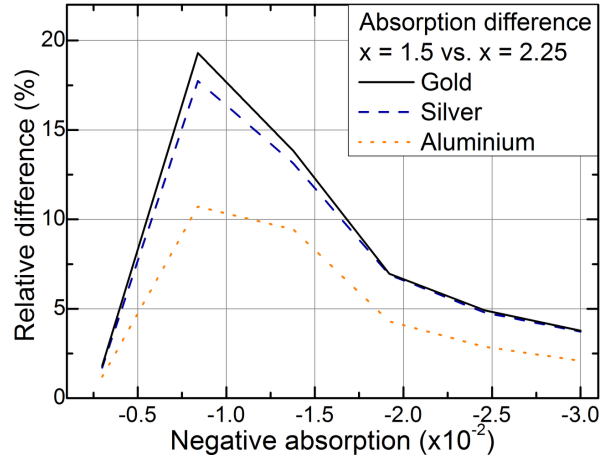In figure 5.18(b), the absorption of the fundamental mode is plotted for various levels of overlaid gain in the excitation region, starting from a value, which compensates the loss of the organic channel up to 10 times this number. Furthermore, the position of the center of the excitation region is shifted from -1 μm to 3 μm. As expected, the high loss of the metal stripes cannot be annihilated by the applied gain, thus the overall loss remains at the same positive value, when the excitation beam is within this region. When approaching the interface, half of the gain region is within the absorptive metal part, the other half in the solely organic part. Whereas the left fraction of the initial source is damped, the right one can be enhanced which leads in sum to a negative absorption for sufficiently high applied gain. A further movement to the uncovered part of the guide leads to an increase of total negative absorption approaching a constant value above 2 μm. Although one expects a continuous decrease to the metal-free value, a minimum appears at a center position of $\approx$1.5 μm, which corresponds to an optical path of 1-2 wavelengths at the chosen excitation. This value slightly depends on the chosen metal, thickness and applied negative absorption (smaller for higher gain). The lower refractive index of the close metal stripes can provide a reasonable explaination. As a part of the propagating field is reflected at the repeated interface, the mode is guided better. It is thus not diffusing further into the direction of the metal stripes and experiences a lower loss in the organic material, compared to a position farther away from the metal. At 1 μm distance, refraction effects at the edges of the metal can deflect a part of the excitation and may prevent a similar effect.

The absorption difference between the position at $\approx$1.5 μm and 2.25 μm at TM polarization is shown in figure 5.19 for the chosen values of gain in the excitation

region. Three of the typical electrode materials are investigated, which are aluminium, silver (n=0.13, κ=3.78), and gold (n=0.63, κ=3.12). Independently of the metal, the difference decreases with increasing gain, which indicates the better confinement of the respective mode in the excitation channel. Thus, the optical influence of the close metal stripes for x≈1.5μm becomes less important. This can also explain the low difference for the smallest gain value. Here, the channel is effectively transparent, as the gain compensates the loss of the organic material. Since the travelling wave is not amplified, a perpendicular propagation decays much faster compared to the higher gain cases. Thus, the positive confinement effect of the metal layer is less pronounced.

Comparing the various materials, it becomes apparent that the largest relative difference is observed for gold, followed by aluminium and silver. The order of the refractive index values can explain this effect for the most part, as the values of gold and silver are much lower than the one of aluminium. A larger amount of light of the mode is reflected at the interface and thus the additional confinement is more pronounced. Light which nevertheless penetrates into the metal is absorbed strongest in aluminium, followed by silver and gold. This could lead to the sequence of the curves as a result of both values. The simulation results for the larger thickness of the metal layers give similar results. The relative difference values increase in the low gain region (up to 1.6 times), but return to the same amount above a negative absorption of ≈ 1.5×10^{-2}. This again indicates the vanishing influence of the confinement effect at low refractive layers for a highly inverted region. In summary, it is shown, that the high absorption of metals is not a hindering factor for the creation of solid state dye lasers, as it is often accompanied with a low refractive index. This can lead to a waveguiding effect for a proper sample design and pumping condition, resulting in reduced losses in the excitation region.

6 Conclusion and outlook

Within the present work, various optical experiments on laterally modified organic microcavity systems are presented, including investigations of their passive transmission behaviour. Primarily, the effect of an in-plane structuring on the parameters of spontaneous and stimulated emission is considered. Therefore, three kinds of samples are investigated, namely height- and concentration-wedged planar microcavities, three-dimensionally confined photonic boxes and resonator structures with incorporated metal layers. The essence of the results is outlined in the following:

- laterally structured OVCSELs can eliminate drawbacks (e.g. in-plane losses, short gain length) of the vertical design for the most part

- a horizontal extension of about $5\,\mu$m experimentally appears as optimum, regarding the optical improvements of the system and simplicity of fabrication and investigation

- highly absorptive metal layers do not inevitably increase the losses of organic lasers, but may confine light and thus lower the laser threshold

- selected microcavity designs provide a useful tool for polarization-related physics and its later application

It is shown in a microcavity with a continously variable resonator thickness that the polarization-dependent penetration depth of the electric field into dielectric mirrors induces a splitting of the resonant mode for oblique observation angles θ. The spectral distance Δ_θ between the cross-polarized states increases, as the shift between the design wavelength λ_D of the mirrors and the resonant wavelength λ_C of the cavity grows. Whereas for small variations, the values can be approximated by an analytical formula [28], the large experimental splitting for high detunings ($\Delta_{30°} > 10\,$nm close to the edge of the stop band) deviates from the linear growth. A numerical treatment with the transfer matrix algorithm provides in this case a better agreement. The observed effect is an intrinsic property of the dielectric mirrors and could be used in passive (empty) cavities for a wavelength and polarization filtering, or with a suitable emitter

for the generation of a THz modulated signal [37] covering a wide range of frequencies (up to 14×10^{12}Hz).

When the cavity layer is structured on the micron scale, the modified spatial boundary conditions influence the density of electromagnetic states and thus the allowed modes. Instead of a single resonance (neglecting polarization splitting) of the planar $\lambda/2$ microcavity, a complex mode picture arises. The finite lateral extension of the resonator leads to a discrete set of states at non-equidistant energy steps. With the help of a micro-photoluminescence setup, the local intensity distribution of the electric field and the far field emission profile is monitored with very high precision. For the simulation of the states, a scalar box model with fully reflective ($R = 1$) sidewalls is used. This gives a good agreement with the experiment and explains the emission lines at small detection angles for higher order modes as interference effect of a patterned source. Another feature of modes with higher mode number is the appearance of doublets with increasing spectral distance. This effect is attributed to a polarization splitting of the states which occurs despite the match of cavity mode and design wavelength. As an approach to this problem, numerical waveguide simulations, including the vectorial field information are performed instead of the analytical model. Whereas the so obtained local intensity profiles are similar to the scalar approach, the different phase shifts upon reflection at the sidewalls lead to an energetic shift between the states of different polarizations, as observed in the experiment.

It is shown in chapter 5 that the stimulated emission of a planar organic microcavity is mainly concentrated in the apex of the far field dispersion parabola, with a slight but visible divergence originating from the small active mode volume. The input-output curves verify that stimulated emission occurs for the $\lambda/2$ layer of Alq$_3$:DCM even away from the gain maximum with adequate performance (coupling factor $\beta \sim 10^{-3}$, I$_{thr} \sim 15\,\mu$J/cm^2). Upon a variation of the DCM amount in the emission layer, while retaining the residual resonator parameters, the lasing threshold shows a minimum for a concentration of approximately 2.5wt% when the indirect pumping scheme via Alq$_3$ is used. This originates from the interplay of the separation-dependent Förster resonant energy transfer and the increasing absorption tail of the DCM molecules for higher concentrations. Pumping the fluorescent molecules directly, the threshold minimum disappears, but an asymptotic approach towards a constant intensity value in the stimulated emission regime occurs. Taking into account the limited number of emitter molecules contributing to the lasing and the short duration of the pump pulse by an additional rate equation, it is possible to model the input-output behaviour with good accuracy. The result also suggests that the shown planar organic microcavity system works already close to its intrinsic limits, since the emitter count in the small inverted region is facing a still high number of losses. Thus, it is straightforward to pursue the lateral confinement to have a fair chance of electrical excitation.

The stability of the presented microcavity systems has been analyzed in the following at various excitation levels with the focus on the degradation rate above the respective laser threshold of planar samples and photonic box systems. As the excited dye molecules are mostly fragile and reactive with oxygen and water, the typically chosen environmental conditions in the experiment could lead to major decomposition of the emission layer. Nevertheless, the stimulated emission continues after $> 10^6$ pulses even for pump energies two orders of magnitude above the lasing threshold. Analogous to kinetics observed in electrically driven OLEDs, the emission intensity reduction can be described with a fast and a slow time constant, which can be attributed to different degradation mechanisms. It could be worth to check the stability under different gas flows in order to isolate the primary reaction. An additional capping layer or the introduction of adsorbing substances might then increase the lifetime of the device.

In further experiments, the photonic boxes are analyzed for their stimulated emission capability. The lasing of a single mode is obtained at lower threshold energy, which is a consequence of the better confinement and limited mode volume. The lower number of possible emission channels is expressed by the high coupling factor β, reaching values up to 0.1. Different from planar $\lambda/2$ systems, the lasing process in three-dimensionally confined organic resonators is not restricted to a single state, but can be initiated for many modes simultaneously at multiple wavelengths and directions. These modes have comparable coupling factors and their respective threshold values monitor qualitatively the gain profile of Alq$_3$:DCM. An interesting effect occurs when the excitation of the box structure is spatially inhomogenous. In this case, the distribution of gain and loss regions supports the overcome of the lasing threshold for the modes which show the best overlap of their respective field profile. The effect can be modelled using a waveguide approach with a laterally restricted negative loss component. The so introduced additional gain guiding effect modifies the electric field of the modes and can thus shift the resonant wavelength.

Another type of optical confinement is shown in the last part of the thesis. Here, a thin areal metal layer is partially located underneath the organic cavity layer and the lasing performance is analyzed at its interface. Although highly absorptive, the threshold is slightly reduced at close distance to the metal in comparison to a region with pure dye layer. Numerical simulations show that the low refractive index of the potential electric contact leads to a weak confinement of the electric field additional to those provided by the locally restricted gain region. With increased pumping, the relative influence of this effect becomes less pronounced due to increased confinement of the field within the inverted region.

This thesis gives an insight into possible manipulations of the spectral behaviour and the lasing characteristics of organic microcavities by lateral structuring. Additionally, the effect of the inhomogenous distribution of gain in structured samples is shown.

The broad emission spectrum of the employed organic dyes of the cavity layer allows in this context a wide range of optical investigations under ambient conditions. A majority of the observed effects demonstrates the huge potential of a three-dimensional VCSEL resonator structure to be the basis of the electrically driven organic solid state laser. Nevertheless, some open questions are not adressed here and there is room for improvement of the system.

First to mention is the material choice. Although Alq$_3$:DCM is a widely used and efficient laser dye system with a good gain coefficient, the electrical conductivity is rather weak. New materials [45, 103, 104] can reduce the necessary power for inversion and thus lower the expected necessary current densities. The stability of the molecules is probably not the limiting factor for high currents [105], but the charge induced absorption increases. Another promising material class could be organic single crystals [106] with high charge carrier mobilities at good emission efficiency. Although predestined for lateral resonator structures, layers can be grown in predefined microcavity structures [107].

Regarding the dielectric mirrors, the material combination of TiO$_2$ and SiO$_2$ provides one of the highest reflection coefficients per layer pair within the visible range. Possible improvements can be achieved by the in-situ monitoring of the optical thickness of each layer directly on the sample, by which the fluctuation of the physical thickness and refractive index can be compensated. First tests show a better agreement of the experimental and simulated spectra of the mirrors and indicate a better performance of microcavity samples. Another method is the oblique angle deposition of oxide layers [108]. Due to the pillar like growth of the film, a tilting of the substrate leads to a self-shadowing, with the result of increasing spaces between the material. Thus, the refractive index n_{low} decreases towards unity, which can either be used to raise the difference Δn between the mirror pairs or to create transient layers. Whereas the first application increases the reflectivity and width of the stop band, the second one can be used for light outcoupling of otherwise guided mirror modes.

Further experimental effort is needed to understand the temporal behaviour of the investigated systems. It would be possible to measure an enhancement of the spontaneous emission rate in the box structures and derive the mode volume directly. Additionally, one could detect a coupling of the confined modes. For certain pump conditions, it is possible to suppress stimulated emission of one mode with the onset of lasing in another one. This mode competition is already a hint of the interplay between the states, which could be used with the corresponding phase relation for example for short pulse generation.

For an electrically contacted device, a fair chance of realization is existent, regarding the weak optical confinement effect at close distance. Here, a combination of three-dimensional micron-sized structuring, as already successfully shown in inorganic

semiconductors [21] and efficient electro-luminescent layer stacks inside a microcavity is under investigation. Samples with holes of different size in a metal layer show already a similar discretization of the spectrum and optically induced lasing at low threshold [109].

Bibliography

[1] D. Martin, "Theodore Maiman, who built the first laser, dies at 79," *The New York Times* , May 13 2007.

[2] T. Maiman, "Stimulated optical radiation in ruby," *Nature* **187**, 493–494, 1960.

[3] A. Javan, D. Herriott and W. Bennett, "Population inversion and continuous optical maser oscillation in a gas discharge containing a He-Ne mixture," *Phys. Rev. Lett.* **6**, 106, 1961.

[4] R. Hall, R. Carlson, T. Soltys, G. Fenner and J. Kingsley, "Coherent light emission from GaAs junctions," *Phys. Rev. Lett.* **9**, 366, 1962.

[5] P. Sorokin and J. Lankard, "Stimulated emission observed from an organic dye chloro-aluminum phthalocyanine," *IBM J. Res. Develop.* **10**, 162–&, 1966.

[6] F. Schäfer, W. Schmidt and J. Volze, "Organic dye solution laser," *Appl. Phys. Lett.* **9**, 306–&, 1966.

[7] M. Hentschel, R. Kienberger, C. Spielmann, G. Reider, N. Milosevic, T. Brabec, P. Corkum, U. Heinzmann, M. Drescher and F. Krausz, "Attosecond metrology," *Nature* **414**, 509–513, 2001.

[8] C. W. Tang and S. A. van Slyke, "Organic Electroluminescent Diodes," *Appl. Phys. Lett.* **51**, 913–915, 1987.

[9] N. Tessler, G. J. Denton and R. H. Friend, "Lasing from conjugated-polymer microcavities," *Nature* **382**, 695–697, 1996.

[10] S. Frolov, M. Shkunov, Z. Vardeny and K. Yoshino, "Ring microlasers from conducting polymers," *Phys. Rev. B* **56**, R4363–R4366, 1997.

[11] Y. Kawabe, C. Spiegelberg, A. Schulzgen, M. Nabor, B. Kippelen, E. Mash, P. Allemand, M. Kuwata-Gonokami, K. Takeda and N. Peyghambarian, "Whispering-gallery-mode microring laser using a conjugated polymer," *Appl. Phys. Lett.* **72**, 141–143, 1998.

[12] V. G. Kozlov, V. Bulović, P. E. Burrows, M. Baldo, V. B. Khalfin, G. Parthasarathy, S. R. Forrest, Y. You and M. E. Thompson, "Study of lasing action based on Förster energy transfer in optically pumped organic semiconductor thin films," *J. Appl. Phys.* **84**, 4096–4108, 1998.

[13] T. Granlund, M. Theander, M. Berggren, M. Andersson, A. Ruzeckas, V. Sundstrom, G. Bjork, M. Granstrom and O. Inganas, "A polythiophene microcavity laser," *Chem. Phys. Lett.* **288**, 879–884, 1998.

[14] C. Kallinger, M. Hilmer, A. Haugeneder, M. Perner, W. Spirkl, U. Lemmer, J. Feldmann, U. Scherf, K. Mullen, A. Gombert and V. Wittwer, "A flexible conjugated polymer laser," *Adv. Mat.* **10**, 920, 1998.

[15] M. Koschorreck, R. Gehlhaar, V. G. Lyssenko, M. Swoboda, M. Hoffmann and K. Leo, "Dynamics of a high-Q vertical cavity organic laser," *Appl. Phys. Lett.* **87**, 181108, 2005.

[16] I. D. W. Samuel and G. A. Turnbull, "Organic semiconductor lasers," *Chem.Rev.* **107**, 1272–1295, 2007.

[17] T. Tezuka, S. Nunoue, H. Yoshida and T. Noda, "Spontaneous emission enhancement in pillar-type microcavities," *Jpn. J. Appl. Phys. Pt. 2* **32**, L54–L57, 1993.

[18] J. M. Gérard, D. Barrier, J. Y. Marzin, R. Kuszelewicz, L. Manin, E. Costard, V. Thierry-Mieg and T. Rivera, "Quantum boxes as active probes for photonic microstructures: The pillar microcavity case," *Appl. Phys. Lett.* **69**, 449–451, 1996.

[19] B. Gayral, J. M. Gérard, B. Legrand, E. Costard and V. Thierry-Mieg, "Optical study of gaas/alas pillar microcavities with elliptical cross section," *Appl. Phys. Lett.* **72**, 1421–1423, 1998.

[20] A. Daraei, D. Sanvitto, J. A. Timpson, A. M. Fox, D. M. Whittaker, M. S. Skolnick, P. S. S. Guimaraes, H. Vinck, A. Tahraoui, P. W. Fry, S. L. Liew and M. Hopkinson, "Control of polarization and mode mapping of small volume high q micropillars," *J. of Appl. Phys.* **102**, 043105, 2007.

[21] S. Reitzenstein, T. Heindel, C. Kistner, A. Rahimi-Iman, C. Schneider, S. Hofling and A. Forchel, "Low threshold electrically pumped quantum dot-micropillar lasers," *Appl. Phys. Lett.* **93**, 061104, 2008.

[22] A. Adawi, A. Cadby, L. Connolly, W.-C. Hung, R. Dean, A. Tahraoui, A. Fox, A. Cullis, D. Sanvitto, M. Skolnick and D. Lidzey, "Spontaneous emission control

in micropillar cavities containing a fluorescent molecular dye," *Adv. Mater.* **18**, 742, 2006.

[23] E. M. Purcell, "Spontaneous emission probabilities at radio frequencies," *Phys. Rev.* **69**, 681, 1946.

[24] E. Hecht, *Optik*, Oldenbourg Verlag München Wien, 2005.

[25] P. Yeh, *Optical Waves in Layered Media*, John Wiley & Sons, Inc., Hoboken, New Jersey, 2005.

[26] D. Burak and R. Binder, "Cold-cavity vectorial eigenmodes of VCSEL's," *IEEE J. of Quant. Elect.* **33**, 1205, 1997.

[27] G. Panzarini, L. Andreani, A. Armitage, D. Baxter, M. Skolnick, J. Roberts, V. Astratov, M. Kaliteevski, A. Kavokin and M. Vladimirova, "Polariton dispersion and polarisation splitting for quantum well excitons in single and coupled microcavities," *Phys. Stat. Sol.. A* **164**, 91–94, 1997.

[28] G. Panzarini, L. C. Andreani, A. Armitage, D. Baxter, M. S. Skolnick, V. N. Astratov, J. S. Roberts, A. V. Kavokin, M. R. Vladimirova and M. A. Kaliteevski, "Exciton-light coupling in single and coupled semiconductor microcavities: Polariton dispersion and polarization splitting," *Phys. Rev. B* **59**, 5082–5089, 1999.

[29] S. Brorson, "Electromagnetic field mode density calculated via mode counting," in *Spontaneous emission and laser oscillation in microcavities*, H. Yokoyama and K. Ujihara, ed., ch. 5, 151 – 187, CRC Press, Boca Raton, 1995.

[30] D. Kleppner, "Inhibited spontaneous emission," *Phys. Rev. Lett.* **47**, 233–236, 1981.

[31] H. Yokoyama, "Spontaneous and stimulated emission in the microcavity laser," in *Spontaneous Emission and Laser Oscillation in Microcavities*, H. Yokoyama and K. Ujihara, ed., ch. 8, 275–310, CRC Press, Boca Raton, 1995.

[32] H. Yokoyama and S. D. Brorson, "Rate equation analysis of microcavity lasers," *J. of Appl. Phys.* **66**, 4801–4805, 1989.

[33] S. I. Hintschich, H. Gothe, V. G. Lyssenko, H. Fröb and K. Leo, "The effects of inhomogeneous broadening in an organic microcavity laser," *Opt. Quantum Electronics* **40**, 397–402, 2008.

[34] R. Brückner, "Untersuchung zur Anregung organischer Mikroresonatoren mit anorganischen Leuchtdioden," Diploma thesis, TU Dresden, 2009.

[35] S. Morimura and K. Ujihara, "Rate equation analysis of a microcavity laser with a finite number of molecules in the mode volume," *Jap. J. Appl. Phys.* **36**, 4307–4311, 1997.

[36] H. W. Lehmann and K. Frick, "Optimizing deposition parameters of electron beam evaporated TiO$_2$ films," *Appl. Opt.* **27**, 4920, 1988.

[37] R. Gehlhaar, *Terahertz oscillation and stimulated emission from planar microcavities.* PhD thesis, TU Dresden, 2007.

[38] H. K. Jang, S. W. Whangbo, H. B. Kim, K. Y. Im, Y. S. Lee, I. W. Lyo, C. N. Whang, G. Kim, H.-S. Lee and J. M. Lee, "Titanium oxide films on Si (100) deposited by electron-beam evaporation at 250°C," *J. Vac. Sci. Technol. A* **18**, 917, 2000.

[39] R. Linsbod, E. Ritter and K. Leitner, "Evaluation of the oxidation of TiO$_2$ films during reactive evaporation of Ti$_3$O$_5$ and during exposure of the films to the atmosphere," *Appl. Opt.* **42**, 4580, 2003.

[40] U. Schulz, S. Jakobs and N. Kaiser, "SiO$_2$ protective coatings on plastic optics deposited with plasma IAD," *Developments in Optical Component Coatings* **2776**, 169–174, SPIE, 1996.

[41] R. Thielsch, A. Gatto, J. Heber and N. Kaiser, "A comparative study of the UV optical and structural properties of SiO$_2$, Al$_2$O$_3$, and HfO$_2$ single layers deposited by reactive evaporation, ion-assisted deposition and plasma ion-assisted deposition," *Thin Solid Films* **410**, 86–93, 2002.

[42] P. R. Hammond, "Laser-dye DCM, its special properties, synthesis and comparison with other dyes in the red," *Opt. Comm.* **29**, 331–333, 1979.

[43] V. Bulović, V. G. Kozlov, V. B. Khalfin and S. R. Forrest, "Transform-limited, narrow-linewidth lasing action in organic semiconductor microcavities," *Science* **279**, 553, 1998.

[44] T. Förster, "Energiewanderung und Fluoreszenz," *Naturwissenschaften* **6**, 166, 1946.

[45] T. Aimono, Y. Kawamura, K. Goushi, H. Yamamoto, H. Sasabe and C. Adachi, "100% fluorescence efficiency of 4,4 '-bis[(n-carbazole)styryl]biphenyl in a solid film and the very low amplified spontaneous emission threshold," *Appl. Phys. Lett.* **86**, 2005.

[46] H. Nakanotani, C. Adachi, S. Watanabe and R. Katoh, "Spectrally narrow emission from organic films under continuous-wave excitation," *Appl. Phys. Lett.* **90**, 231109, 2007.

[47] D. Yokoyama, M. Moriwake and C. Adachi, "Spectrally narrow emissions at cutoff wavelength from edges of optically and electrically pumped anisotropic organic films," *J. of Appl. Phys.* **103**, 123104, 2008.

[48] E. K. Engel, *Ultrafast exciton relaxation in quasi-one-dimensional perylene derivatives.* PhD thesis, TU Dresden, 2005.

[49] M. Swoboda, "Time-resolved laser emission from organic microcavities," Diploma thesis, TU Dresden, 2006.

[50] T. Virgili, D. Lidzey, D. Bradley and S. Walker, "Cavity mode polarisation splitting in organic semiconductor microcavities," *Synthetic Metals* **116**, 497–500, 2001.

[51] A. A. Dukin, N. A. Feoktistov, V. G. Golubev, A. V. Medvedev, A. B. Pevtsov and A. V. Sel'kin, "Polarization splitting of optical resonant modes in a-Si:H/a-SiO$_x$:H microcavities,"*Phys. Rev. E* **67**, 046602, 2003.

[52] C. Y. Hu, H. Z. Zheng, J. D. Zhang, H. Zhang, F. H. Yang and Y. P. Zeng, "Mode splitting in photoluminescence spectra of a quantum-dot-embedded microcavity,"*Appl. Phys. Lett.* **82**, 665 – 667, 2003.

[53] L. Persano, E. Mele, R. Cingolani and D. Pisignano, "Polarization mode splitting in monolithic polymer microcavities," *Appl. Phys. Lett.* **87**, 031103, 2005.

[54] A. Camposeo, L. Persano, P. D. Carro, T. Virgili, R. Cingolani and D. Pisignano, "Polarization splitting in organic-based microcavities working in the strong coupling regime,"*Org. Electron.* **8**, 114 – 119, 2007.

[55] S. Stelitano, G. D. Luca, S. Savasta and S. Patané, "Polarized emission from high quality microcavity based on active organic layered domains," *Appl. Phys. Lett.* **93**, 193302, 2008.

[56] R. Gehlhaar, R. Schüppel, M. Koschorreck, T. Fritz, H. Fröb, M. Hoffmann, V. G. Lyssenko, K. Leo, L. Connolly, J. Wenus and D. G. Lidzey, "Time-resolved and cw photoluminescence from strongly-coupled organic microcavities,"*J. Lum.* **110**, 354–358, 2004.

[57] K. J. Vahala, "Optical microcavities,"*Nature* **424**, 839, 2003.

[58] A. Muller, C.-K. Shih, J. Ahn, D.Lu, D. Gazula and D. Deppe, "High Q (33000) all-epitaxial microcavity for quantum dot vertical-cavity surface-emitting lasers and quantum light sources," *Appl. Phys. Lett.* **88**, 031107–1, 2006.

[59] A. Baas, O. e. Daïf, M. Richard, J.-P. Brantut, G. Nardin, R. I. Kaitouni, T. Guillet, V. Savona, J. Staehli, F. Morier-Genoud and B. Deveaud, "Zero dimensional exciton-polaritons," *phys. stat.sol.* **243**, 2311, 2006.

[60] C. Constantin, E. Martinet, D. Oberli, E. Kapon, B. Gayral and J. Gérard, "Quantum wires in multidimensional microcavities: Effects of photon dimensionality on emission properties," *Phys. Rev. B* **66**, 165306, 2002.

[61] D. Sanvitto, A. Daraei, A. Tahraoui, M. Hopkinson, P. W. Fry, D. M. Whittaker and M. S. Skolnick, "Observation of ultrahigh quality factor in a semiconductor microcavity," *Appl. Phys. Lett.* **86**, 191109, 2005.

[62] H. Lohmeyer, K. Sebald, C. Kruse, R. Kröger, J. Gutowski, D. Hommel, J. Wiersig, N. Baer and F. Jahnke, "Confined optical modes in monolithic II-VI pillar microcavities," *Appl. Phys. Lett.* **88**, 051101–1, 2006.

[63] A. Kuther, M. Bayer, T. Gutbrod, A. Forchel, P. Knipp, T. Reinecke and R. Werner, "Confined optical modes in photonic wires," *Phys. Rev. B* **58**, 15744, 1998.

[64] T. Gutbrod, M. Bayer, A. Forchel, P. Knipp, T. Reinecke, A. Tartakovskii, V. Kulakovskii, N. Gippius and S. Tikhodeev, "Angle dependence of the spontaneous emission from confined optical modes in photonic dots," *Phys. Rev. B* **59**, 2223, 1999.

[65] J. M. Gérard, B. Sermage, B. Gayral, B. Legrand, E. Costard and V. Thierry-Mieg, "Enhanced spontaneous emission by quantum boxes in a monolithic optical microcavity," *Phys. Rev. Lett.* **81**, 1110–1113, 1998.

[66] M. Langner, R. Gehlhaar, C. Schriever, H. Fröb, V. G. Lyssenko and K. Leo, "Strong optical confinement and multimode emission of organic photonic dots," *Appl. Phys. Lett.* **91**, 181119, 2007.

[67] A. Kumar, K. Thyagarajan and A. Ghatak, "Analysis of rectangular-core dielectric waveguides - an accurate perturbation approach," *Opt. Lett.* **8**, 63–65, 1983.

[68] D. Wu, L. Wang, Y. Liu, S. Wang, Y. Ning, C. Jin, J. Zhao, X. Liu, S. Wu and X. He, "Photoluminescent properties of dye-doped poly(N-vinyleabzole) (PVK) in microcavity," *Thin Solid Films* **363**, 198–200, 2000.

[69] T. Virgili, D. G. Lidzey, M. Grell, D. D. C. Bradley, S. Stagira, M. Zavelani-Rossi and S. D. Silvestri, "Influence of the orientation of liquid crystalline poly(9,9-dioctylfluorene) on its lasing properties in planar microcavity," *Appl. Phys. Lett.* **80**, 4088–4090, 2002.

[70] X. Liu, D. Poitras, Y. Tao and C. Py, "Optically pumped lasing from organic microcavity," *Can. J. Phys.* **82**, 481, 2004.

[71] B. Schütte, H. Gothe, S. I. Hintschich, M. Sudzius, H. Fröb, V. G. Lyssenko and K. Leo, "Continuously tunable laser emission from a wedge-shaped organic microcavity," *Appl. Phys. Lett.* **92**, 163309, 2008.

[72] C. W. Tang, S. A. van Slyke and C. H. Chen, "Electroluminescence of doped organic thin films," *J. Appl. Phys.* **65**, 3610–3616, 1989.

[73] V. G. Kozlov, V. Bulovic, P. E. Burrows and S. R. Forrest, "Laser action in organic semiconductor waveguide and double-heterostructure devices," *Nature* **389**, 362–364, 1997.

[74] S. Riechel, U. Lemmer, J. Feldmann, T. Benstem, W. Kowalsky, U. Scherf, A. Gombert and V. Wittwer, "Laser modes in organic solid-state distributed feedback lasers," *Appl. Phys. B* **71**, 897–900, 2000.

[75] G. Y. Zhong, J. He, S. T. Zhang, Z. Xu, Z. H. Xiong, H. Z. Shi, X. M. Ding, W. Huang and X. Y. Hou, "In situ photoluminescence investigation of doped Alq," *Appl. Phys. Lett.* **80**, 4846–4848, 2002.

[76] J. Jakabovic, T. Wong, O. Lengyel, J. Kovac, C. Lee and S. Lee, "Optical properties investigations of organic Alq$_3$ layers doped by DCM," in *4th Int. Conf. on Adv. Sem. Dev. Micros.*, 35 – 38, 14-16 2002.

[77] A. D. Walser, I. Sokolik, R. Priestly and R. Dorsinville, "Dynamics of photoexcited states and charge carriers in organic thin films: Alq$_3$," *Appl. Phys. Lett.* **69**, 1677, 1996.

[78] G. Zhong, Z. Xu, J. He, S. Zhang, Y. Zhan, X. Wang, Z. Xiong, H. Shi, X. Ding, W. Huang and X. Hou, "Aggregation and permeation of 4-(dicyanomethylene)-2-methyl-6-(p-dimethylaminostyryl)-4h-pyran molecules in Alq," *Appl. Phys. Lett.* **81**, 1122–1124, 2002.

[79] K. Yagi, S. Shibata, T. Yano, A. Yasumori, M. Yamane and B. Dunn, "Photostability of the laser-dye DCM in various inorganic-organic host matrices," *J. of Sol-Gel Sc. and Techn.* **4**, 67–73, 1995.

[80] F. P. Rosselli, W. G. Quirino, C. Legnani, V. L. Calil, K. C. Teixeira, A. A. Leitão, R. B. Capaz, M. Cremona and C. A. Achete, "Experimental and theoretical investigation of tris-(8-hydroxy-quinolinate) aluminum (Alq$_3$) photo degradation," *Org. Electron.* **10**, 1417–1423, 2009.

[81] K. Higginson, D. Thomsen III, B. Yang and F. Papadimitrakopoulos, "Chemical degradation and physical aging of aluminum(III) 8-hydroxyquinoline: Implications for organic light-emitting diodes and material design," in *Organic light-emitting devices: a survey*, J. Shinar, ed., ch. 3, 71–85, Springer New York, 2004.

[82] C. Féry, B. Racine, D. Vaufrey, H. Doyeux and S. Cinà, "Physical mechanism responsible for the stretched exponential decay behavior of aging organic light-emitting diodes," *Appl. Phys. Lett.* **87**, 2005.

[83] H. Yokoyama, K. Nishi, T. Anan, Y. Nambu, S. D. Brorson, E. P. Ippen and M. Suzuki, "Controlling spontaneous emission and threshold-less laser oscillation with optical microcavities," *Optical and Quantum Electronics* **24**, 245–272, 1992.

[84] B. Gayral, "Controlling spontaneous emission dynamics in semiconductor microcavities: An experimental approach," *Ann. de Phys.* **26**, 2001.

[85] S. Reitzenstein, A. Bazhenov, A. Gorbunov, C. Hofmann, S. Munch, A. Löffler, M. Kamp, J. P. Reithmaier, V. D. Kulakovskii and A. Forchel, "Lasing in high-Q quantum-dot micropillar cavities," *Appl. Phys. Lett.* **89**, 051107, 2006.

[86] S. M. Ulrich, C. Gies, S. Ates, J. Wiersig, S. Reitzenstein, C. Hofmann, A. Löffler, A. Forchel, F. Jahnke and P. Michler, "Photon statistics of semiconductor microcavity lasers," *Phys. Rev. Lett.* **98**, 043906, 2007.

[87] P. Michler, A. Kiraz, L. Zhang, C. Becher, E. Hu and A. Imamoglu, "Laser emission from quantum dots in microdisk structures," *Appl. Phys. Lett.* **77**, 184–186, 2000.

[88] J. Cha, M. Bartl, M. Wong, A. Popitsch, T. Deming and G. Stucky, "Microcavity lasing from block peptide hierarchically assembled quantum dot spherical resonators," *Nano Lett.* **3**, 907–911, 2003.

[89] H. Y. Ryu, M. Notomi, E. Kuramoti and T. Segawa, "Large spontaneous emission factor (> 0.1) in the photonic crystal monopole-mode laser," *Appl. Phys. Lett.* **84**, 1067–1069, 2004.

[90] S. Strauf, K. Hennessy, M. Rakher, Y. Choi, A. Badolato, L. Andreani, E. Hu, P. Petroff and D. Bouwmeester, "Self-tuned quantum dot gain in photonic crystal lasers," *Phys. Rev. Lett.* **96**, 2006.

[91] G. Björk, S. Machida, Y. Yamamoto and K. Igeta, "Modification of spontaneous emission rate in planar dielectric microcavity structures," *Phys. Rev. A* **44**, 669–681, 1991.

[92] P. Schneeweiss, M. Sudzius, R. Gehlhaar, M. Hoffmann, V. G. Lyssenko, H. Fröb and K. Leo, "Observation of Kastler ring stimulated emission from an organic microcavity," *Appl. Phys. Lett.* **91**, 2007.

[93] D. Bajoni, P. Senellart, E. Wertz, I. Sagnes, A. Miard, A. Lemaitre and J. Bloch, "Polariton laser using single micropillar GaAs-GaAlAs semiconductor cavities," *Phys. Rev. Lett.* **100**, 2008.

[94] T. Enomoto, T. Sasaki, K. Sekiguchi, Y. Okada and K. Ujihara, "Intensity fluctuation of a pulsed planar microcavity laser," *J. of Appl. Phys.* **80**, 6595–6601, 1996.

[95] M. McGehee and A. Heeger, "Semiconducting (conjugated) polymers as materials for solid-state lasers," *Adv. Mat.* **12**, 1655–1668, 2000.

[96] V. G. Kozlov, G. Parthasarathy, P. E. Burrows, V. B. Khalfin, J. Wang, S. Y. Chou and S. R. Forrest, "Structures for organic diode lasers and optical properties of organic semiconductors under intense optical and electrical excitations," *IEEE J. Quantum El.* **36**, 18–26, 2000.

[97] P. Andrew, G. Turnbull, I. Samuel and W. Barnes, "Photonic band structure and emission characteristics of a metal-backed polymeric distributed feedback laser," *Appl. Phys. Lett.* **81**, 954–956, 2002.

[98] M. Reufer, S. Riechel, J. Lupton, J. Feldmann, U. Lemmer, D. Schneider, T. Benstem, T. Dobbertin, W. Kowalsky, A. Gombert, K. Forberich, V. Wittwer and U. Scherf, "Low-threshold polymeric distributed feedback lasers with metallic contacts," *Appl. Phys. Lett.* **84**, 3262–3264, 2004.

[99] M. Kaliteevski, I. Iorsh, S. Brand, R. Abram, J. Chamberlain, A. Kavokin and I. Shelykh, "Tamm plasmon-polaritons: Possible electromagnetic states at the interface of a metal and a dielectric Bragg mirror," *Phys. Rev. B* **76**, 2007.

[100] C. Symonds, A. Lemaitre, E. Homeyer, J. Plenet and J. Bellessa, "Emission of Tamm plasmon/exciton polaritons," *Appl. Phys. Lett.* **95**, 2009.

[101] M. Sasin, R. Seisyan, M. Kaliteevski, S. Brand, R. Abram, J. Chamberlain, I. Iorsh, I. Shelykh, A. Egorov, A. Vasil'ev, V. Mikhrin and A. Kavokin, "Tamm plasmon-polaritons: First experimental observation," *Superlat. and Microstruct.* **47**, 44–49, 2010.

[102] J. Bellessa, C. Bonnand, J. Plenet and J. Mugnier, "Strong coupling between surface plasmons and excitons in an organic semiconductor," *Phys. Rev. Lett.* **93**, 036404, 2004.

[103] C. Mowatt, S. M. Morris, M. H. Song, T. D. Wilkinson, R. H. Friend and H. J. Coles, "Comparison of the performance of photonic band-edge liquid crystal lasers using different dyes as the gain medium," *J. Appl. Phys.* **107**, 2010.

[104] S. Toffanin, R. Capelli, T.-Y. Hwu, K.-T. Wong, T. Ploetzing, M. Foerst and M. Muccini, "Molecular host-guest energy-transfer system with an ultralow amplified spontaneous emission threshold employing an ambipolar semiconducting host matrix," *J. of Phys. Chem. B* **114**, 120–127, 2010.

[105] T. Matsushima and C. Adachi, "Observation of extremely high current densities on order of ma/cm^2 in copper phthalocyanine thin-film devices with submicron active areas," *Jap. Journ. of Appl. Phys. Pt. 2 - Lett. & Expr. Lett.* **46**, L1179–L1181, 2007.

[106] S. Z. Bisri, T. Takenobu, Y. Yomogida, T. Yamao, M. Yahiro, S. Hotta, C. Adachi and Y. Iwasa, "Fabrication of ambipolar light-emitting transistor using high-photoluminescent organic single crystal," in *Proc. SPIE "Org. Opt.el. and Phot. III"*, **6999**, SPIE, 2008.

[107] S. Kena-Cohen and S. R. Forrest, "Room-temperature polariton lasing in an organic single-crystal microcavity," *Nat. Phot.* **4**, 371–375, 2010.

[108] J. Xi, J. Kim, E. Schubert, D. Ye, T. Lu, S. Lin and J. Juneja, "Very low-refractive-index optical thin films consisting of an array of SiO$_2$ nanorods," *Opt. Lett.* **31**, 601–603, 2006.

[109] R. Brückner, J. Haase, M. Sudzius, F. H. Hintschich, S.I., V. Lyssenko and K. Leo, "Unpublished results.".

Acknowledgments

Here I want to thank all the persons who contributed to the thesis in one form or another.

Prof. Dr. Karl Leo has supervised my scientific work and provided excellent working and research conditions as head of the IAPP. From the beginning, he supported the investigation of the laterally confined microcavities, although the experience with these structured systems in our group was scarce. Especially the sometimes demanding high level discussions in scientific meetings about physical denotations and fundamental principles of microcavities remain unforgettable. He also earns respect for the regular personal consultations and fast proofreading of papers, despite a tight schedule with many official travellings. Furthermore, I want to thank for the continuous financial funding conditions and the numerous opportunities to attend national and international conferences.

The part Prof. Dr. Vadim G. Lyssenko contributed to this work cannot be overemphasized. His experience, gained in decades of scientific work, the constant efforts to motivate for new and unusual ideas and all the intense discussions initiated many of the shown experiments. It was always a pleasure to work with him, although he sometimes confronted me with challenging tasks. I hope, he continues to be a restless scientist, even when he will officially be retired. Vadim, огромное спасибо за возможность работать с Вами.

Dr. Hartmut Fröb I have to thank for his straightforward leadership of the OIML group, allowing a rather unrestricted experimental work. His personal contacts to partners of industry and scientific institutes together with practical experience in sample processing often allowed to take another step forward. Not to mention that he is a pleasant companion for the off-time of scientific conferences.

With the help of Dr. Markas Sudzius, it was possible to observe the lasing of photonic boxes for the first time. As the person in charge for the short-pulse laser system, he not only allowed for the measurements but provided profound information on stimulated emission and mode distribution theory. Furthermore, he emphasized a precise description and modelling, which improved the quality of our publications.

My former diploma thesis advisor Dr. Robert Gehlhaar introduced me into the

field of organic microcavity physics and inspired me during the first steps with the structured samples. I also have to thank you and Mariana for the kind hospitality during my work visit in Fukuoka.

The former diploma students Ellen Siebert-Henze and Felix Becker helped me with the measurements of the polarization properties and their numerous questions improved my understanding of the theory of the systems.

Dr. Susanne I. Hintschich as head of the SPEX group gave good advices for the experiments and by her scientific and language experience she helped to improve talks and publications.

The current and former group members Daniel Kasemann, Robert Brückner, Johannes Haase and Clemens Schriever I thank for being great colleagues and friends. Not only do we share the same enthusiasm for the experimental and technical details, but also the humor and non-university interests. In the same breath I have to mention my office co-workers Hannah Ziehlke, Steffen Pfützner and Jan Meiß. Thank you for creating the best ecosystem in the Königbau during the last years, and I will definitively miss our regular lunch break sport events.

Dr. Marieta Levichkova and Sylke Furkert introduced me into the measurement and handling of organic dyes and helped for the chemistry, whereas Kai Schmidt and his team did a very good job managing the IT infrastructure of the institute. And not to forget Eva Schmidt and Jutta Hunger, who helped in the daily fights against administration matters.

All members of the IAPP, which I did not mention personally, I acknowledge for the pleasant working atmosphere and the spectacular christmas parties.

Prof. Dr. Chihaya Adachi kindly gave me the oportunity to visit his institute in Fukuoka and to attend the IMR workshop in Sendai. Here, I came into contact with the promising experiments of PhD student Satria Z. Bisri, which started a fruitful scientific colaboration.

Now is the time to thank my family and friends for the necessary balance in my freetime. My parents paved the way and always supported me during my studies. My fiancee Arlett I need to thank for her appreciation, especially regarding my revolutionary simple ideas of applied chemistry. And our adorable daughter always paid attention that I take regularly breaks to not lose myself in writing.

Erklärung

Hiermit bestätige ich, dass ich diese Promotionsarbeit ohne unzulässige Hilfe Dritter und ohne die Benutzung anderer als der angegebenen Hilfsmittel angefertigt habe. Die aus fremden Quellen direkt oder indirekt übernommenen Gedanken sind als solche kenntlich gemacht. Die Arbeit wurde bisher weder im Inland noch im Ausland in gleicher oder ähnlicher Form einer anderen Prüfungsbehörde vorgelegt.

Maik Langner   Dresden, 31. August 2010